



On the evolution of first-year sea ice

Iris Ehlert



Hinweis

Die Berichte zur Erdsystemforschung werden vom Max-Planck-Institut für Meteorologie in Hamburg in unregelmäßiger Abfolge herausgegeben.

Sie enthalten wissenschaftliche und technische Beiträge, inklusive Dissertationen.

Die Beiträge geben nicht notwendigerweise die Auffassung des Instituts wieder.

Die "Berichte zur Erdsystemforschung" führen die vorherigen Reihen "Reports" und "Examensarbeiten" weiter.



Notice

The Reports on Earth System Science are published by the Max Planck Institute for Meteorology in Hamburg. They appear in irregular intervals.

They contain scientific and technical contributions, including Ph. D. theses.

The Reports do not necessarily reflect the opinion of the Institute.

The "Reports on Earth System Science" continue the former "Reports" and "Examensarbeiten" of the Max Planck Institute.

Anschrift / Address

Max-Planck-Institut für Meteorologie
Bundesstrasse 53
20146 Hamburg
Deutschland

Tel.: +49-(0)40-4 11 73-0
Fax: +49-(0)40-4 11 73-298
Web: www.mpimet.mpg.de

Layout:

Bettina Diallo, PR & Grafik

Titelfotos:

vorne:

Christian Klepp - Jochem Marotzke - Christian Klepp

hinten:

Clotilde Dubois - Christian Klepp - Katsumasa Tanaka

On the evolution of first-year sea ice

Iris Ehlert

aus Neustrelitz, Deutschland

Hamburg 2012

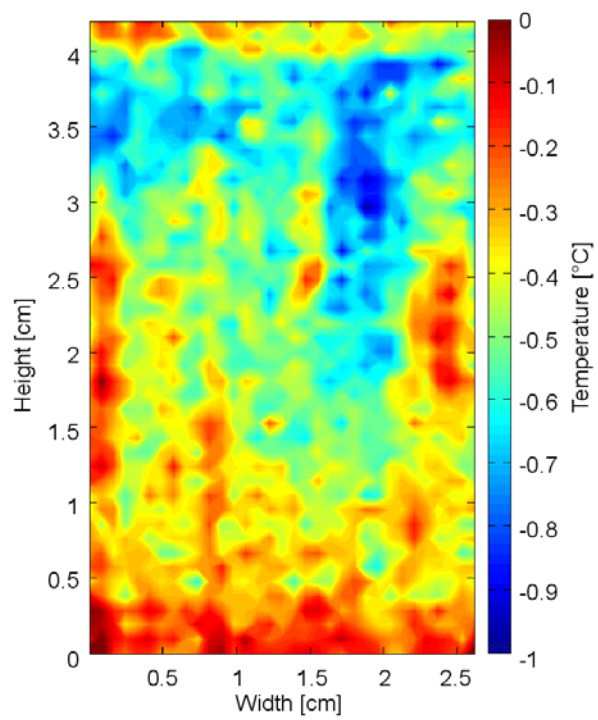
Iris Ehlert
Max-Planck-Institut für Meteorologie
Bundesstrasse 53
20146 Hamburg

Als Dissertation angenommen
vom Department Geowissenschaften der Universität Hamburg

auf Grund der Gutachten von
Prof. Dr. Björn Stevens
und
Dr. Dirk Notz

Hamburg, den 26. Juni 2012
Prof. Dr. Jürgen Oßenbrügge
Leiter des Departments für Geowissenschaften

On the evolution of first-year sea ice



Iris Ehlert

Hamburg 2012

ABSTRACT

First-year sea ice is expected to be the prevailing sea-ice type in the Arctic in the 21st century. However, in-situ observations on the evolution of first-year sea ice and its accompanying interaction with the ocean and the atmosphere are largely lacking. This thesis investigates a variety of measurements above, within, and below growing and melting first-year sea ice that were obtained during both lab experiments and a winter-long field campaign at the north-western coast of Greenland during the unusually warm winter of 2009/2010.

One feature that can only be observed on first-year sea ice is frost flowers. I investigate how frost flowers influence the growth and melt of first-year sea ice. I find that the insulating effect of frost flowers leads to lower ice thicknesses during freezing, and that the dissolution of the underlying sea ice by the salty frost-flower meltwater enhances the melting process.

The bulk salinity of sea ice strongly influences the energy transport through sea ice. I investigate the processes responsible for the desalination of first-year sea ice during its transition from a winter state to its complete melt in summer. I find that the overall temperature increase during spring together with the high bulk salinity of first-year sea ice leads to an increase in sea-ice permeability and enables gravity drainage. Flushing occurred after the desalination by permeability drainage.

To obtain the bulk-salinity evolution of sea ice in situ, we improved the electronic setup of an already existing instrument. The novel development is capable to measure the individual parts of the impedance between two thin metallic wires that are frozen into the ice. Results show the impedance to be almost exclusively resistive. However, the high sensitivity of the mechanical setup of the instrument and its influence on the properties of the ice forming between the wires calls into question the field applicability of this instrument.

I investigate the role of the evolution of first-year sea ice for the physical properties of its adjacent layers in atmosphere and ocean, and on the heat flux at the ocean surface during both abrupt and gradual transitions from an ice-free to an ice-covered ocean. Maximum oceanic heat loss occurred during the initial formation of a continuous sea-ice cover. I apply a conceptual model to estimate ice thicknesses and ocean-to-ice heat-transfer coefficients. The ocean-ice-coupling coefficient was highest during periods of high ice production. Estimated ice thicknesses agree well with observations until accumulation of heat at the ice surface induced melting of the ice interior.

*If we see light at the end of the tunnel,
it's the light of the oncoming train.*

— Robert Lowell

DANKSAGUNG

Diese Arbeit beruht im Wesentlichen auf Ergebnissen, die ich während eines Feldexperimentes auf Grönland gewonnen habe. Dies war nur dadurch möglich, dass Dirk Notz den Kontakt zu Arved Fuchs hergestellt hat, und wir zusammen mit René Fontes ein sowohl unter wissenschaftlichen als auch sozialen Gesichtspunkten einmaliges und äußerst interessantes Experiment auf die Beine gestellt haben. Dies war eine Erfahrung, die nicht jedem einfach so vor die Füße fällt. Das war toll, einer meiner bis dahin unerfüllten Träume, ein Superlativ. Und Ihr, lieber René, Arved und Dirk, habt mich bei seiner Ausführung unglaublich unterstützt. Vielen Dank!

Rémy Tokouda hat während dieses Feldexperimentes unschätzbare Eiskerne genommen, ohne die ein ganzes Kapitel dieser Arbeit nicht existent wäre. Auch Miles McPhee, der uns während einer sehr turbulenten Woche im Feld besucht und Messungen gemacht hat, sei an dieser Stelle für die von ihm gewonnenen Daten gedankt, welche ich in der Folge nur mit der fachlichen und instrumentellen Unterstützung von Anders Sirevaag und Lisbeth Håvik im Labor zu simulieren versuchen konnte.

Während des RECARO-Experimentes in der HSVA nahm das Schicksal seinen Lauf... Ich danke Klaus Niederhausen, der mich während dieser Zeit sehr unterstützt hat. Hier lernte ich auch Marcel Nicolaus kennen, dem ich in der Folge wertvolle Tipps bezüglich der Auswertung von Strahlungsmessungen verdanke. Im Mai 2008 hatte ich die Gelegenheit, die auf ihre Art sehr beeindruckende und zugleich nördlichste Siedlung der USA (Barrow, Alaska) während einer von Hajo Eicken organisierten Sommerschule kennenzulernen. Vielen Dank, Hajo, für diese wertvolle Erfahrung und einen sehr konzentrierten und tiefen Einblick in die Weiten der experimentellen Meereisforschung!

Im Gegensatz zu Feldexperimenten laufen Laborexperimente immer unter kontrollierten Bedingungen ab (rolle-mich-lachend-auf-dem-boden). Wie entscheidend jedoch auch nur die kleinsten Dinge bei der Ausführung von Laborexperimenten sein können, habe ich während meiner Arbeit immer wieder erfahren müssen. Ein wesentlicher Teil wurde dadurch abgefangen, dass ich jederzeit auf die Hilfe von Björn Brüggemann, Friedhelm Jansen und Lutz Hirsch zählen konnte. Vielen Dank für Eure stete Hilfsbereitschaft, ungezählte Meter Kabel, Lötspitzen und nicht zuletzt die Infrarotkamera. Nicht unerwähnt bleiben sollen Marta Zygmuntowska und Carsten Abraham, die mir geholfen haben, die Lady zu löten und ihre Drähte zu spannen. Und dann war da noch Lars Krieger ... ja, Lars, irgendwie hatten wir schon eine ziemlich nette Zeit da oben, im vermaledeiten 13. Stock. Apropos vermaledeit—zusammen mit meinem damaligen Kollegen und langjährigen Freund René Fontes könnte ich ein Buch über die Unglückszahl 13 schreiben... Danke, René, für all das, was wir zusammen erarbeitet haben. Scheitern gehört eben einfach dazu.

Das Arbeitsumfeld des MPI bietet ein unvergleichliches intellektuelles Potential. Unvergessen sind vor allem die alle zwei Jahre stattfindenden Retreats, die die Möglichkeit bieten, die Arbeitsweise und Ergebnisse der verschiedenen Abteilungen des Institutes immer wieder neu kennenzulernen und Verbindungen zu knüpfen, die in Alltagssituationen gar nicht oder nur schwer möglich sind.

Ebenso unvergleichlich ist der Komfort. Wann immer Probleme mit Rechnern auftraten, konnte ich der Hilfe der Mitarbeiter von CIS gewiss sein. Vielen Dank insbesondere an Lambert Rasche, Jan Sellmann, Alexander Bugl, Jörn Heinemeier, Mario Bernhardt und die vielen, vielen Studenten, die mir im Laufe der Jahre über den Weg liefen und ohne die CIS nicht das wäre, was es ist. Ich danke den Verwaltungsmitarbeitern Evelyn Wolters, Andrea Altenburg, Uwe Mohr, Frank Schlichting, Reiner Letscher, Darja Katrytsch und Hildegard Grebe für den stets reibungslosen Ablauf bei der Abwicklung unserer Bestellungen für unser Feldexperiment oder das Labor, der Bearbeitung unserer Dienstreisen und der Annahme ungezählter Pakete. Dass all das einfach funktioniert, ist toll! Carola Kauhs danke ich für ihre Geduld bezüglich der Rückgabe von Büchern. Ich finde es schön, dass es in unserer Zeit noch eine derartige Bibliotheksstruktur geben kann.

Wie langweilig und einsam das Doktorandenleben ohne die vielen Kollegen gewesen wäre, vermag ich kaum einzuschätzen. Deshalb möchte ich an dieser Stelle insbesondere danken: Ronny Petrik und Florian Rauser (Wehre den Anfängen!), Chao Li (Der netteste Pavillonkorrespondent.), Freja Vamborg und Kenji Shimizu, Zoltan Szuts, Leif Riemenschneider, Michael Botzet, Sven Deinert und Volker Umland (Und er ist doch nicht dicht!), Andreas Chlond und Gottfried Kruspe (Das war wirklich ein ganzes Fass!), Norbert Noreiks, Kornelia Müller (Du weißt ganz genau, dass Du Schuld an den Rückenschmerzen bist.), Karl-Hermann Wieners, Antje Weitz, Jin-Song von Storch und Uwe Mikolajewicz (Das war doch mal ein Anfang!), Johann Jungclaus (Auch Kaffee gehorcht der Schwerkraft.), Ernst Maier-Reimer (Ich muss noch das Infrarotbild machen ... In einer halben Stunde vielleicht?) und—Peter Müller. Und natürlich wären die Pausen an der frischen Luft ohne Rosina Grimm nur halb so nett gewesen; danke Rosi. Auch der Beistand, den ich während meiner schwierigsten persönlichen Krise durch René, Werner Bauer und Connie Kampmann erfahren habe, hat ermöglicht, dass diese Arbeit überhaupt zustande gekommen ist. Das werde ich Euch nie vergessen. Danke.

Ohne die unzähligen fachlichen Diskussionen mit Jochem Marotzke wäre diese Arbeit nicht, was sie ist. Vielen Dank, Jochem, für Deine stete Bereitschaft, in die experimentelle Meereiswelt abzutauchen und meinen Blickwinkel durch den Deinen für ganz neue Bereiche zu öffnen.

Die Freiheit, die mir in der Gestaltung meiner Doktorarbeit und bei der Ausarbeitung der wissenschaftlichen Fragestellungen gewährt wurde, stellte eine große Herausforderung dar, und meine erste Anerkennung für das, was ich gemacht habe, sollte mir auch erst nach den teilweise sehr frustrierenden Jahren mit einem nicht funktionierenden Instrument im Oktober 2011 von Björn Stevens für etwas ausgesprochen werden, das nebenbei herauskommen kann. Danke Björn! Das war sehr motivierend.

Mein größter Dank jedoch gilt meinem P, Ava und Lui. Ohne Euch, Eure Liebe und Unterstützung wäre all das sowieso unmöglich und für die Katz gewesen.

CONTENTS

I INTRODUCTION	1
1 INTRODUCTION	3
1.1 Motivation and research questions	3
1.2 Thesis outline	5
II SEA ICE LAUGHS	7
2 THE INTERACTION BETWEEN FROST FLOWERS AND SEA ICE	9
2.1 Introduction	10
2.2 Field experiment	11
2.3 Laboratory experiment	14
2.4 Nucleation of frost flowers	16
2.4.1 Observations in the field	17
2.4.2 Observations in the lab	18
2.4.3 Discussion	19
2.5 Growth and melt of frost-flowers	20
2.5.1 Temperature evolution in the field	20
2.5.2 Temperature evolution in the lab	22
2.5.3 Salinity observations in field and lab	24
2.5.4 Morphology observations in field and lab	26
2.5.5 Discussion	27
2.6 The influence of frost flowers on sea-ice thickness	31
2.7 Summary and conclusions	33
III SEA ICE CRIES	35
3 WARMING INDUCED SEA-ICE DESALINATION	37
3.1 Introduction	38
3.2 Setup and methods	39
3.3 Desalination of the whole ice column observed from ice cores	41
3.4 Desalination not driven by flushing	42
3.5 Desalination was driven by permeability drainage	44
3.6 Summary and conclusions	46
IV SEA ICE RESISTS	47
4 WIRE-HARP MEASUREMENTS REVISITED	49
4.1 Introduction	50
4.2 Theoretical background	51
4.3 From wire harp towards Harp3d	54
4.4 Intermediate results of Harp3d	56
4.5 Summary and conclusions	59
V A SEA-ICE LIFE ON A WARM OCEAN	61
5 HEAT EXCHANGE THROUGH FIRST-YEAR SEA ICE	63
5.1 Introduction	64
5.2 Field campaign	65
5.2.1 Setup and methods	66
5.2.2 Observed ice and weather conditions	66
5.2.3 Estimation of sea-ice state from humidity	67
5.2.4 Impact of sea ice on hydrography	69
5.3 A lab study on sea-ice formation on warm water	72

5.3.1	Setup and method	73
5.3.2	Results and discussion	74
5.3.3	Conclusions	76
5.4	Heat-flux estimates	76
5.4.1	Longwave and shortwave radiation	77
5.4.2	Surface-temperature estimation	78
5.4.3	Turbulent heat exchange	79
5.4.4	Methods for heat-flux calculations	80
5.4.5	Results and discussion	81
5.4.6	Estimation of heat-transfer coefficients	83
5.4.7	Estimation of ice thickness	85
5.5	Summary and conclusions	88
VI	SUMMARY	89
6	SUMMARY	91
	BIBLIOGRAPHY	93

LIST OF FIGURES

Figure 2.1	Air-temperature anomalies	12
Figure 2.2	Environmental conditions during field study	13
Figure 2.3	Evolution of frost-flower coverage within three days.	14
Figure 2.4	Terms for the parts of a frost flower used in this work: frost flower, frost-flower root, skim layer and frost-flower-covered sea ice. Additionally, there is bare ice without frost flowers on top.	14
Figure 2.5	Tank setup	15
Figure 2.6	Skim-layer close up	17
Figure 2.7	Morphologies of frost flowers in a Greenlandic bay in March 2010.	17
Figure 2.8	Conditions during first laboratory experiment.	19
Figure 2.9	Temperatures above, within and below frost flowers and the underlying sea ice	21
Figure 2.10	Difference between surface temperature of frost flower and bare ice in relation to the size of a frost flower	23
Figure 2.11	Surface temperature of bare ice and frost-flower melt-water	23
Figure 2.12	Salinities of frost flowers and sea ice	25
Figure 2.13	Salinity of frost flowers vs. time and air temperature.	29
Figure 2.14	Photograph of a frost flower	29
Figure 2.15	What a frost flower leaves behind	30
Figure 2.16	Morphology and temperature of sea ice that was influenced by frost-flower growth	30
Figure 2.17	Ice thickness of frost-flower covered ice and bare ice calculated from surface temperature	32
Figure 2.18	Life cycle of a frost flower	34
Figure 3.1	Sampling site	40
Figure 3.2	Change of ice-surface structure	40
Figure 3.3	Temperature and bulk salinity from ice cores	41
Figure 3.4	Air temperature and deviations from oceanic salinity and temperature	42
Figure 3.5	Brine density and ice permeability	45
Figure 3.6	Temperature, brine-salinity, brine-density, and permeability profiles during different life stages of first-year sea ice	46
Figure 4.1	Sketch of measuring device.	51
Figure 4.2	Sketch of impedance.	52
Figure 4.3	Equivalent circuit.	53
Figure 4.4	Error source for old instrument and dependency of impedance on distance.	55
Figure 4.5	Top view of measuring device frozen into ice.	56
Figure 4.6	Evolution of impedance in sodium-chloride ice.	57
Figure 5.1	Air-temperature anomalies	65
Figure 5.2	Air temperature, relative humidity, air pressure and wind speed during field campaign	68
Figure 5.3	Oceanic salinity, temperature and density 50 cm below growing and melting sea ice	70

Figure 5.4	Cross correlation between air and ocean parameters	71
Figure 5.5	Tank setup	73
Figure 5.6	Temporal evolution of parameters	74
Figure 5.7	Zoom into equilibration	75
Figure 5.8	Sketch of sea-ice-heat budget	77
Figure 5.9	Longwave and shortwave radiation balances.	78
Figure 5.10	Surface temperature.	78
Figure 5.11	Fits for deriving surface temperature.	79
Figure 5.12	Turbulent heat fluxes.	80
Figure 5.13	Heat flux through growing and melting first-year sea ice.	81
Figure 5.14	Estimated heat-transfer coefficients.	84
Figure 5.15	Estimated ice thickness.	85
Figure 5.16	Difference between bulk-ice and surface-air temperatures.	86
Figure 5.17	Cross correlation between difference between surface and air temperature and bulk-ice temperature.	87

LIST OF TABLES

Table 2.1	Conditions at freeze-up and formation of frost flowers during laboratory experiments.	18
Table 2.2	Comparison of temperature above and below growing FF.	22
Table 2.3	Salinity of frost flowers and their roots taken in NW Greenland in March 2010.	24
Table 2.4	Temperature of flower relevant components after melt	27
Table 2.5	Influence of frost flowers on ice thickness	32

ACRONYMS

FF	frost flower
FFR	frost-flower root
FFM	frost-flower meltwater
BI	bare ice

Part I

INTRODUCTION

... what has fascinated so many explorers on their journeys, and what is so unique in Polar regions that there is nowhere anything like it: that is the life cycle of the sea-ice in the course of one year and in the course of a whole number of years. It is the history of its life, showing us its birth or origin, its growth, its attaining its maximum thickness, extension and strength, its decline, and finally the end of the sea ice. And this life cycle of the sea-ice which Weyprecht so beautifully called its "metamorphosis", offers, from the scientific point of view, not only some of the most important, but also some of the most interesting and difficult problems which the sea-ice and seawater in general has to offer.

— Josef Zukriegel, 1935

INTRODUCTION

1.1 MOTIVATION AND RESEARCH QUESTIONS

First-year sea ice, which has become the prevailing sea-ice type in the Arctic in the 21st century, is considerably saltier and thinner than multi-year sea ice. It is saltier because it did not yet experience summer melt, and it is thinner because it did not experience the multiple-year cycles of additional ice formation at its bottom. This makes first-year sea ice more vulnerable to natural fluctuations in atmospheric and oceanic forcings.

The recent observed reduction in Arctic sea-ice extent has been accompanied by a substantial loss of multi-year sea ice in all seasons [Johannessen *et al.*, 1999; Comiso, 2002; Nghiem *et al.*, 2007; Maslanik *et al.*, 2007; Kwok *et al.*, 2009; Maslanik *et al.*, 2011]. These formerly multi-year-ice areas are replenished with first-year sea ice, which makes the ice cover as a whole more susceptible to future rapid declines [Maslanik *et al.*, 2007].

The effects of the shrinking and thinning sea-ice cover are expected to be significant on regional and global scales. Because the ice cover insulates the ocean from the polar atmosphere, any change in salinity and thickness of the ice cover will influence the surface-heat exchange, the ability of the ice to reflect the incoming shortwave radiation, and the thermal properties of the ice [Perovich *et al.*, 1998; Perovich and Elder, 2002; Eicken, 2003; Zhang, 2005; Perovich and Richter-Menge, 2009; Weeks, 2010]. The water-vapor content of the atmosphere has increased partly in response to the reduced sea-ice cover and hence modified surface-heat fluxes, which may have enhanced the warming of the lower part of the atmosphere during summer and autumn [Screen and Simmonds, 2010]. Moreover, the increasing first-year sea-ice formation in winter is expected to influence the deep-water formation in polar regions, which is an important component of the global ocean thermohaline circulation [Aagaard *et al.*, 1981; Carmack, 2000; Martinson and Steele, 2001]. Additionally, a thinner ice pack is more easily disrupted by winds, and thus it is very likely to also influence the sea-ice and freshwater export from the Arctic ocean into the northern North Atlantic through Fram Strait. This export modulates the ocean thermohaline circulation, which then feeds back onto the Arctic climate [e. g. Zhang, 2005].

However, the weakness of our current understanding of sea ice and the polar-climate components in general is reflected by the disagreement among results for the Arctic sea-ice retreat in global coupled climate models [Stroeve *et al.*, 2007]. That the age of sea ice explains more than half of the variance in observed and simulated summer sea-ice extent [Rigor and Wallace, 2004] is but one example of the necessity to improve the simulations of a saltier and thinner sea-ice cover under various atmospheric and oceanographic conditions, and to understand how the changing atmosphere-ice-ocean system adjusts to external perturbations.

This improvement of model formulations is impossible without measurements above, within, and below forming, growing, and melting first-year sea ice.

However, datasets obtained during the evolution of first-year sea ice and the interpretation of accompanying processes in the atmosphere and the ocean are largely lacking. One experiment to investigate the state of the atmosphere, ice, and ocean over an entire annual cycle was the experiment to study the Surface Heat Budget of the Arctic Ocean (SHEBA, October 1997 to October 1998). It was directed at acquiring a high-quality and comprehensive dataset of the atmosphere-ice-ocean system and provided the opportunity to investigate processes above and within both multi-year and first-year sea ice [Perovich *et al.*, 1999].

During SHEBA, the ice itself served as a platform that was a Lagrangian drifter. Hence, the SHEBA platform existed throughout the whole year, and the ice that served as a platform grew further after the experiment. The situation is much more difficult if one wants to measure atmospheric and oceanic properties prior to first-year sea-ice formation and during its melt, since the platform in the first place needs to grow, or is almost inaccessible during melting. However, we had the opportunity to use a sailing ship that was overwintering in a small Greenlandic bay at the northwestern coast of Greenland during the unusually warm winter of 2009/2010 [Jung *et al.*, 2010]. This thesis investigates a variety of unique data that we obtained from this platform during the formation, growth, and melt of first-year sea ice.

One feature that can only be observed on first-year sea ice is frost flowers. Frost flowers are known to change a number of physical properties at the sea-ice surface, including the brightness increase at radar frequencies, which leads to difficulties in the radar remote sensing of sea ice because ice thicknesses are overestimated [Onstott, 1992; Martin *et al.*, 1995, 1996; Isleifson *et al.*, 2010]. However, due to the inaccessibility of the very young and thin sea-ice surface on which frost flowers exclusively grow, and the atmospheric prerequisites for frost flowers to grow at all [Style, 2007; Style and Worster, 2009], observations on these fragile, salty crystals are rare, and observations on the temperature evolution above, within, and below frost flowers are nonexistent. This leads to the first set of research questions addressed in this thesis:

What are possible condensation nuclei for frost flowers? How do the temperatures above, within, and below frost-flower-covered ice evolve compared to those for bare ice at the same level? Is there a dependency between the salinity evolution of both frost flowers and the underlying sea ice? Do frost flowers influence the thickness and morphology of the underlying sea ice?

Most properties of sea ice are strong functions of the bulk salinity. Therefore, the evolution of the bulk salinity is crucial for understanding the interaction of sea ice with atmosphere and ocean. Traditionally, the bulk salinity of sea ice is obtained by the extraction of ice cores [e. g. Eicken *et al.*, 2009; Weeks, 2010]. An extensive study of ice-core data obtained from first-year sea ice was carried out by Kovacs [1996], who reexamined ice-core data obtained from a variety of places by Cox and Weeks [1974] and both studies found that the general amount of scatter between the data was quite small with strong general trends [Cox and Weeks, 1974; Kovacs, 1996; Weeks, 2010]. However, ice-core data obtained prior to the complete melt of first-year sea ice to my knowledge are nonexistent. Hence, an investigation of the processes driving the desalination of first-year sea ice during melting was almost impossible in the past. The second research question addressed in this thesis is based on ice-core data I obtained from melting first-year sea ice:

Which processes lead to the desalination of first-year sea ice during its transition from winter to summer?

However, traditional methods to obtain the bulk salinity of sea ice by extracting ice cores are destructive and error-prone due to the outflow of brine during core extraction, and it is difficult to get continuous time series. Hence, an instrument that is capable to measure the bulk-salinity evolution of sea ice in situ would be highly appreciated in the sea-ice community. Due to the combination of the electrically isolating nature of the pure-ice matrix, and the highly conductive saline brine entrapped in the ice matrix, electrical methods are promising. The first attempt to measure the electrical impedance between electrodes that are frozen into the ice was carried out by *Shirtcliffe et al.* [1991]; their instrument has undergone various improvements thereafter [*Shirtcliffe and Kerr*, 1992; *Notz*, 2005; *Yamagishi and Langhorne*]. However, the attempt to use the instrument developed by *Notz* [2005] failed, which leads to the third research question addressed in this thesis:

How applicable are electrical impedance measurements between two thin metallic wires to obtain the bulk-salinity evolution of sea ice in situ?

The scarcity of datasets on the interaction of forming, growing, and melting first-year sea ice with its adjacent layers atmosphere and ocean imply an even higher scarcity of surface heat-flux estimates during those periods. This leads to the fourth and last set of research questions addressed in this thesis:

How does the formation, growth, and melt of first-year sea ice influence the heat exchange between ocean and atmosphere? How can sea-ice formation occur on seawater that is well above its freezing point? Is it possible to estimate ice thicknesses and ocean-to-ice heat-transfer coefficients from the derived surface heat fluxes?

1.2 THESIS OUTLINE

The main part of this thesis consists of four chapters, which are written in the style of journal publications and can thus be read independently of one another. The thesis is structured as follows:

IN PART II, I investigate how the formation, growth, and melt of frost flowers interact with the salinity, temperature, and morphology evolution of the underlying sea ice.

IN PART III, I study processes responsible for the desalination of first-year sea ice during its transition from a winter state to its complete melt in summer.

IN PART IV, I investigate the applicability of an instrument that was developed to study the bulk-salinity evolution of sea ice in situ.

IN PART V, I study how the formation, growth, and melt of first-year sea ice influence the heat exchange between ocean and atmosphere. I apply a conceptual model to estimate ice thicknesses and heat-transfer coefficients.

I give a concise summary of the main results of this thesis in PART VI.

Part II

SEA ICE LAUGHS

Schon nach wenigen Stunden beginnt der Krystallisationsprocess der eingefrorenen Sohle. Büschelweise beisammen stehend schießen die Krystalle zuerst an einzelnen Stellen hervor, wachsen und werden rasch häufiger. Die glatte Oberfläche des jungen Eises sieht bald aus wie eine überfrorene Wiese, auf der hier und da die mit Reif bedeckten Spitzen der Grasbüschel hervorlugen. Die feinen sich verlängernden Nadeln rücken dichter und dichter zusammen und schon nach 24 Stunden hat sich auf dem jungen Eise eine Schichte von mehreren Centimetern Höhe gebildet, die so dicht ist, dass der Uneingeweihte glaubt, es habe geschneit.

— Karl Weyprecht, 1879

THE INTERACTION BETWEEN FROST FLOWERS AND SEA ICE

ABSTRACT

I present field and laboratory observations on the temperature, salinity, and morphology evolution of frost flowers and the sea ice below. In doing so, I provide an extended mechanism of frost-flower formation, growth, and melt, including the accompanying interaction with sea ice.

I find the following: (a) frost flowers nucleate on sea-ice platelets protruding from the sea-ice surface. (b) Frost flowers insulate the underlying sea ice from the cold atmosphere, which can cause frost-flower-covered sea ice to be warmer than bare ice by 1 °C. (c) The growth of frost-flower-covered sea ice is slower than the growth of bare ice. (d) The salinity of frost flowers decreases with age and is dependent on the bulk salinity of the sea ice below. (e) During melting, the salty frost-flower meltwater dissolves the underlying sea ice, which increases the ice's permeability and accelerates its melting.

The ongoing retreat of perennial sea ice is likely to be accompanied by an increase in the areal fraction of frost-flower-covered sea ice. My results suggest that this could cause an additional decrease of the sea-ice thickness due to the insulation of frost flowers, and an acceleration of the melting process of first-year sea ice.

2.1 INTRODUCTION

Frost flowers, salty ice crystals with a size of a few centimeters in width and height, grow on the surface of newly formed sea ice if two environmental conditions are met—the temperature gradient between the sea-ice surface and the atmosphere has to be sufficiently large, and the wind conditions have to be calm [Perovich and Richter-Menge, 1994; Martin *et al.*, 1996; Style and Worster, 2009]. Frost flowers are thought to influence ocean-atmosphere salt and heat exchanges both on regional and large scales, but due to the relative inaccessibility of the Arctic and Antarctic regions, field studies of frost flowers are rare, and studies concerning their interaction with the underlying sea ice are nonexistent. With this chapter, I present measurements of the morphology, temperature and salinity evolution of frost flowers and the underlying sea ice, which I carried out during field and lab experiments.

If the two environmental conditions given above are met, frost flowers can be observed all over the polar regions. In particular, in leads the ocean water is exposed to the cold air, and, due to high temperature gradients between the ocean and the atmosphere in winter, leads usually freeze-over very fast and provide a perfect site for frost flowers to grow. With the ongoing retreat of perennial Arctic sea ice, leads are expected to appear more often, which would increase the likelihood of frost flowers.

Frost flowers change a number of physical properties of the sea-ice surface. They increase the surface roughness and the albedo of young sea ice, since their varying facets reflect incoming shortwave radiation much more effectively than newly formed sea ice without frost flowers. This leads to difficulties in the radar remote sensing of sea ice. The brightness increase at radar frequencies due to the appearance and growth of frost flowers is about the same as the variation of the brightness range for all sea-ice types [Onstott, 1992]. Moreover, frost flowers influence the temperature of the sea-ice surface. Laboratory experiments have shown that the surface temperature of the frost flowers can be 4–6 °C lower than the surface temperature of the same ice after removing the flowers [Martin *et al.*, 1996]. This will lead to young and warm sea ice mistaken for old sea ice in infrared-satellite images, since colder temperatures are falsely assigned to thicker sea ice. The importance of frost flowers on the thermodynamics of the underlying sea ice was illustrated during a field experiment in the Canadian Arctic, where the increase in sea-ice thickness between a frost-flower covered area of sea ice (increase of 1 cm) and the same type of ice cleared of frost flowers (increase of 4 cm), differed by 3 cm after 12 hours [Isleifson *et al.*, 2010].

Another source of interest is the impact of the salt within the flowers on the chemistry of the atmosphere. Sunrise in polar regions brings episodes of almost complete depletion of tropospheric ozone. These ozone-depletion events are correlated with high concentrations of bromine compounds. Since the salt within the flowers also contains chemicals such as bromine monoxide, the formation of new sea ice was proposed to be an important factor in the depletion of ozone [Rankin *et al.*, 2002; Kaleschke *et al.*, 2004; Jones *et al.*, 2006], and the study of frost-flower chemistry was subject of much recent research. Recently, the variation of surface ozone, wind and temperature was measured in Antarctica over one year [Wang *et al.*, 2011]. The results show ozone-depletion events to be strongly correlated with a temperature drop below -30 °C and calm winds, which meets the two environmental

conditions necessary for frost-flower growth. Additionally, the large surface area of the flowers was proposed to give a more effective surface for the distribution of sea-salt aerosols by winds. Sea-salt aerosols are deposited on snow over land, which compacts over time, and later will give information about past atmospheric conditions [Rankin *et al.*, 2002].

However, recent studies [Obbard *et al.*, 2009; Roscoe *et al.*, 2011] call the influence of frost flowers on both ozone depletion events and on sea-salt aerosol concentrations into question, since the authors neither measured an enhanced amount of bromide within frost flowers, nor did they measure an aerosol release from frost flowers. However, in both experiments the authors did not take into account the initial stages of frost-flower formation. The kinetics and the yields of halogens strongly depend on temperature, composition, and acidity of the sea-ice [Huff and Abbatt, 2002], which differs during the very initial stages of sea-ice and frost-flower formation compared to later stages. Hence, an understanding of the physical processes going on during the initial stages of frost-flower formation is crucial to also understanding the chemical processes. However, how and on what type of condensation nuclei frost flowers nucleate, is still not known.

In this chapter, I present field and lab observations on the nucleation and formation of frost flowers, and field and lab measurements of the temperature, salinity, and morphology evolution of frost flowers and the underlying sea ice during freezing and melting processes. To my knowledge, this is the first time that also the melting of frost flowers is documented.

After a presentation of the experimental setups of both the field (section 2.2) and lab experiment (section 2.3), I present and discuss observations regarding the initial nucleation and formation of frost flowers in section 2.4. Measurements and observations on the temperature, salinity, and morphology evolution of frost flowers and the sea ice below I obtained during growth and melt of the flowers, I present in section 2.5. In section 2.6, I use a simple conceptual model to investigate the influence of frost flowers on the evolution of the sea-ice thickness relying on the field and lab observations. I summarize the results in section 2.7.

2.2 FIELD EXPERIMENT

To study the atmosphere-ice-ocean interaction during the formation and growth of young sea ice, we carried out a field experiment in a small Greenlandic bay (72.79° N, 56.06° W) during a few days in March 2010. The site is 5 km beeline to the airport of the settlement Upernavik, which itself is located on an island within the fjord landscape of Western Greenland. A sailing ship overwintering in the bay provided a basis for us and our scientific equipment. The bay covers an area of 120 × 100 m² and had an average depth of 8 m. This bay turned out to be a perfect site to study the evolution of young sea ice under calm conditions, because oceanic currents were almost absent and surrounding mountains protected the bay from the wind.

ENVIRONMENTAL CONDITIONS Influenced by an extreme negative phase of the Arctic Oscillation during the winter 2009/2010 [Jung *et al.*, 2010], which contributed to unusually high temperatures over Western Greenland (see figure 2.1), the freeze-up was extremely late, and the sea ice we found when we arrived on 13 March had only been growing since the end of February.

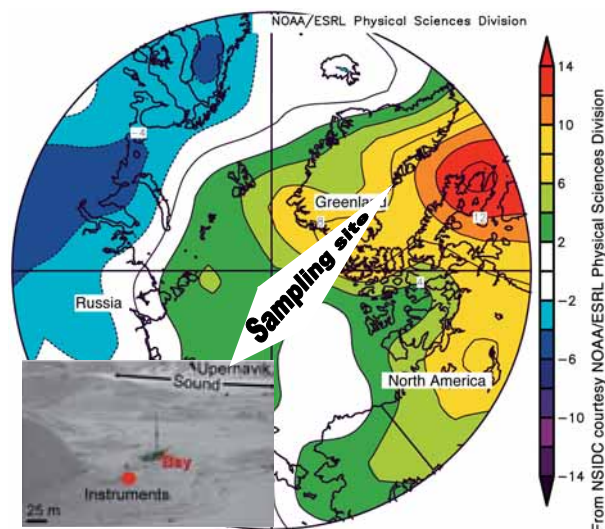


Figure 2.1: Map of air-temperature anomalies for February 2010.^a

^a Provided by the National Snow and Ice Data Center courtesy NOAA/ESRL Physical Sciences Division; source: <http://nsidc.org/arcticseaicenews/2010/030310.html>

The average ice thickness within the bay was 35 cm. For the time of the field experiment, the average sea-water temperature at a depth of 50 cm below the water/ice surface was -1.2 °C. With an average mean seawater salinity of 33.8 g/kg, the seawater temperature was above the freezing point for the whole time of the experiment. During the first three days from 16 March until 19 March it was cloudy in the morning, but turned into almost clear-sky conditions during the afternoon. The mean air temperature was -19 °C, and the mean relative humidity was 79% (see figure 2.2). During the night of 19 March the atmospheric pressure started to rise from 1000 hPa, reaching 1013 hPa on 22 March. Several light snowfall events occurred during that time. The mean air temperature and the mean relative humidity increased to an average value of -13 °C and 86%, respectively. These atmospheric conditions offer the opportunity to study the influence of a frost flower on the temperature evolution above and below growing thin sea ice not only during the growth of a frost flower, but also during snowfall and the onset of frost-flower melt.

SETUP AND METHODS We chose the sampling site in the middle of the bay, so as to be as far as possible away from the surrounding land and from the sailing ship. To simulate the formation of young sea ice from open water, three holes of approximately 1.2×1.2 m² were cut into the already existing sea ice, each with a different time of freeze-up. These three holes were used as sampling areas for frost flowers and the underlying sea ice. Above the surface of one of the holes air temperature¹, wind², and humidity³ sensors were arranged in a height of 20 cm and 2 m, respectively. In the middle of the same hole, two thermistor rods were deployed 40 cm apart from each other. Every rod was made from teflon, had a diameter of 4.5 cm, and con-

¹ Campbell 43347 RTD temperature probe with Campbell 43502 aspirated radiation shield

² Campbell A100R for velocity and Campbell W200P-1 for direction

³ rotronic hygrometer MP 100 A with RS 12 T radiation shield

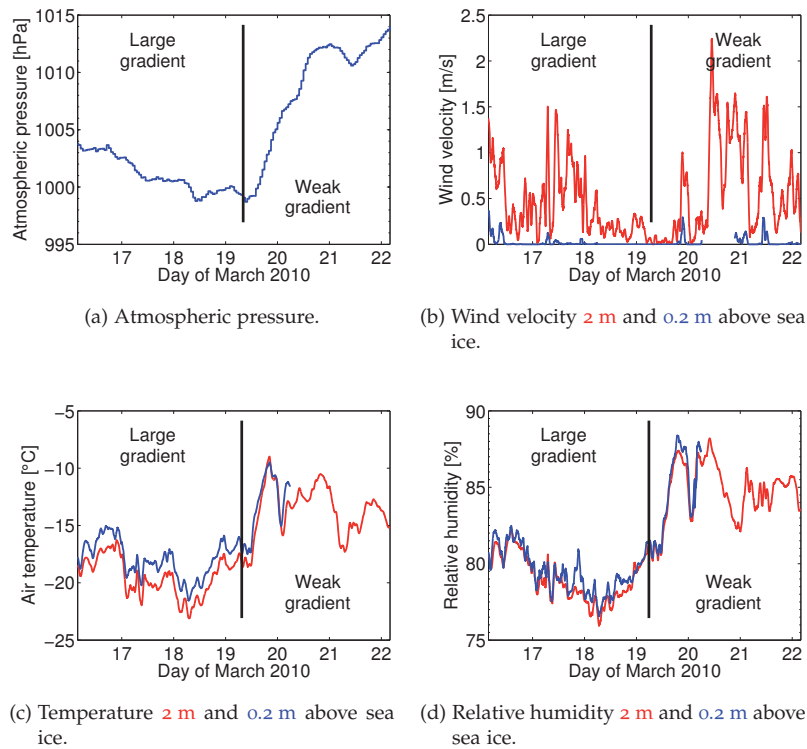


Figure 2.2: Environmental conditions during the field experiment.

tained 29 thermistors⁴. One of the thermistor rods had a vertical resolution of 3 cm; the other thermistor rod had an even higher vertical resolution, ranging from 0.5 cm to 2 cm. The sampling interval of air temperature, wind and humidity sensors was set to 30 s, while for the thermistor rods the sampling interval was set to 10 s. Both the temperature and the humidity sensor at 20 cm height stopped working on 20 March, 4 days after deployment.

To simulate sea-ice growth from open water, each hole was entirely cleared of small ice pieces using a sieve prior to each experiment. In every case, the initial ice growth began under quiescent environmental conditions.

Fortunately, during one experiment that lasted from 17 March until 20 March, a frost flower was growing close to one of the thermistor rods, whereas the other thermistor rod was not affected by frost-flower growth. This offers the opportunity to compare the temperature evolution above and below sea ice that is influenced by frost-flower growth with the temperature evolution above and below sea ice that is *not* affected by frost-flower growth. However, two and a half days after freeze-up, the frost flowers had spread out in the horizontal plane to cover almost the entire surface of the sampling hole (see figure 2.3). Hence, from this moment the temperature within bare ice was also affected by frost flowers at its surface.

Several samples of individual frost flowers, frost-flower roots, and the skim layer on top of the sea-ice surface (as defined in figure 2.4) were taken with a flat metal spatula. To get representative samples of the very thin, newly formed sea ice below and besides the frost flowers, I used an ice screw which

⁴ 2.2K3A1 Series 1 Thermistor, calibrated to an accuracy of 0.05 °C



Figure 2.3: Evolution of the frost-flower coverage of the sampling hole besides the hole with thermistor rods from 17 March until 20 March.

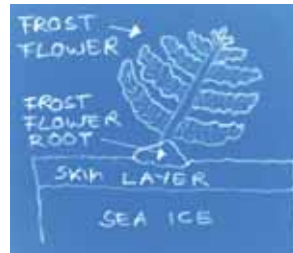


Figure 2.4: Terms for the parts of a frost flower used in this work: frost flower, frost-flower root, skim layer and frost-flower-covered sea ice. Additionally, there is bare ice without frost flowers on top.

normally is used by ice climbers, and took small ice cores with a diameter of 1.2 cm. The salinity of the melted samples was measured with a HQ40d multimeter (accuracy 0.01 g/kg). Sometimes the salinities of the samples were saltier than the measurement range of the multimeter. In those cases I analyzed the samples in the laboratory by diluting the samples with deionized water. The ice thickness was measured with a millimeter-scale ruler. The accuracy of the ice-thickness measurements is within ± 2 mm.

One and a half days after the freeze-up of a hole that had two frost flowers on its surface, I did a section of tiny ice cores along the hole to study the relationship between the salinity of frost flowers and the salinity of the underlying sea ice. To do so, I first sampled the frost flowers and their roots, and then used the ice screw to collect ice cores along a horizontal section covering the entire hole. The spacing between the cores was 5 cm.

2.3 LABORATORY EXPERIMENT

To complement the observations I did in the field, I carried out two lab experiments on the interaction of frost flowers with the adjacent layers of air, sea ice, and ocean during a complete life cycle of the frost flowers—formation, growth, and melt.

SETUP AND METHODS Frost flowers were grown in an insulated tank with inside dimensions of 1.95×0.67 m² and a height of 1.2 m (see figure 2.5), which itself was housed in a cold room with an area of 3×1.25 m² and a height of 2.25 m. The temperature of the cold room can be controlled down to -25 °C. The tank was filled up to a water level of 1 m with sea-

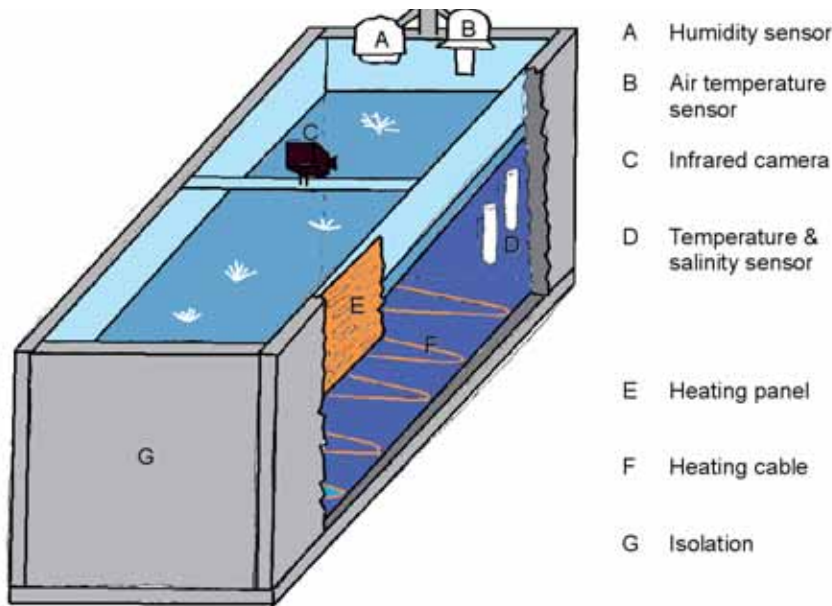


Figure 2.5: Tank setup.

water⁵ mixed to a salinity of approximately 32 g/kg. Heat panels were arranged along the tank sidewalls to avoid pressure generation caused by a complete ice cover frozen to the sides. To simulate a typical mean oceanic heat flux of 4 W/m², we arranged a cable on the floor of the tank that provided this heat flux. The cable also inhibited supercooling of the water below the growing sea ice. To measure the evolution of the temperature and the relative humidity above the sea-ice surface, an air-temperature and a humidity sensor⁶ were arranged 20 cm above the water surface. The sampling interval of both the air-humidity and the air-temperature sensor was set to 30 s. A conductivity-temperature sensor (CT) was arranged at 8 cm below the surface. The sampling interval of the CT was set to 10 s. During the cooling cycles of the cold room, the cold-room ventilator caused an average wind velocity of 0.3 m/s. The de-frost cycles of the cooling machine induced fluctuations of the preset ambient temperature. To measure the evolution of the size of the frost flowers, a commercially available webcam was arranged in a distance of 30 cm from the water/ice surface.

The setup of the two experiments differed in one important respect. During the first experiment (hereafter *Expt1*) a typical fish-tank filter was arranged within the tank to keep the water clean from particles brought into the system during the setup of the experiments. Additionally, this fish-tank filter caused a very weak current of approximately 0.1 m/s, which prevented the water from stratifying. To study the influence of currents below the surface on frost-flower formation, I switched off this filter for the second experiment after the initial condition (homogeneous temperature within the tank) was reached. During the second experiment (hereafter *Expt2*), an infrared camera⁷ was installed directly beneath the webcam to measure the temperature evolution of frost flowers and the surrounding bare ice. Due to setup con-

5 made from TUNZE Reef Excel Lab Marine Salt

6 the same as used for the field experiment

7 Jenoptik IR-TCM 640

straints, the camera looked at an angle of 25° relative to horizontal. However, a test run did not show an influence of the angle on the measured surface temperature at these distances. The sampling interval of the infrared camera was set to 10 s.

For both experiments, I chose the water temperature to be sufficiently warmer than the temperature in the cold room, and then switched the cold room to -25°C , i. e., the strongest cooling possible. The large temperature gradient led to evaporation of the water. The water vapor deposited on the coldest surfaces in the cold room (i. e., the cooling coils of the freezing machine), and also on some metal parts at the tank sidewalls. However, within the frost-flower study area, the vapor deposited on its coldest surface too, i. e., the water surface. This resulted in a humidity gradient above the water/ice surface, which is a prerequisite for the formation of frost flowers [Style and Worster, 2009].

The methods for taking samples of frost flowers, their roots, and the sea ice below were the same as during the field experiment (see section 2.2).

2.4 NUCLEATION OF FROST FLOWERS

When sea ice starts to form from open seawater under calm conditions, 3-4 mm small, needle-like crystals (frazil ice) conglomerate to a thin sea-ice layer (nilas). While the growing ice crystals expel some of the salt into the ocean, some of the salt remains within the sea-ice matrix to form highly concentrated saline brine. If the temperature gradient between the air and the sea-ice surface is sufficiently large and wind speeds are below 5 m/s, the evaporation of the seawater below and enclosed within the ice matrix provides a region of supersaturated vapor adjacent to the ice surface. The vapor then condenses on condensation nuclei that are present on the sea-ice surface [Perovich and Richter-Menge, 1994; Martin *et al.*, 1995, 1996; Style, 2007; Style and Worster, 2009].

The first coherent description of a mechanism for frost-flower growth was given by Style [2007], who improved the observation-based theories suggested by Perovich and Richter-Menge [1994] and Martin *et al.* [1995]. The main result of Style's study is that the only requirement for frost-flower formation is a sufficient temperature gradient between the sea-ice surface and the atmosphere. He corrected the mechanism of Perovich and Richter-Menge [1994] in that the salty skim layer on top of the sea-ice surface (see figure 2.4) is *not* a prerequisite for the growth of frost flowers. This correction was based on observations of frost flowers also appearing on fresh-water lakes [Domine *et al.*, 2005]. Also, Style [2007] was the first to derive a set of governing equations for modeling the growth of frost flowers. He proposed atmospheric ice crystals (snow or diamond-dust crystals) falling on the sea-ice surface to be a likely source for the nucleation of frost flowers. To my knowledge, this has never been observed either in the field or under laboratory conditions. Hence, the physical processes driving the formation of frost flowers are still not fully understood. In the following section, I present observations concerning possible condensation nuclei for the formation of frost flowers.

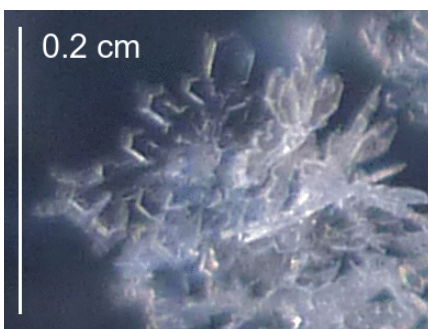
2.4.1 Observations in the field

The frost flowers never formed from diamond-dust crystals (present from 13 March to 19 March; hereafter *large-gradient regime*) or snow crystals (present from 20 March until 23 March; hereafter *weak-gradient regime*; see also figure 2.2) that were falling on the surface of the newly formed sea ice. Instead, these crystals dissolved into the skim layer immediately. Therefore, I doubt that they serve as nuclei for frost flowers as suggested by *Style* [2007]. Instead, the frost flowers formed on sea-ice platelets protruding from the skim layer (see figure 2.6).



Figure 2.6: Close up of the structure of the skim layer one day after opening a sampling hole on 20 March.

During both temperature regimes I removed ice crystals from sampling holes with a sieve several times to get nearly the same time of freeze-up for different holes. Almost immediately after opening the holes, thin sea-ice platelets were floating within the seawater to form the thin, initial sea-ice layer. But the difference in both the thicknesses and the structures of the initial ice crystals after opening the holes during both regimes was striking. Whereas the platelets formed immediately and were thinner, more regular, and harder for the large-gradient regime, the ice surface was a slushy mixture of platelets for the weak-gradient regime. In the same manner, the structure of the ice crystals forming the skim layer, and the thicknesses of the skim layers varied between 0.1-0.3 cm for the large-gradient regime and 0.8 cm for the weak-gradient regime.



(a) Stellar-plate like structure that grew during the night of 15 March ($\hat{T} = -16^\circ\text{C}$, $\hat{r}_h = 81\%$).



(b) Fern-like structure that grew during the night of 18 March ($\hat{T} = -19^\circ\text{C}$, $\hat{r}_h = 78\%$).

Figure 2.7: Morphologies of frost flowers observed during the field study.

Parameter	Expt1	Expt2
at freeze-up		
T_{air} [°C]	-25.1	-21.5
rh_{air} [%]	78.6	80.5
T_{sw} [°C]	-1.5	0.2
S_{sw} [g/kg]	31.36	31.9
at time of frost-flower formation		
T_{air} [°C]	-25.4	-22.7
rh_{air} [%]	78	78
T_{sw} [°C]	-1.6	-1.6
S_{sw} [g/kg]	31.4	32.2

Table 2.1: Temperature and relative humidity of the air 20 cm above, and temperature and salinity of the seawater 8 cm below the water/ice surface at freeze-up and at the time of initial frost-flower formation for the two tank experiments.

Figure 2.7 gives an impression of the frost-flower structures that evolved during a large-gradient regime and a weak-gradient regime. Stellar-shaped flowers only formed once. Unfortunately, this happened when we were arranging our weather station, which is why the air-temperature value of -16 °C and the relative-humidity value of 81% in figure 2.7a stem from the weather station that was 10 m from the hole on which the flowers grew.

For the rest of the field study I only observed fern-like flowers as shown in figure 2.7b. These structures grew both at a mean air temperature of -13 °C and -18 °C and a relative humidity of 85% and 79%, respectively.

2.4.2 Observations in the lab

In the lab, the installed webcam provided the opportunity to record the growth process of frost flowers starting from the very initial stages of their nucleation sites. Frost flowers formed when relative humidity and air temperature were 78% and between -23 - 25 °C, respectively (see table 2.1).

During Expt1, a small ice tip appeared at the surface that served as the nucleation site for a small frost flower approximately one hour after freeze-up. This flower grew for half an hour before it collapsed. The nucleation site then started to grow within the sea ice in all directions for half an hour. One hour after the first ice tip appeared, the same nucleation site protruded from the sea-ice surface as a small-scale topography and provided another ice tip for a frost flower to grow up to a size of 7.2 cm wide and 2.4 cm high within 12 h (see figure 2.8b).

During Expt2, it took much longer for the ice tip that served as the nucleation site for a frost flower to appear. Precisely: nine hours after freeze-up. This flower was growing for approximately one and a half hours before it collapsed. It followed a period of another one and a half hours, where the flower increased its size and collapsed several times, before it started to grow continuously. The final size of the flower after six hours was 4.8 cm wide and 1.4 cm high.

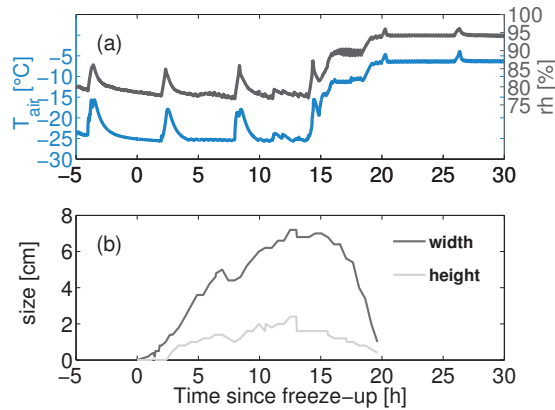


Figure 2.8: Conditions during the first laboratory experiment. a) air temperature and relative humidity 20 cm above the sea-ice surface. b) evolution of the frost-flower size.

Concerning the different environmental forcings for both experiments⁸, it was striking that while the skim layer had a thickness of 0.2 cm during Expt1, there was no skim layer at all during Expt2. In the laboratory, I only observed fern-like frost flowers.

2.4.3 Discussion

Based on the observations described above, I suggest the following concerning possible condensation nuclei for the nucleation of frost flowers:

As frazil-ice crystals conglomerate to form grease ice, some platelets form that have a higher solid fraction (hereafter hsf-platelets) than the surrounding platelets with a lower solid fraction (hereafter lsf-platelets). Due to the higher solid fraction of the hsf-platelets, two physical properties come into play:

1. The thermal conductivity of hsf-platelets is higher than the thermal conductivity of lsf-platelets, and
2. hsf-platelets are less dense.

Hence, as ice growth continues, the higher thermal conductivity leads to a faster growth of the hsf-platelets. While they increase their volume inside the sea-ice layer, they get lighter, and finally “float” on and within the thin sea-ice layer, resulting in a small-scale topography at the sea-ice surface that serves as the nucleation site for frost flowers. Later on, the hsf-platelets form what I defined as the frost-flower root; and the lsf-platelets conglomerate to form what I defined as bare ice throughout this work.

HSF VS. LSF SALINITY: The higher solid fraction of hsf-platelets implies that they have a lower bulk salinity than the lsf-platelets, since the faster growth of hsf-platelets leads to an enhanced expulsion of salty brine into the underlying ocean. Furthermore, the enhanced growth of hsf-platelets due to their higher thermal conductivity leads to a thinning of the capillaries within hsf-platelets and therewith higher brine salinities.

⁸ Expt1 *with* current; Expt2 *without* current; see section 2.3

INFLUENCE OF TEMPERATURE GRADIENT ON SALINITY: A weak temperature gradient leads to lower bulk and brine salinities of the platelets than a large temperature gradient, because the more slowly the sea-ice formation process is, the less seawater is enclosed and the less is the fraction of solid fresh-water ice within the hsf-platelets. This causes the nucleation sites for frost flowers to be less salty and to protrude more from the sea-ice surface under a weak temperature gradient than under a large temperature gradient between ocean and atmosphere.

Thus, the salinity of hsf-platelets and how much they are protruding from the sea-ice surface is determined by the velocity of the freezing process, which in turn is determined by the temperature gradient between ocean and atmosphere during the very initial stages of sea-ice formation. The brine salinity of hsf-platelets is higher under a large-gradient regime.

In addition to the degree of supersaturation above the sea-ice surface, which is dependent on the temperature gradient between ocean and atmosphere, I suggest that the size and the morphology of the protruding platelets determine which frost-flower structure will evolve. During field and laboratory experiments carried out by other authors [Perovich and Richter-Menge, 1994; Martin *et al.*, 1996; Style, 2007], rodlike frost flowers only formed at air temperatures close to and below -30°C , whereas stellar-plate like and fernlike flowers grew at temperatures close to and above -25°C . Since a rapid freezing of the surface leads to a formation of smaller hsf-platelets associated with a higher degree of supersaturation, this may be the case for rodlike frost flowers; and bigger platelets together with a lower degree of supersaturation serve as nuclei for the stellar-plate like and fernlike frost-flower structures.

Hence, the newly formed frost flowers are directly connected to the underlying hsf-platelets with brine-filled, fine capillary systems, and the brine is transported into the frost-flower skeleton by capillarity. The collapses of flowers I observed in the lab during their initial stages of growth, I assign to the initial wicking of relatively warm, saline brine into the capillaries of the flowers. Especially the repeated collapses of the frost flower in Expt2 illustrates the sensitivity of frost flowers within the atmosphere-ice-ocean system. Even though the air temperature is below -20°C , it is the high temperature of the underlying seawater that provides the brine that is rising within the capillary system and overthrows the flower. The collapses substantiate that there is a connection of frost flowers to the underlying sea ice and the ocean already during the early stages of frost-flower growth.

2.5 GROWTH AND MELT OF FROST-FLOWERS

2.5.1 *Temperature evolution in the field*

In the following, I present unique temperature measurements above and below frost-flower covered sea ice. To investigate the influence of frost-flower coverage on the temperature evolution of the underlying sea ice, I compare the temperature evolution above and below sea ice that was affected by a frost flower with the temperature evolution above and below bare ice (see section 2.2 for details).

Almost immediately after opening the sampling hole in which the temperature sensors were deployed, ice crystals formed and conglomerated to a thin

sea-ice layer. Exemplarily, figure 2.9 shows the evolution of the temperature 1 cm above (b) and 5 cm below the growing sea-ice surface (c) for both frost-flower-covered and bare ice during a period of three days. Additionally, the air temperature 20 cm above the sea-ice surface is shown (a).

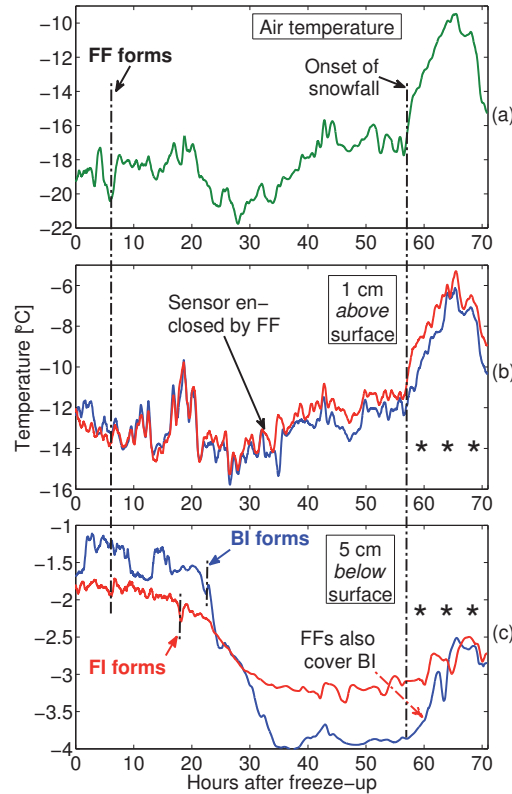


Figure 2.9: (a) Air temperature 20 cm above evolving frost-flower field. (b) Temperature evolution 1 cm above, and (c) 5 cm below the sea-ice surface both close to a frost flower and close to bare ice. Prior to sea-ice formation 5 cm below the frost flower, the temperature was below the freezing point of the initial seawater. Stars indicate period of several snowfall events. FI indicates frost-flower-covered ice, BI indicates bare ice. Note different y-axes.

Prior to frost-flower formation, the measured temperature both above and below the water/ice interface where the frost flower formed afterwards, was lower than the temperature above and below the interface where bare ice formed afterwards. After frost-flower formation and growth, after some time the temperature both above and below frost-flower-covered sea ice was higher than the temperature both above and below bare ice at the same levels. Average values for the differences between the temperature above and below both frost-flower-covered sea ice and bare ice under different conditions are summarized in table 2.2.

When the frost flower reached the temperature sensor at a height of 1 cm above the frost-flower-covered sea-ice surface, the difference between the surface temperature of frost-flower-covered sea ice and bare ice reversed, and the surface temperature of the frost-flower-covered sea ice was higher by approximately 1 °C than the surface temperature of bare ice at this level.

Level above surface	Prior to frost-flower formation	During growth of frost flowers	During snowfall
4 cm	-0.5 °C	+0.3 °C	+1 °C
1 cm	-1 °C	+0.7 °C	+1.3 °C
-2 cm	-0.8 °C	+0.6 °C	+0.7 °C
-5 cm	-0.7 °C	+0.8 °C	+0.5 °C

Table 2.2: Average values of the temperature difference between ice that was influenced by frost-flower growth and bare ice at the same level for several levels above surface.

Snow covering the surface of the frost flower further increased the surface temperature of the frost-flower-covered sea ice to be higher by 1.3 °C than the surface temperature of bare ice. After approximately 12 h of light snowfall, the leaves of the flower could not carry the weight of the snow anymore and the flower collapsed to the surface of the ice, thereby increasing the sea-ice thickness by 0.5 cm.

Figure 2.9c shows the influence of frost flowers at the surface of sea ice on the temperature evolution within and below sea ice even more clearly. Prior to the formation of sea ice at this depth, the seawater temperature at the advancing front below frost-flower-covered sea ice was lower by 0.7 °C than the temperature at the advancing front below bare ice. Additionally, the seawater temperature below frost-flower-covered sea ice was below the freezing point of the initial seawater, which indicates supercooling of the seawater. When sea ice formed below the frost flowers, the seawater temperature at the advancing front had a value of -2.3 °C; whereas when sea ice formed below bare ice at this level, the seawater temperature had a value of -1.9 °C. After ice formation, the difference in the propagation of the temperature signal is striking. It took 9.72 h for the frost-flower-covered sea ice at this level to reach a temperature of -3 °C after formation, whereas the bare ice reached -3 °C within only 5.89 h after its formation. After the snowfall and an accompanied increase of air temperature, the temperature of both ice types increased. Additionally, the frost flowers at the surface of the sampling hole had spread out horizontally to cover almost the entire hole, which is why also the bare ice was influenced by frost flowers at the surface. However, taking the onset of the increase in air temperature after 57 h as the startpoint, the frost-flower-covered sea-ice temperature had increased by 0.38 °C after 6 h, whereas the bare-ice temperature had increased by 0.9 °C after 6 h. Hence, bare ice not only reaches lower temperatures faster, it also reaches higher temperatures faster.

2.5.2 Temperature evolution in the lab

To study the difference between the surface-temperature evolution of frost flowers and bare ice that formed under the same environmental conditions, I used the infrared camera described in section 2.3. It was fortunate that only one single flower formed in the study area of the infrared camera, since this offered the opportunity to clearly distinguish between the regions of the frost flower and bare ice in the infrared pictures.

In previous studies it was found that the surface temperature increased by 4-6 °C after the authors cleared the surface of flowers [Martin *et al.*, 1996].

However, to measure how the surface temperature of frost flowers changes compared to the change of the surface temperature of bare ice during melting, I did not remove the flower.

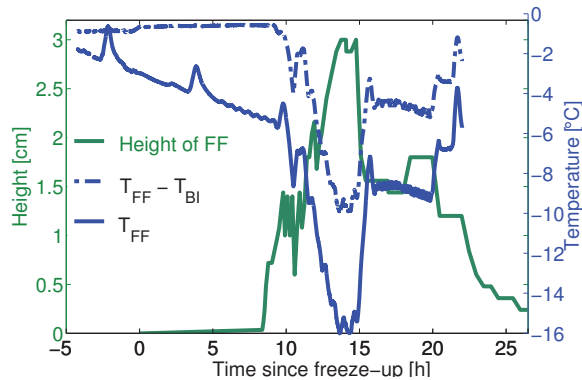


Figure 2.10: Difference between surface temperature of frost flower and bare ice (dash-dotted line) in relation to the size of a frost flower (green line). The solid blue line shows the surface temperature of the frost flower (FF) alone.

The difference between the surface temperature of the frost flower and the surrounding bare ice is shown in figure 2.10. Both the increase and decrease of the size of the flower are accompanied by an increase and decrease of the surface temperature of the flower, i. e., the temperature difference between frost-flower-covered ice and bare ice is linearly dependent on the size of the frost flower.

Fifteen hours after freeze-up the air temperature was raised to induce melting and the flower disappeared within 15 h. At the sea-ice surface, it left behind irregularities in the form of ice clumps and a brine pool (i. e., the frost-flower meltwater). The temperature of the frost-flower meltwater was lower by approximately $0.9\text{ }^{\circ}\text{C}$ than the surface temperature of the surrounding bare ice (see figure 2.11).

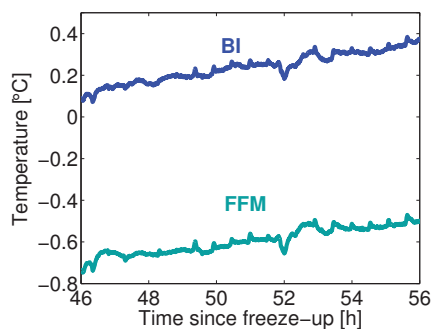


Figure 2.11: Surface temperature of the frost-flower meltwater (FFM) after complete melt of the frost flower and the surface temperature of the surrounding bare ice.

2.5.3 Salinity observations in field and lab

During both the field study and the laboratory experiments, the different environmental conditions during freeze-up led to different salinities of the frost flowers and their roots. The results of the field-salinity measurements of frost flowers and their roots from the three sampling holes (see section 2.2 for details) at different stages of their growth are summarized in table 2.3.

Date of year 2010	Elapsed time [d]	Flower salinity [g/kg]	Root salinity [g/kg]
hole 1 - freeze-up on 13 March			
18 March	5	75.6	-
<i>general increase of ambient air temperature + snowfall</i>			
21 March	8	27.64	29.55
22 March	9	17.58	-
hole 2 - freeze-up on 17 March			
18 March	1	50.64	34.26
18 March	1.5	59.46	-
<i>general increase of ambient air temperature</i>			
19 March	2.5	46.11	38.94
<i>snowfall</i>			
22 March	5	25.46	-
hole 3 - freeze-up on 18 March			
<i>snowfall</i>			
20 March	1.5	49.5	40.15
20 March	1.5	37.7	33.36

Table 2.3: Salinity of frost flowers and their roots taken in NW Greenland in March 2010.

Highest salinities of frost flowers were measured during the large-gradient regime (see table 2.3, values on 18 March). After the changeover to the weak-gradient regime, the salinity values were lower. Snow accumulating at the surface of frost flowers led to a further decrease of the salinity. In summary, salinities were higher for shorter growth times and under the large-gradient regime.

As described in section 2.2, I did a horizontal section along a sampling hole 1.5 days after freeze-up of the hole to study if there exists an interdependence between the salinity of frost flowers and the salinity of the underlying sea ice. This happened during the changeover from the large-gradient regime to the weak-gradient regime. Two frost flowers grew within a distance of approximately 20 cm of each other at the surface of the sampling hole. Since holes sawn into already existing sea ice are not free from the influence of thick sea ice close to the sides, I only consider measurements in a distance of ± 25 cm from the center of the hole. However, the influence of the thicker sea ice close to the sides was there and led to an earlier freeze-up and hence a higher value for the sea-ice thickness of the sampling hole at the sides.

One of the frost flowers grew on the thicker sea ice close to the sides. This

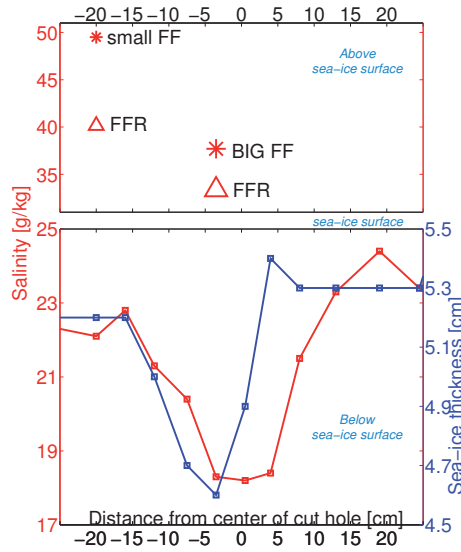


Figure 2.12: Salinities of two frost flowers, their roots, and ice cores; together with the thickness of the underlying sea ice. The samples were taken along a horizontal section of 90 cm 1.5 days after freeze-up of the sampling hole.

flower was smaller⁹ than the other flower¹⁰, which grew close to the center of the hole, where sea ice was thinnest. The center of the sampling hole was least influenced by thick sea ice from the sides and froze over last.

Both flowers were covered with snow. The small frost flower and its root were saltier than the big frost flower and its root (see figure 2.12, upper panel). The salinity of the small frost flower was 11.8 g/kg higher than the salinity of the big frost flower. Additionally, the salinity of the sea ice below the small flower was higher by 3.8 g/kg than the sea ice below the big flower (see figure 2.12, lower panel).

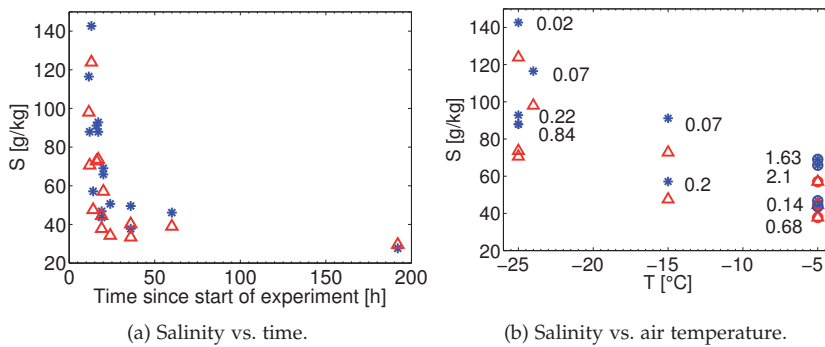


Figure 2.13: Salinity of frost flowers and frost-flower roots versus time (a) and versus the ambient air temperature (b). In (b), the weight of frost-flower samples in gram is indicated. Circled values indicate samples during melting.

⁹ Dimension of 6 x 10 x 2.4 cm in width, length and height, respectively
¹⁰ Dimension of 9 x 12 x 2.9 cm in width, length and height, respectively

Complementary to the field measurements, several samples of frost flowers and their roots were analyzed during the laboratory experiments. Figure 2.13 summarizes the results of both the field and laboratory studies. Contrary to the statement of previous studies [Roscoe *et al.*, 2011], figure 2.13a shows a *decrease* in salinity with age of the frost flowers. Due to the sparse dataset, the dependency between the salinity of frost flowers and the ambient air temperature is difficult to determine, but the curve progresses monotonically. The salinities were higher at lower temperatures (see figure 2.13b). This corresponds with the results of earlier studies [Martin *et al.*, 1995]. Again, I find the opposite to results of Roscoe *et al.* [2011] concerning the time dependence of the salinity—the weight of the flower, which represents its size, is indicated besides the flower-salinity values in figure 2.13b. The weight also represents the growth time, since the frost flowers steadily increased their size during freezing once they formed. During my experiments, the salinity was higher for younger frost flowers.

For all experiments I carried out both in the field and in the laboratory, I find the difference between the salinity of the frost flowers and their roots to decrease from approximately 20 g/kg during freezing to 10 g/kg or lower during melting.

2.5.4 Morphology observations in field and lab



Figure 2.14: The figure shows a stellar-plate like frost flower that started to grow during the night of 16 March. Note the small single ice crystals in the lower left corner. The sea ice below frost flowers appeared milky and was almost free of air-bubbles.

FIELD Under the weak-gradient regime, the protruding sea-ice platelets on which the frost flowers grew were significantly bigger than under the large-gradient regime. The skim layer was significantly thicker during the weak-gradient regime than during the large-gradient regime (see also section 2.4).

Once the frost flowers had formed, their further growth was characterized by an accumulation of smaller and thinner crystals on top of older crystals. Exemplarily, figure 2.14 shows a stellar-shaped flower that grew on a sampling hole during the large-gradient regime. The older stellar-shaped crystals in the lower parts of the flower appeared more robust, thicker, and darker than the younger crystals in the upper parts of the flower. The sea ice below frost flowers appeared milky and was almost free of air-bubbles. It was harder than the surrounding bare ice (investigated while screwing the ice screw to take small ice cores).

LABORATORY During Expt2, I recorded a complete life cycle of a frost flower. In figure 2.15a we see the protruding condensation site on which the flower started to grow. Within only three hours, the flower increased its size from 0.5 cm to 4.8 cm (figure 2.15b). 16 h after freeze-up the melting process was induced, and approximately 22 h after freeze-up the frost flower had collapsed (figure 2.15c). After another 20 h the frost flower was gone and a brine pool had formed that dissolved the underlying sea ice (figure 2.15d).

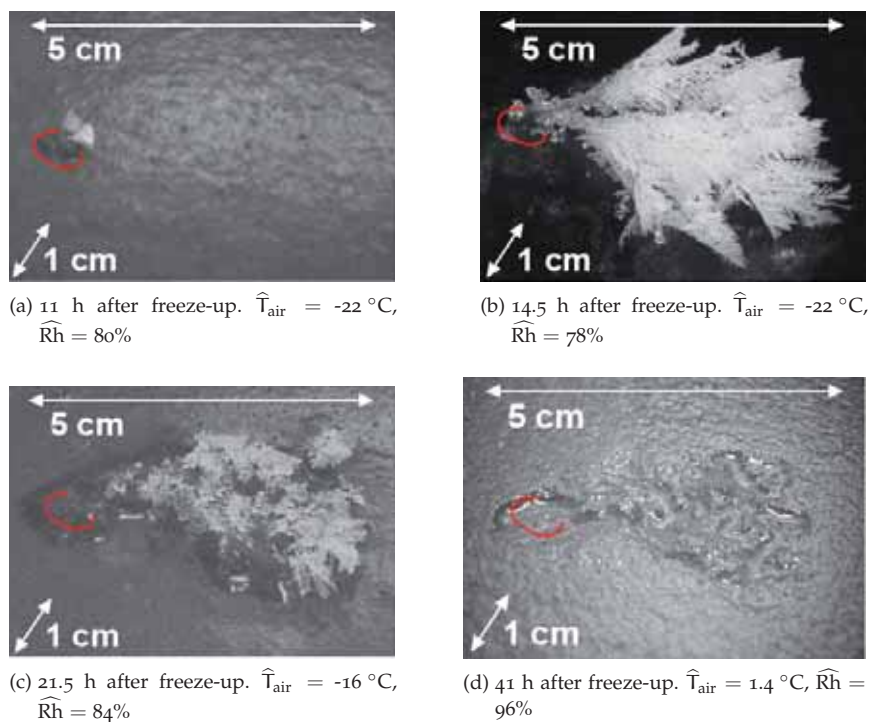


Figure 2.15: The life cycle of a frost flower. Within only 3 hours the flower increased its length from 0.5 cm (a) to 4.8 cm (b). 8 h after inducing the melting process the flower had collapsed (c). Finally, a brine pool formed that dissolved the sea ice below (d). The protruding **condensation site**, i. e., the **frost-flower root (FFR)** is encircled in red.

The morphology of the sea ice that grew below the frost flower was studied by carefully sawing out the piece of sea ice on which the flower had grown. The previously frost-flower-covered ice was much more fragile than the surrounding bare ice. Immediately after taking it out, a photograph and an infrared picture were taken to study the structure and the temperature of frost-flower-covered sea ice.

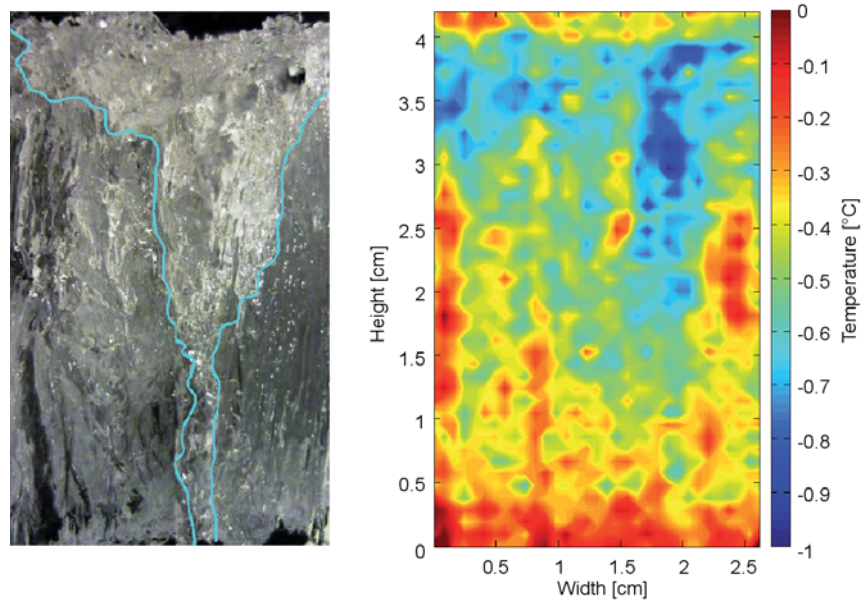


Figure 2.16: Vertical section through sea ice that was influenced by frost-flower growth and melt. Left panel: morphology. Right panel: surface temperature.

The result is shown in figure 2.16. First, the morphology below the flower differed greatly from the bare-ice morphology. Whereas the bare ice showed a typical columnar structure (which can be seen on the left hand side of the left panel in figure 2.16), the structure within the ice that grew below the flower was funnel-shaped. The extension of the funnel in the upper part coincided with the former size of the flower on top of the ice. Additionally, there was a connection from the lower part of the funnel to the underlying seawater via a brine channel. Comparing the temperature within the funnel with the temperature of the columnar ice besides (figure 2.16, right panel), the temperature within the funnel was lower by $0.6\text{ }^{\circ}\text{C}$. This indicates that it was filled up with the salty frost-flower meltwater that had a lower melting point than the fresher sea ice, which implies that the frost-flower meltwater dissolved the underlying sea ice. Average values of the temperature of the different components after melt are given in table 2.4.

Component	Temperature
ambient air	$+2\text{ }^{\circ}\text{C}$
sea ice	$-0.2\text{ }^{\circ}\text{C}$
frost-flower meltwater	$-0.8\text{ }^{\circ}\text{C}$
seawater	$+0.5\text{ }^{\circ}\text{C}$

Table 2.4: Average temperature of flower relevant components after melt.

While taking photographs of the previously frost-flower-covered sea-ice structure, the frost-flower meltwater drained out of the funnel through the brine channel. At the end of the experiment, the salinity of the sea ice that was

influenced by frost-flower growth and melt was lower by 1 g/kg than the salinity of the surrounding bare ice.

2.5.5 Discussion

GROWTH PROCESSES Once a frost flower has formed, the further growth is nothing else than the nucleation of further vapor particles onto the frost-flower tips/skeleton. This means that when the flower is growing, more fresh water freezes onto the flower, which finally *must* decrease the salinity of the flower. While the frost flowers increase their size above the sea-ice surface, the ice below is growing, which leads to a decrease of the temperature gradient between the sea-ice surface and the atmosphere. Since this temperature gradient determines the height and the existence of the supersaturated layer of vapor above the sea-ice surface, the supersaturated layer of vapor disappears and limits the height into which the frost flowers can grow. Moreover, the growth of frost flowers leads to an additional increase in temperature below frost-flower covered ice, since the frost flowers isolate the underlying sea ice from the cold atmosphere. Additionally, it could be the temperature increase that leads to the observed decrease of the frost-flower salinity with age, since the increase is very likely to be accompanied by a widening of the capillaries within the frost-flower skeleton and a release of the salty brine into the underlying sea ice.

The enhanced growth of the hsf-platelets (i. e., the frost-flower roots) which is caused by their higher thermal conductivity, leads to an enhanced expulsion of salty brine into the underlying ocean. This explains the lower seawater temperature at the advancing front below frost-flower-covered ice prior to ice formation compared with the seawater temperature below bare ice (see section 2.5 and figure 2.9c). Another explanation could be the existence of a brine channel right below the flower, so that the thermistor measured the temperature of brine within a channel. In that case the higher brine salinity would have caused a later freezing at the advancing front 5 cm below the flower. However, all this is speculation and needs to be substantiated during additional lab and field experiments.

To summarize, the lower freezing point of seawater with a higher salinity causes the accumulation process of new sea ice below frost flowers to be more slowly than the accumulation of new sea ice below bare ice. Additionally, the frost flowers on top of sea ice insulate the ice from the cold air and cause higher temperatures within the frost-flower-covered sea ice, which further slows down the growth of frost-flower covered ice relative to bare ice.

MELT PROCESSES Snow covering the surface of frost flowers leads to a widening of the capillaries within the flowers and their roots, accompanied by a release of the salty brine into the seawater throughout the sea-ice layer. One could argue that the decrease of the frost-flower salinity after snowfall is just because of the mixture of the frost flower with snow. But since the salinity of the frost-flower roots decreases too (and the root is *not* directly affected by the snow), it likely is the release of salty brine into the underlying sea ice and the ocean that leads to a decrease in the frost-flower salinity.

The difference between the salinity of frost flowers and their roots decreases from approximately 20 g/kg during freezing to 10 g/kg or lower during melting. This can be explained by the weakening of capillary forces due to

the widening of the capillaries as the local temperature increases, which indicates a downward transport of salty brine into the underlying sea ice.

When frost flowers collapse and finally melt, they form a brine pool (the frost-flower meltwater) which is much saltier than the underlying sea ice that has a higher melting point. Hence, the frost-flower meltwater flows downwards and dissolves the underlying sea ice, which finally leads to different morphologies of frost-flower-covered sea ice compared with the morphology of bare ice.

The observations imply that the dissolution of sea ice by the frost-flower meltwater has a strong impact on the rapidity of the sea-ice melting process. The salinity of the sea ice on which the flowers grew is important, because a larger salinity difference between the frost-flower meltwater and the sea ice will lead to faster dissolution and thereby faster melting of the sea ice. Even though bare ice reaches higher temperatures faster (see section 2.5), which implies that bare ice should melt faster than frost-flower covered ice; in the end it is the salinity of the frost flowers that dissolves the underlying sea ice and thereby increases its permeability and its interaction with both the warm ocean and the atmosphere, which finally leads to a faster melting of frost-flower-covered sea ice.

SHORT NOTICE ON SKIM LAYERS Since the formation of skim layers has not been explained satisfactory in the past, I will try to make a first step into a clarification of the formation process with this short notice.

Given the different observed thicknesses of skim layers (*Perovich and Richter-Menge* [1994], this work) and that there was no skim layer in Expt2, I suggest that besides the temperature gradient between the ocean and the atmosphere, a decisive parameter for the formation of a skim layer at all is the turbulence of the ocean below the forming sea-ice surface. Under a large temperature gradient, the initial formation of a sea-ice layer is very fast. As observed during the field study, the solid fraction of the sea-ice surface is higher (which means the surface is much harder and more stable) and quickly inhibits further direct interaction between the oceanic boundary layer and the atmosphere. This is why columnar ice grows earlier and why the skim layer is thinner than under a lower temperature gradient, where a slushy ice-brine mixture conglomerates into a thicker skim layer. The higher solid fraction leads to thinner capillaries and higher salinities of the skim layer. Hence, the skim layer is a residual of the initial stages of sea-ice formation and represents the environmental conditions during freeze-up.

2.6 THE INFLUENCE OF FROST FLOWERS ON SEA-ICE THICKNESS

In the previous sections, I have shown which influence frost flowers have on the temperature, salinity, and morphology evolution of the underlying sea ice. The question remains whether this is a marginal effect or whether frost flowers have a major impact on the evolution of sea-ice thickness.

To get a basic idea of the influence of frost-flower fields on the evolution of the sea-ice thickness, I used a simple conceptual model [*Semtner*, 1976] and used the increase in temperatures within frost-flower-covered sea ice measured in the field (see section 2.5) and applied this frost-flower-caused temperature increase to the surface temperature of bare ice I measured in the laboratory. The model is based on the calculation of the heat flux at the

bottom of the ice via

$$Q_b = -k \cdot \frac{T_s - T_b}{h}, \text{ with} \quad (2.1)$$

Q_b heat flux at bottom of ice

k heat conductivity

T_s surface temperature

T_b bottom temperature

h sea-ice thickness,

which then is used to calculate the change in sea-ice thickness via

$$\Delta H = \frac{Q_b}{\rho L} \cdot \Delta t, \text{ where} \quad (2.2)$$

ΔH change in sea-ice thickness

ρ sea-ice density

L latent heat of fusion of sea ice

Δt time step.

For the surface temperature, I used the temperature of bare ice measured by the infrared camera during the laboratory experiment. The bottom temperature was calculated as the freezing-point temperature according to the salinity of the seawater 8 cm below the ice. The heat conductivity and sea-ice density were calculated according to the temperature of the respective time step.

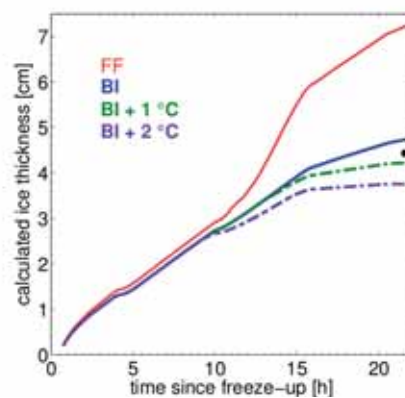


Figure 2.17: Ice thicknesses calculated from the surface temperature of a **frost flower** (FF) and the surrounding **bare ice** (BI) using SemtnerZero. Black dot indicates measured ice thickness. See text for details.

Figure 2.17 shows the result for an averaged bulk salinity of 25 g/kg, which is a realistic assumption for sea ice at this stage of growth. First, I calculated the ice thickness for the original surface-temperature evolution of the bare ice. The final ice thickness agrees well with the measurement I did with a millimeter-scale ruler (blue, solid line in figure 2.17).

To then simulate the influence of frost-flower coverage and the accompanying increase of the surface temperature on the evolution of the sea-ice thickness, I made calculations for two different assumptions:

1. According to the field measurements (see section 2.5), I introduced an increase of the surface temperature of $0.7\text{ }^{\circ}\text{C}$ for the early stages, and an increase of $1\text{ }^{\circ}\text{C}$ for the later stages of frost-flower growth (green, dash-dotted line in figure 2.17). In this scenario the sea ice is 0.5 cm thinner than it would have been without frost flowers on top after 12 h of frost-flower growth.
2. On the basis of the measurements of *Martin et al.* [1996], who measured the temperature of the surface where a flower grew to be higher by $4\text{--}6\text{ }^{\circ}\text{C}$, I introduced a temperature increase of $1\text{ }^{\circ}\text{C}$ for the early stages, and $2\text{ }^{\circ}\text{C}$ for the later stages (purple, dash-dotted line in figure 2.17). In this scenario the sea ice is 0.9 cm thinner than it would have been without frost flowers on top after just 12 h of frost-flower growth.

IMPORTANCE FOR SATELLITE DERIVED SEA-ICE THICKNESS In addition to the isolating effect of frost flowers that leads to thinner sea ice, satellite-measured sea-ice-surface temperatures might cause an extra overestimation of the actual sea-ice thickness. The laboratory measurements have shown that the surface temperature of frost flowers can be lower by $10\text{ }^{\circ}\text{C}$ than the surface temperature of bare ice. To study the effect of this temperature difference that causes satellite-measured sea-ice temperatures to be too cold, which leads to an overestimation of the sea-ice thickness, the thickness was calculated for the surface temperature of the frost flower too (red, solid line in figure 2.17). The results imply that a sea-ice thickness that is derived from a satellite-inferred temperature can result in an overestimation of up to 3.5 cm after 12 h already. The results are summarized in table 2.5.

Based on surface temperature of ...	Calculated ice thickness	Difference to thickness derived from T_{surf} of FF
FF	7.3 cm	0
BI	4.7 cm	-2.6 cm
BI + $0.7\text{--}1\text{ }^{\circ}\text{C}$	4.2 cm	-3.1 cm
BI + $1\text{--}2\text{ }^{\circ}\text{C}$	3.8 cm	-3.5 cm

Table 2.5: Influence of frost flowers on ice thickness 12 h after nucleation of frost flowers.

2.7 SUMMARY AND CONCLUSIONS

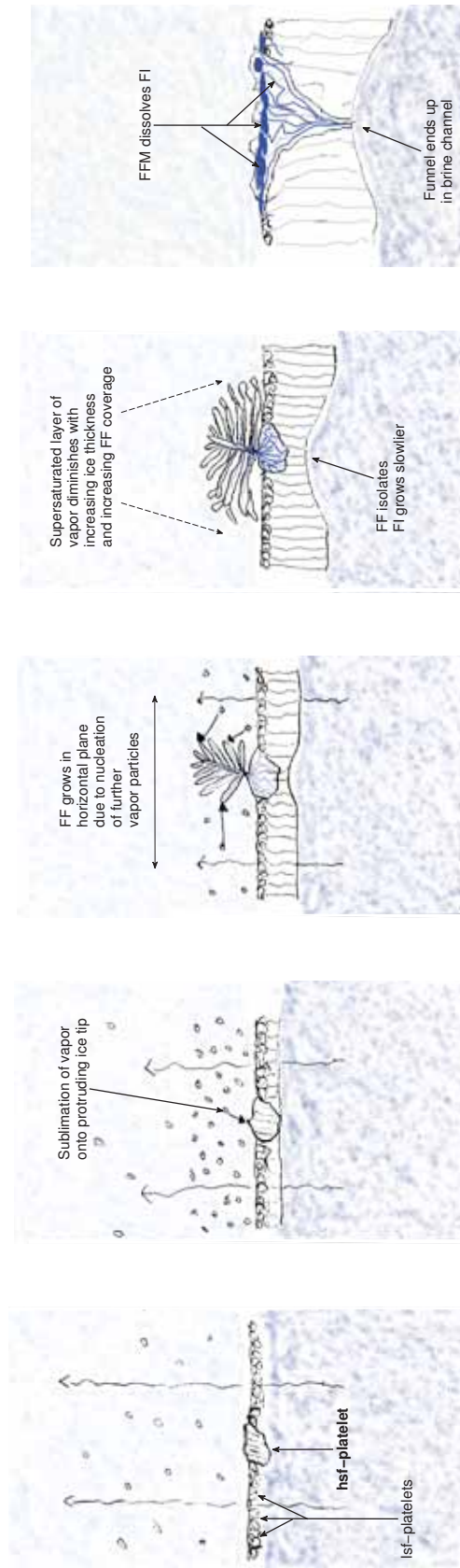
In this chapter, I have investigated the temperature, salinity, and morphology evolution of frost flowers and the underlying sea ice, based on measurements carried out in the field and the laboratory. My main goal was to achieve an understanding of the physical processes accompanying the formation, growth, and melt of frost flowers and their interaction with the underlying sea ice (see figure 2.18). I conclude the following:

1. Frost flowers form on sea-ice platelets protruding from the sea-ice surface, and that accidentally might have a higher solid fraction and a higher thermal conductivity than the surrounding sea-ice platelets. The salinity, size, and structure of frost flowers are determined by the size and the structure of the sea-ice platelets together with the temperature gradient between the atmosphere and the water/ice surface

during the initial stages of sea-ice formation. Larger temperature gradients during the initial stages lead to a higher salinity of both sea ice and frost flowers.

2. The formation and growth of the frost-flower nucleation sites, which form the frost-flower roots later on, is accompanied by an enhanced expulsion of salty brine into the ice-ocean-boundary layer.
3. The salinity of frost flowers decreases with age and depends on the bulk salinity of the underlying sea ice.
4. Frost-flower-covered sea ice grows more slowly and melts faster than bare ice. During their growth, frost flowers insulate the sea-ice surface from the atmosphere and lead to higher temperatures within the underlying sea ice compared to temperatures within bare ice. During melting, the highly saline frost-flower meltwater dissolves the underlying sea ice and increases the permeability of the ice, which leads to a faster melting process.

The ongoing retreat of perennial sea ice is likely to be accompanied by an increase in the areal fraction of frost-flower-covered sea ice. This will lead to a more rapid melting process of first-year sea ice, which goes along with a larger areal fraction of open seawater—not only in September.



(a) Large temperature gradient between atmosphere and ocean causes ice crystals to grow at air-seawater interface and determines size of hsf and lsf-platelets and accompanying enclosement of saline brine into their matrices. Faster growth of hsf-platelets lead to both thinning of capillaries and an accompanied increase in brine salinity within hsf-platelets, and an enhanced expellement of salty brine into the ocean. hsf-platelets are less dense and float on and within thin sea-ice layer.

(b) Evaporation of seawater throughout thin sea-ice layer leads to region of supersaturated vapor above ice surface. Vapor sublimates onto protruding ice tips of hsf-platelets. Size of frost flower determined by height of vapor layer. Structure determined by temperature gradient during hsf-platelet formation.

(c) Temperature dependent capillary forces bring up salty brine from hsf-platelet into frost-flower skeleton. Growth of frost flower is nucleation of further vapor onto frost-flower skeleton.

(d) Growth of sea ice and increase in frost-flower-areal fraction decreases supersaturated layer of vapor, since temperature gradient gets weaker. Growth of frost flower stops. The frost flowers isolate the sea ice from cold atmosphere. Frost-flower-covered sea ice grows slower than bare ice.

(e) During melt, salty frost-flower meltwater dissolves the underlying sea ice, thereby increasing its permeability. Hence, the ice gets more vulnerable to both dynamics and thermodynamics of adjacent layers. Frost-flower covered sea ice melts faster than bare ice.

Figure 2.18: Life cycle of a frost flower.

Part III

SEA ICE CRIES

It is such a secret place, the land of tears.

— The little Prince
Antoine de Saint-Exupéry

THE DESALINATION OF MELTING FIRST-YEAR SEA ICE

ABSTRACT

Based on field observations of salinity and temperature in both sea ice and ocean, I investigate the desalination of sea ice during its first melt cycle.

The data were obtained during a field study at the West coast of Greenland from 15 April 2010 until the complete melt of the ice on 20 May 2010. Ocean salinity and temperature 50 cm below the ice surface were recorded continuously until all ice had melted. Sea-ice salinity and temperature were obtained from five ice cores that were taken during the period from 15 April to 7 May.

The observations suggest that the major desalination of first-year sea ice during its winter-spring-summer transition is driven by gravity drainage that is enabled and enhanced by a combination of the high bulk salinity of first-year sea ice and the overall increasing temperatures caused by polar sunrise. In contrast to desalination by gravity drainage in winter, this kind of gravity drainage is triggered by a significant increase in sea-ice permeability. At the end of the major desalination, the whole ice column had equilibrated to an average temperature of -1.7 °C, and an average bulk salinity of 6 g/kg. Such a bulk-salinity can also be found in young, multi-year sea ice. Flushing occurred in our field experiment four days after the gravity-drainage driven desalination.

Hence, the desalination of sea ice during its first melt cycle is driven by permeability drainage. The permeability increase due to this process might be a prerequisite for flushing to occur at all.

3.1 INTRODUCTION

First-year sea ice, which has become the prevailing sea-ice type in the Arctic and has long played an important role in the Antarctic, is considerably saltier and thinner than multi-year sea ice. It is saltier because it did not yet experience summer melt, and it is thinner because it did not experience the multiple-year cycles of additional ice formation at its bottom. Here, I investigate processes driving the desalination of sea ice during its transition from first-year sea ice to either young multi-year sea ice or complete melt.

First-year sea ice is the prevailing sea-ice type in the Antarctic, where offshore winds present the establishment of a substantial multi-year sea-ice cover. In the Arctic, first-year sea ice has now become the prevailing sea-ice type, since the recent observed reduction in Arctic sea-ice extent has been accompanied by a substantial loss of multi-year sea ice in all seasons [Johannessen *et al.*, 1999; Comiso, 2002; Nghiem *et al.*, 2007; Maslanik *et al.*, 2007; Kwok *et al.*, 2009; Maslanik *et al.*, 2011]. The formerly multi-year-ice areas in the Arctic are replenished with first-year sea ice, which makes the Arctic ice cover as a whole more susceptible to future rapid declines [Maslanik *et al.*, 2007]. That the age of sea ice explains more than half of the variance in observed and simulated summer sea-ice extent [Rigor and Wallace, 2004] is but one example of the necessity to improve the simulations of a saltier and thinner sea-ice cover under various atmospheric and oceanographic conditions, and to understand how the changing atmosphere-ice-ocean system adjusts to external perturbations. This improvement of model formulations is impossible without measurements above, within, and below forming, growing, and melting first-year sea ice. With this chapter I present measurements of the bulk-salinity evolution of melting first-year sea ice.

The bulk salinity of sea ice is determined by the mass fraction and the salinity of the highly saline brine that is surrounding the freshwater-ice matrix. Any change of the brine fraction influences the physical properties of the ice itself and the ocean below, including ice-thermodynamic properties and ocean density [Schwerdtfeger, 1963; Weeks and Assur, 1967; Ono, 1975; Grenfell and Maykut, 1977; Aagaard *et al.*, 1981; Morey *et al.*, 1984; Goosse *et al.*, 1997; Carmack, 2000; Stössel *et al.*, 2002]. Traditionally, the bulk salinity of sea ice is obtained by the extraction of ice cores [e.g. Eicken *et al.*, 2009; Weeks, 2010]. An extensive study of ice-core data obtained from first-year sea ice was carried out by Kovacs [1996], who reexamined ice-core data obtained from a variety of both Arctic and Antarctic places [Cox and Weeks, 1974; Kovacs, 1996] and both studies surprisingly found that the general amount of scatter between Arctic and Antarctic data was quite small with strong general trends [Cox and Weeks, 1974; Kovacs, 1996; Weeks, 2010]. However, due to the inaccessibility of polar regions that are covered with thin, melting first-year sea ice, ice-core data obtained prior to the complete melt of first-year sea ice to my knowledge are nonexistent. Hence, an investigation of the processes driving the desalination of first-year sea ice during melting was almost impossible in the past. However, we had the opportunity to use as a scientific base a sailing boat that was overwintering in a small Greenlandic bay, which allowed for ice-core sampling right up to the complete melt of thin (≈ 30 cm), first-year sea ice. Based on oceanographic and ice-core data, I here investigate which processes drive the desalination of first-year sea ice during its transition from winter to summer.

To date it is generally agreed that two processes dominate the loss of brine

from sea ice—gravity drainage during winter, and flushing during summer [Notz and Worster, 2009; Weeks, 2010; Hunke et al., 2011].

Gravity drainage describes the loss of brine from sea ice by convective overturning with underlying sea water. It was suggested to be the most important desalination process in winter, when the cooling of sea ice by the atmosphere leads to an unstable brine-density profile throughout the whole ice column with the brine in the top parts being more dense. Once the Rayleigh number (which can be interpreted as the ratio between available potential energy of the brine and the energy necessary for brine convection) exceeds a critical value, convection of the brine might occur, with the brine that drained out being replaced by the seawater below [Untersteiner, 1968; Cox and Weeks, 1975; Wettlaufer, 1997; Worster, 2000; Notz and Worster, 2009].

Flushing leads to additional loss of brine from sea ice during summer. It describes the percolation of fresh surface meltwater through the whole ice column, thereby washing out the salty brine. Hence, it is dependent on the permeability of the ice. Although the main path of the percolating meltwater is vertical, flushing was found to also have a significant horizontal component [Untersteiner, 1968; Eicken et al., 2002; Freitag and Eicken, 2003; Eicken, 2003; Eicken et al., 2004].

Recently, it was suggested primarily based on modelling studies that sea ice can also lose brine by gravity drainage during periods of warming [Jardon et al., in press; Griewank and Notz, 2012]. Here we provide the first direct evidence that indeed, such desalination happens in the field. We find that during warming of the ice cover, gravity drainage can be triggered by an increase in sea-ice permeability, well before the surface state would allow for desalination by flushing.

3.2 SETUP AND METHODS

To study how sea ice desalinates during its first melt cycle, we chose a small bay at the Western coast of Greenland (72.79°N, 56.06°W), 5 km beeline to the airport of the settlement Upernavik. The bay itself belongs to an island within the fjord landscape of Western Greenland and covers an area of 120x100 m² with an average water depth of 8 m. A sailing ship overwintering in the bay provided a basis for our scientific equipment. Measurements of an acoustic Doppler current profiler (ADCP)¹, which we deployed four months prior to the study described here, showed oceanic currents to be almost absent. Given that the surrounding mountains additionally protected the bay against wind (see figure 3.1), this place turned out to be a perfect site to study the desalination of sea ice grown under calm environmental conditions. By the end of March 2010 a sea-ice cover with an average thickness of 33 cm had formed that was homogeneous allover the bay and did not show any rafts or ridges. We deployed air temperature² and humidity³ sensors at a height of 1.5 m above the ice surface. To obtain the temperature and salinity evolution within the melting ice, one of the overwinterers agreed to take ice cores occasionally until the beginning of May 2010 (the red line in figure 3.1 marks the section along which the cores were taken). A conductivity-temperature (CT) sensor⁴ was arranged 50 cm below the ice

¹ Workhorse Sentinel, 1200 kHz; velocity accuracy: ± 0.3 cm/s

² Campbell 43347 RTD temperature probe with Campbell 43502 aspirated radiation shield

³ rotronic hygrometer MP 100 A with RS 12 T radiation shield

⁴ SeaBird Electronics, SBE37

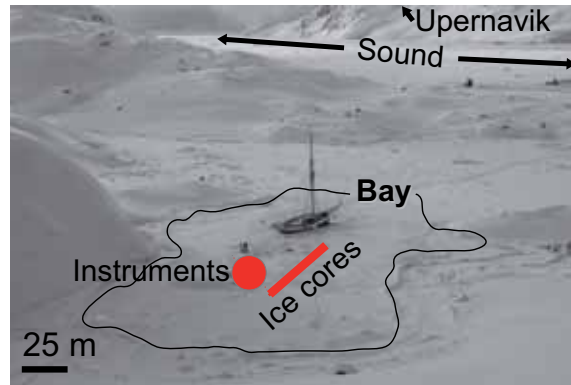


Figure 3.1: Semi-enclosed bay in which we carried out the field experiment. Instruments were deployed within the region marked with a red dot. The red line marks the section along which ice cores were taken.

surface to measure the oceanic salinity and temperature evolution below the melting ice (the position of the instruments is marked as a red dot in figure 3.1.). The sampling interval of air temperature, humidity, and CT sensors was set to 30 s.

When we left the site after deployment of our instruments at the end of March, the ice was smooth, covered with approximately 10 cm of snow, and had an average thickness of 33 cm. The sound between the bay and the settlement Upernavik was ice covered (see figure 3.1). On 9 May 2010 we returned to the site to check the battery status and to prepare the recovery of the instruments by the ships crew. This time, the sound was ice free, but the bay was still ice covered with an average ice thickness of 30 cm and a continuous snow cover of 10 cm. However, the ice-bottom structure had changed completely compared to March. It was covered with holes all over with a diameter of approximately 1-3 cm. The holes were filled with algae that served as food for copepods and amphipods. Touching the ice caused a feeling comparable to touching styrofoam. Only three days later, the day of our departure, the state of the ice surface had completely changed (see figure 3.2). There were no melt ponds, but the surface got wet and hence



Figure 3.2: During a period of three days, the sea-ice-surface structure changed significantly from being continuously snow covered to being covered by a wet snow /water surface.

darker, and it was not quite safe anymore to walk on the ice; with every step we were breaking approximately 10 cm throughout the snow into the

ice. The snow was not continuous anymore, but rather a thin snow surface with the region between the snow surface and the ice surface being like a snow skeleton filled with water.

On 20 May 2010 all ice had melted and the instruments were recovered by the ships crew. A total of five ice cores were taken during the period from 15 April to 7 May, and bulk salinity and temperature of these cores were determined using standard methods [see *Eicken et al.*, 2009].

3.3 DESALINATION OF THE WHOLE ICE COLUMN OBSERVED FROM ICE CORES

The temperature and bulk-salinity evolution as obtained from the ice cores are shown in figure 3.3. Most striking is a period of 11 days (25 April to 6 May), during which a general temperature increase occurred at all levels in the ice, and the ice-surface temperature changed from being coldest to being the warmest throughout the whole ice column (see figure 3.3a). The temperature profile of the last ice core shows the temperature to have reached an almost homogeneous temperature of -1.7°C throughout the whole ice column. This general increase of ice temperature was accompanied by a general decrease and equilibration of the bulk salinity throughout the ice column, too (figure 3.3b), showing an almost homogeneous bulk-salinity profile with an average salinity of 6 g/kg—a value which is comparable to the average bulk-salinity value of young, multi-year sea ice. Noteworthy is that while

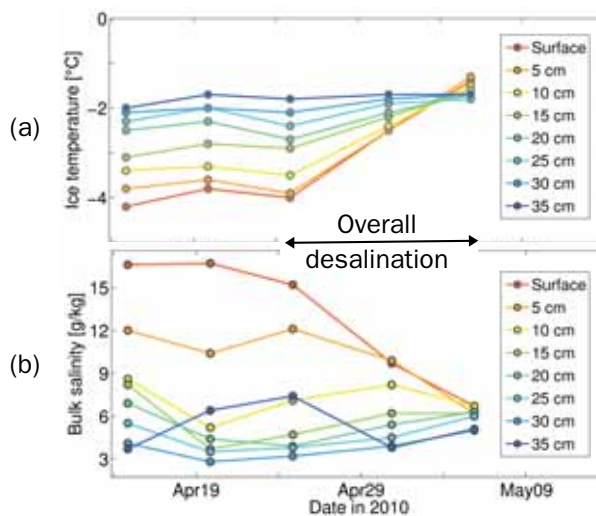


Figure 3.3: (a) Temperature and (b) bulk salinity obtained from ice cores. During a period of 11 days (25 April to 6 May), an overall increase and equilibration to an average ice temperature of -1.7°C was accompanied by a desalination and equilibration to an average salinity of 6 g/kg throughout the whole ice column, which is comparable to the bulk salinity of young, multi-year sea ice.

the bulk salinity in the upper parts of the ice column decreases, the bulk salinity in the lower parts of the ice column slightly increases during the overall desalination (see figure 3.3b, depths of 20–35 cm).

3.4 DESALINATION NOT DRIVEN BY FLUSHING

To date, the only process that has been suggested to drive the desalination of sea ice during summer is flushing (see section 3.1). However, in the following I show that it was *not* flushing that was responsible for the observed overall desalination.

One prerequisite for flushing to occur is surface temperatures that are high enough to melt the snow covering the ice surface. Once this prerequisite is given, the snow meltwater, which usually accumulates in melt ponds, covers large areas of the ice surface. If the ice then is permeable enough, the meltwater percolates through the ice and washes out the salty brine.

Hence, if flushing would have been the process responsible for the observed desalination, the air temperature should have been above 0°C and melt-pond areas should have appeared at the ice surface. But neither was the case—the air temperature during the desalination period was below 0°C (see figure 3.4a), and when we arrived on 9 May, which was 3 days after the last ice core was taken, the ice was still continuously snow covered (see figure 3.2, left panel). Hence, another process than flushing must have driven the overall desalination. However, right *after* the overall desalination, the ob-

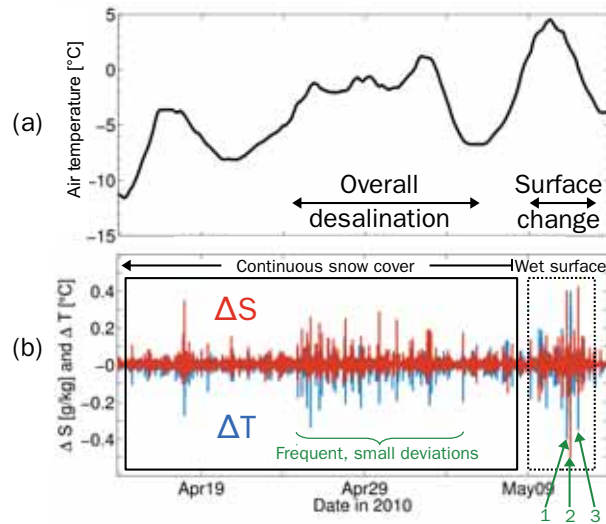


Figure 3.4: (a) Air temperature was below 0°C during the overall desalination (permeability drainage) and above 0°C during flushing. (b) The deviations from oceanic salinity and temperature measured 50 cm below the ice surface, averaged over a sliding window of 2 h, are highest during the observed change of the surface structure, i.e., during flushing (dashed rectangle). The three strongest events are marked with green arrows. More frequent but smaller deviations can be found during the period of the overall desalination, i.e., during permeability drainage (solid-line rectangle). The strong deviation on 17 April was also caused by permeability drainage after a first significant air-temperature increase. See section 3.5 for details.

served change of the ice-surface structure from continuously snow-covered (9 May 2010) to be covered by a wet snow/water surface (12 May 2010) occurred at air temperatures above 0°C and increases the likelihood that flush-

ing finally occurred and led to a further decrease in bulk salinity. Since the sampling of ice cores was too dangerous at that time and we therefore have no ice-core data for the final melting period, I use oceanic salinity and temperature measured 50 cm below the ice surface to investigate if I can identify temperature and salinity signals caused by the outflow of brine and/or meltwater from the ice. In case of a significant positive deviation from averaged oceanic salinity and negative deviation from averaged oceanic temperature, I assume that salty, cold brine was released from the ice above. Contrary, I assume that warm and fresh meltwater ran from the ice if the deviations from averaged salinity are negative, and deviations from averaged oceanic temperature are positive.

Concerning the reliability of this method, we need to consider possible inflows of different water masses, and strong rain or storm events that could have caused disturbances in salinity and temperature as measured by the CT, too. However, the overwinterers did not report on any strong rain or storm events during the period from March to May, and given the near absence of oceanic currents for a period of more than four months as measured by the ADCP prior to the study (see section 3.2), a sudden inflow of different water masses into the bay seems unlikely. Hence, I interpret strong deviations from average oceanic salinity and temperature to be caused by local brine and/or meltwater outflow from the ice above. Deviations from average oceanic temperature and salinity were calculated over a sliding window of 2 h. The result is shown in figure 3.4b. The error of deviations of both temperature and salinity I estimate to be below $0.1\text{ }^{\circ}\text{C}$ and 0.1 g/kg , respectively. Indeed, stronger deviations from average oceanic temperature ($\pm 0.4\text{ }^{\circ}\text{C}$) and salinity (up to $\pm 0.5\text{ g/kg}$) occurred during the period of the surface-structure change compared to earlier periods, where the surface was continuously snow covered (see figure 3.4b, period emphasized by dashed-line rectangle). Moreover, contrary to earlier periods with a continuous snow cover where significant deviations are characterized by an increase in salinity and decrease in temperature, this time three strong deviations of both salinity and temperature appear which fluctuate between increase and decrease (see figure 3.4b, three events indicated by green arrows). We suggest that the first event, characterized by a salinity increase and a temperature decrease indicates that meltwater percolated through the ice and washed out the salty, cold brine in the vertical ($S \uparrow, T \downarrow$). The following second event, which occurred right after the first event, is characterized by a salinity decrease and a temperature increase ($S \downarrow, T \uparrow$) and might indicate that since most of the brine in the vertical was washed out by the first event, not much brine was left and the signals now are dominated by the warm and fresh meltwater ($S \downarrow, T \uparrow$). The third and last strong event during this period occurred 17 h later, and is characterized by a salinity increase and temperature decrease again ($S \uparrow, T \downarrow$). This might substantiate the measurements of *Eicken et al.* [2002, 2004] in that flushing also has a significant horizontal component, assuming that there was time enough for brine cells to rearrange [see also *Light et al.*, 2003] and move together with meltwater from the sides in the horizontal, so that the percolating meltwater washed out the remainder of the brine in the vertical that came from the sides.

Hence, flushing occurred and very likely led to a further decrease of the initial bulk salinity of 6 g/kg that was observed after the overall desalination. But flushing is not the process that has driven the desalination of the whole ice column to a homogeneous bulk-salinity profile that is comparable to the

one of multi-year sea ice.

3.5 DESALINATION WAS DRIVEN BY PERMEABILITY DRAINAGE

In contrast to the three strong deviations from average oceanic salinity and temperature that we observed during flushing, several more frequent, but smaller deviations from oceanic temperature (up to $-0.2-0.3$ °C) and salinity (up to $+0.2-0.3$ g/kg) can be found during the period of the major desalination prior to flushing (see figure 3.4b, period indicated by green brace). This period of 11 days is characterized by a general increase in air temperature (see figure 3.4a), which finally caused the measured temperature increase at all levels in the ice. With a mean value of -2.1 °C, the air temperature was too low to melt the snow at the ice surface. Having excluded flushing as the process driving the major desalination, it seems reasonable to investigate if the process that was suggested to be responsible for the loss of brine from sea ice during winter—gravity drainage—might be important for the desalination of sea ice during this time of the year with increasing solar radiation, i.e., spring and/or summer, too.

In winter, sea ice balances the difference between low atmospheric and comparatively high oceanic temperatures, which causes a temperature gradient within the ice column with temperatures at the ice surface being lower than at the ice bottom. Since the microstructural evolution of sea ice as a system of solid freshwater ice and liquid brine is determined by the adjustment of both components to local temperature changes to maintain phase equilibrium, any temperature gradient is accompanied by a salinity gradient within the encapsulated brine cells, which finally results in an unstable brine-density profile. Dependent on the permeability of the ice, the instability caused by the difference between brine and ocean density can result in brine convection within the ice column, and some of the brine might leave the ice. This desalination process was termed gravity drainage, and the relation between the driving buoyancy of the salty brine relative to the dissipation during convection can be described by the porous-medium Rayleigh number Ra , which is based on the mushy-layer theory [Worster, 1992; Wettlaufer, 1997; Feltham et al., 2006, and references therein]. The Rayleigh number can be calculated as:

$$Ra(z) = \frac{g(\rho_{br}(z) - \rho_{sw})\Pi(\phi_v)(h - z)}{\kappa\mu} , \quad (3.1)$$

where g is acceleration due to gravity, $(\rho_{br}(z) - \rho_{sw})$ is the difference between brine and ocean density, h is ice thickness, z is level in the ice, and κ and μ are thermal diffusivity of and dynamic viscosity of the brine, respectively. The permeability $\Pi(\phi_v)$ can be calculated as a function of the solid-volume fraction ϕ_v following Freitag and Eicken [2003] as

$$\Pi = 10^{-17} (10^3 \cdot (1 - \phi_v))^{3.1} . \quad (3.2)$$

Here ϕ_v can be determined from the measured bulk salinity S_{bu} and ice temperature T as

$$\phi_v = 1 - \frac{\rho_l}{\rho_s} (1 - \phi_s) , \quad (3.3)$$

where

$$\phi_m(T, S_{bu}) = 1 - \frac{S_{bu}}{S_{br}(T)} . \quad (3.4)$$

ϕ_s is the solid-mass fraction, and ρ_l and ρ_s are the densities of the brine and the ice, respectively. The density of the brine is calculated from the measured ice temperature by first determining the local brine salinity via the liquidus relationship (obtained from the phase diagram for sea ice, where the curve connecting the local brine salinity and the local temperature defines the solid-liquid coexistence at constant pressure; in oceanographic parlance, it is simply the salinity-dependent freezing temperature [Weeks, 1998; Wettlaufer et al., 2000; Feistel et al., 2008]⁵); and then using the calculated local brine salinity and measured temperature to determine the brine density.

Once the buoyancy of the brine is sufficient to overcome dissipation, i. e., once convection of the brine can set in, the Rayleigh number exceeds a critical value. However, the value of the *critical* Rayleigh number is still unclear. I am aware of three different values for the critical Rayleigh number, ranging from around 1 to around 10 that are used in different numerical models or were derived theoretically [Worster, 1992; Wettlaufer, 1997; Vancoppenolle et al., 2010; Griewank and Notz, 2012]. Hence, for simplicity and clarity, I here focus on the two directly observed parameters that dominate the loss of brine from sea ice and that both are determined by the ice temperature—the difference between brine and ocean density, and the permeability.

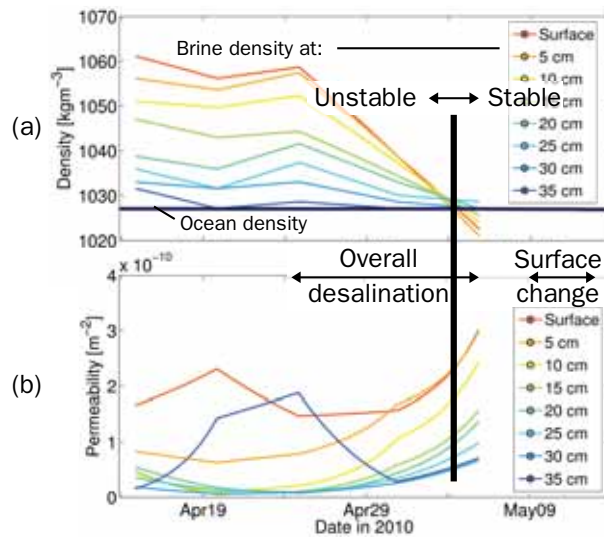


Figure 3.5: (a) Brine density and (b) permeability at different levels in the ice. Once the brine-density profile changed to a stable state, the frequent deviations from average oceanic salinity and temperature stopped (see figure 3.4 (b)). The permeability increased at all levels in the ice.

I find that the general temperature increase at all levels in the ice is accompanied by both a brine-density decrease, and a permeability increase (see figure 3.5). Moreover, I find that the brine-density profile changes from unstable to stable. Once the profile has become stable, the frequent, smaller deviations from average oceanic salinity (+0.2 g/kg) and temperature (−0.2 °C) stop (see figure 3.4 (b)). I suggest that the general temperature increase strongly enhances the rapidity of the melting of the salty first-year sea-ice

⁵ Equation used from: IOC, SCOR and IAPSO, 2010: The international thermodynamic equation of seawater - 2010: Calculation and use of thermodynamic properties

surface. The internal phase changes induced by the warming of the ice cause a change of the brine volume and a stronger interconnection between single brine cells [see also *Light et al.*, 2003]. The downward moving brine further dissolves the freshwater-ice matrix and brine cells interconnect, thereby further increasing the permeability of the ice, which leads to both a decrease of the bulk salinity at the ice surface, and an increase of the bulk salinity in the lower parts of the ice column with some of the brine continuously leaving the ice until an almost homogeneous temperature and salinity distribution is reached and no further deviations from oceanic salinity and temperature occur.

In contrast to gravity drainage in winter, the gravity drainage observed here leads to a significant increase in permeability. To distinguish between both drainage processes, I name the spring-desalination process as permeability drainage. This process might be a prerequisite for flushing to occur at all.

3.6 SUMMARY AND CONCLUSIONS

In this chapter I presented measurements above, within, and below melting first-year sea ice that suggest a new desalination process to occur in spring (see figure 3.6 for a sketch of profiles during different times of the year). The measurements show that the general temperature increase in spring induces warming and hence melting of the saltier upper parts of first-year sea ice, which causes a change in the brine volume and hence a decrease in brine salinity and density. As long as the brine-density profile is unstable, the brine moves towards the ice bottom, thereby increasing the permeability of the ice. I conclude that the saltier the ice is at the surface, the earlier the brine-volume fraction increases to maintain phase equilibrium, the earlier the permeability of the ice increases, and the earlier the ice gets more vulnerable to both atmospheric and oceanic forcings.

The observations described in this study might hold for increasing areas in the Arctic with an increasing fraction of first-year sea ice, as sun is rising and the ice starts to experience its first melt cycle.

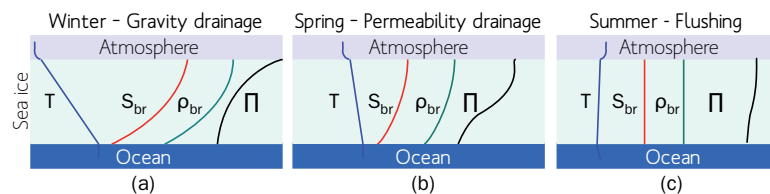


Figure 3.6: Profiles of temperature (T), brine salinity (S_{br}), brine density (ρ_{br}), and permeability (Π) within first-year sea ice during (a) winter, (b) spring, and (c) summer. The warming of the salty ice surface during spring causes melting of the upper ice column. The unstable brine-density profile causes the brine to move towards the ice bottom, thereby increasing the permeability of the ice. This permeability increase in spring might be a prerequisite for flushing to occur at all.

Part IV

SEA ICE RESISTS

Write, write anything: it is all in all probability worthless anyhow, it is never hard to destroy written characters. But it is absolutely to the writing of anything worth while that the mind be fluid and release itself to the task. Forget all rules, forget all restrictions, as to taste, as to what ought to be said, write for the pleasure of it—whether slowly or fast—every form of resistance to a complete release should be abandoned.

— William Carlos Williams

WIRE-HARP MEASUREMENTS REVISITED

ABSTRACT

I present preliminary results of impedance measurements between two thin metallic wires within growing and melting artificial sea ice. The results were obtained from an intermediate version of an instrument developed to measure the bulk-salinity evolution of sea ice in situ.

Since the attempt to use an already existing instrument failed to give reliable results, the electrical setup of the old instrument has been improved and tested in the laboratory. While the old instrument was capable to measure the absolute value of the impedance, the novel development is capable to measure the individual parts of impedance, resistance and reactance, independently.

First results show impedance to be almost exclusively resistive, contrary to assumptions made for the old instrument, where the resistive part was neglected for data interpretation. Impedances measured between individual wire pairs show strong variability even under identical environmental conditions, illustrating the high sensitivity of the wires. Mechanical deformation of the wires by growing ice even under calm laboratory conditions, calls the field applicability of the instrument into question.

However, the instrument is still under electrical and mechanical construction and might give more reliable results in a future setup.

4.1 INTRODUCTION

When seawater reaches its freezing point, sea ice starts to separate from it and immediately moderates and regulates the heat exchange between ocean and atmosphere. The separation process is forced by varying meteorological and oceanographic conditions. Therefore, the arrangement of the two major components of sea ice—solid freshwater ice and liquid salty brine—is heterogeneous, and so are the resulting bulk physical properties of the ice. One of these properties is the bulk salinity, which is determined by the highly temperature-dependent brine-volume fraction and hence the solid-volume fraction of sea ice. The bulk salinity strongly influences the energy transport through the ice, its thermal conductivity and permeability [see e. g. *Perovich et al.*, 1998; *Eicken*, 2003; *Weeks*, 2010, and references therein]. Although this importance has long been recognized by the scientific community, in-situ measurements of the bulk salinity of sea ice are still largely lacking. In this chapter, I discuss the reliability of electrical impedance measurements that were carried out in the past to examine the bulk-salinity evolution of sea ice in situ by using the wire harp [*Notz*, 2005; *Notz et al.*, 2005]. Moreover, I present and discuss intermediate results of impedance measurements obtained during the development of an improved version of this instrument, the Harp3d [*Fontes*, 2009; *Fontes et al.*, 2009].

If available, in-situ measurements of the bulk salinity of sea ice were carried out on perennial sea ice in the majority of cases [see e. g. *Perovich et al.*, 1998; *Eicken*, 2003; *Weeks*, 2010]. However, the predominant mechanism of sea-ice formation in the Arctic is changing from accumulation underneath multi-year sea ice to sea-ice formation starting in open water. This results in an increasing fraction of first-year sea ice, which has a considerable higher salt content than perennial sea ice [*Weeks*, 2010]. This is why measurements of the microphysical properties such as the brine-volume fraction of first-year sea ice are essential to develop and evaluate future numerical sea-ice models.

Traditionally, measurements of the bulk salinity were observed by the extraction of ice cores. Immediately after taking the core, temperature was measured at equidistant intervals, and bulk salinity was obtained from molten samples of the core that was cut into pieces of similar size. However, this method is destructive and error-prone due to the outflow of brine during core extraction. In contrast, observations of the microstructural evolution of sea ice by using electrical methods are more promising, as these methods are non-destructive and the ice remains in its mechanical and thermal equilibrium. The principle of electrical methods relies on the fact that the electrical properties of the solid-ice matrix contrasts those of the brine as pure ice is a poor conductor, while brine has a high electrical conductivity.

The least invasive method to determine the microphysical properties of sea ice using electrical methods is cross-borehole resistivity measurements [*Ingham et al.*, 2008; *Jones et al.*, 2010, 2011, and references therein], where a combination of resistivity measurements from four pairs of current and potential electrodes allows for the estimation of vertical resistivity, which is related to the brine-volume fraction in the ice.

An alternative is the method discussed here, which began with the measurements of *Shirtcliffe et al.* [1991], who developed an instrument to determine the liquid-brine fraction by measuring the electrical impedance be-

tween electrodes. The instrument has to be setup in open-water conditions. Since the development of *Shirtcliffe et al.* [1991]; *Shirtcliffe and Kerr* [1992], their instrument has undergone a number of modifications and improvements [*Shirtcliffe and Kerr*, 1992; *Notz et al.*, 2005; *Yamagishi and Langhorne*]. However, the attempt to use the instrument developed by *Notz* [2005, the so-called wire harp] failed to give reliable results during the experiment to study the Reduced Ice Cover of the Arctic Ocean [RECARO, 2007/08 *Wilkinson et al.*, 2009], which is why the electrical setup had to be revised and improved thereafter [*Fontes et al.*, 2009; *Fontes*, 2009].

In this chapter, I discuss limitations and error sources of the wire harp, and present results of preliminary tests that I obtained by using an intermediate version of a new instrument that still is under construction, the Harp3d [*Fontes et al.*, 2009; *Fontes*, 2009].

4.2 THEORETICAL BACKGROUND

Before discussing the limitations and possible error sources of the wire harp [*Notz*, 2005], I review the principles underlying the calculation of the liquid fraction of sea ice from impedance measurements between two thin metallic wires as obtained from the Harp3d.

The complex electrical impedance (or alternating-current (a.c.) resistance) specifies the ratio between the voltage and the current that was applied to and adjusted from a device. In our case, this device consists of two very thin bare metallic wires, arranged in a distance of 10 mm (see figure 4.1).

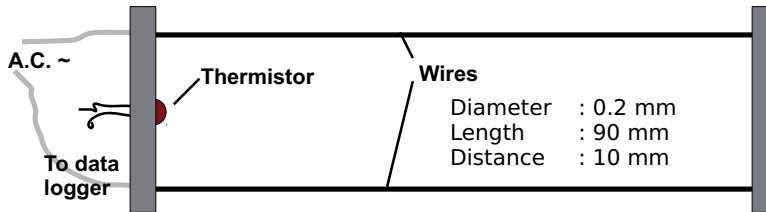


Figure 4.1: Sketch of two metallic wires arranged to measure the electrical impedance by applying an a.c. voltage.

After deploying the device into a sodium-chloride solution and applying an a.c. voltage, the impedance can be calculated as the ratio between the complex sinusoidal a.c. voltage $u(t)$ and current $i(t)$ as

$$Z = \frac{u(t)}{i(t)}. \quad (4.1)$$

In polar coordinates, the absolute value of the impedance $|Z|$ represents the impedance, i. e., the length of the vector in the coordinate system (see figure 4.2). The angle φ gives the phase shift between voltage and current, i. e., the rotation relative to the real axis.

$$Z = |Z| \cdot e^{i\varphi} = |Z| \cdot (\cos \varphi + i \sin \varphi) \quad (4.2)$$

In cartesian coordinates, the real part $R = \text{Re}(Z) = Z \cos \varphi$ represents the resistance R that converts the transferred effective power, and the imaginary part $X_C = \text{Im}Z = Z \sin \varphi$ represents the reactance X_C , which stores energy and loads it back to the generator. The geometric sum of resistance R and reactance X_C gives the impedance $|Z|$.

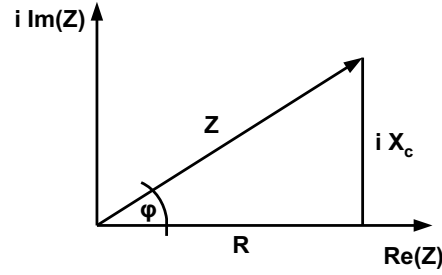


Figure 4.2: Sketch of impedance in the complex plane. Real part represents resistance, which is dependent on medium between the wires. Imaginary part represents capacitive part of impedance, which is dependent on the medium in immediate vicinity of the wires.

$$|Z| = Z = \sqrt{R^2 + X_C^2} \quad (4.3)$$

Here, R is the resistance between the thin wires, which is dependent on the medium between them, i. e., the sodium-chloride solution. If we cool the solution down to its freezing point, pure ice will start to separate from it. Hence, the fraction of the electrically isolating freshwater ice between the wires increases, which leads to an increase of the resistive part of the impedance proportional to the fraction of the isolating ice.

The reactance is calculated as $X_C = -1/\omega C_d$, where ω is the angular frequency of the applied voltage, and C_d is the so-called double-layer capacitance (hereafter dlc). The concept of the dlc relies on the fact that the charged surface of a wire will attract and reject ions provided by the electrolytic solution. An ion cloud in the immediate vicinity of the wire surface consisting of two charged and parallel layers will evolve. One of these layers (the one with ions of opposite charge) is closer to the surface of the wire than the diffuse layer (see figure 4.3). This separation of charge, accompanied by a very thin physical separation of the two layers in the order of nanometers is called the dlc. The dlc works like a conventional capacitor without a dielectric, since the layers are from the same solution [see e. g. *Rieger, 1993; Hunter, 1987*]. As the freshwater-ice matrix grows, the dlc gets smaller because of the reduction in available ions close to the wire (see figure 4.3). This leads to an increase in the reactance.

Hence, measuring the impedance delivers information about both the evolution of the fraction of pure ice between the wires, and the evolution of available ions in the immediate vicinity of the wires.

As the solid-ice matrix grows at the expense of the liquid brine, the salinity of the entrapped brine increases to maintain phase equilibrium. The opposite happens when the solid-ice matrix melts. Thus, any increase or decrease in the solid-volume fraction of the ice caused by local-temperature changes is accompanied by a change of the concentration (i. e., salinity) and hence conductivity of the entrapped interstitial liquid brine. To determine this conductivity, information about the local brine temperature and brine salinity is needed, which is why we arranged a thermistor¹ close to the wires to measure the local temperature (see figure 4.1). This temperature can then be used to calculate the brine salinity by applying the so-called liquidus temperature, which is the temperature at which a solid phase of a solution

¹ 2.2K3A1 Series 1 Thermistor, calibrated to an accuracy of 0.01 °C

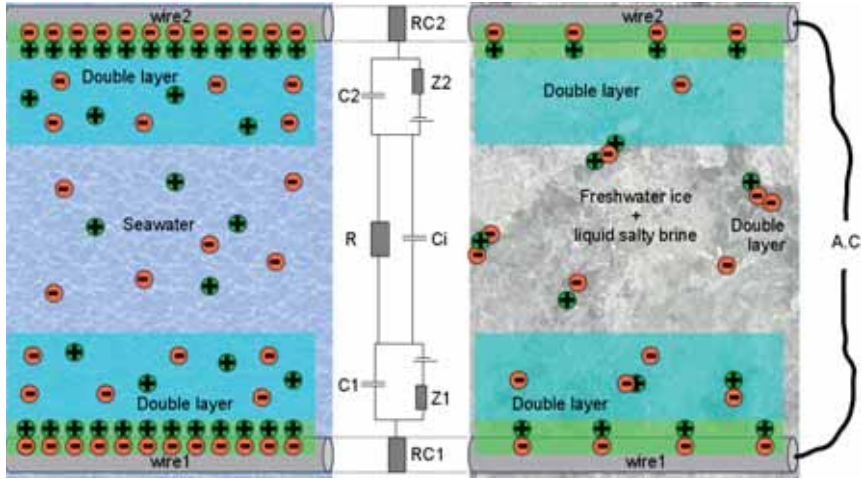


Figure 4.3: Equivalent circuit of one wire pair seen from above. Left panel shows conditions in solution, right panel shows conditions when sea ice has formed. See text for details.

occurs. A cubic fit to the experimental data in *Weast* [1971] gives the liquidus relationship for sodium-chloride solutions as

$$T = (-5.33 \cdot 10^{-7} \cdot S^3) - (9.37 \cdot 10^{-6} \cdot S^2) - 0.0592 \cdot S, \quad (4.4)$$

and inverting equation 4.4 gives the concentration of the brine as

$$S = -0.00361 \cdot T^3 - 0.388 \cdot T^2 - 17.6 \cdot T. \quad (4.5)$$

The conductivity of the brine can then be estimated from both the measured reactance and resistance as a function of local temperature and salinity $\gamma(T, S_{br})$. Hence, the setup as shown in figures 4.1 and 4.3 can be seen as a conductivity cell. To accurately determine the temperature and salinity dependency of the conductivity cell for the specified geometrical configuration of the Harp3d, a calibration of both the reactance and resistance at appropriate temperature and salinity ranges is essential. Unfortunately, a variety of problems with the mechanical setup of the electronics prohibited a careful calibration. For example, circuit boards were housed in a container below the surface to minimize disturbances at the water surface during freezing. The problem was that the connectors, which were sold as water tight, definitely were *not* water tight, which led to flooding of the circuit boards with saltwater. This was but one example of the problems we arrived at while testing the Harp3d. However, the calibration is not important for the following discussion of the theoretical and mechanical basics of the instrument and is left for later studies.

Once the calibration of the conductivity will have been performed, taking the ratio between the conductivity γ_0 and the impedance Z_0 of the solution before ice formation started, and the conductivity $\gamma(T, S_{br})$ of the interstitial brine and the impedance Z at a later point after the onset of ice formation, we can calculate the liquid-volume fraction similar to the method of *Shirtcliffe et al.* [1991] as

$$(1 - \Phi_S) = \frac{\gamma_0 Z_0(R, X_C)}{\gamma(T, S_{br}) Z(R, X_C)}, \quad (4.6)$$

where Φ_S is the solid-volume fraction, and resistive and reactive parts of the impedance have to be accounted fraction weighted as obtained by the calibration. Since bulk salinity, brine salinity, and the liquid fraction are connected by

$$(1 - \Phi_S) = \frac{S_{bu}}{S_{br}}, \quad (4.7)$$

we can calculate the bulk salinity of sea ice as $S_{bu} = S_{br}(1 - \Phi_S)$. Hence, arranging a number of such wire pairs at an adequate distance in the vertical and measuring the impedance will provide information of the evolution of the bulk salinity of sea ice at desired depths.

In a nutshell, the novel development of the Harp3d [Fontes *et al.*, 2009; Fontes, 2009] is capable to measure the resistive and capacitive part of the impedance independently, which will give new insights into the individual evolution of the solid and liquid phases of sea ice.

4.3 FROM WIRE HARP TOWARDS HARP3D

In contrast to the capability of the Harp3d in measuring the resistive and capacitive part of the impedance independently, the wire harp as developed by Notz [2005], was only capable to measure the absolute value of the impedance $|Z|$.

From the theoretical considerations given in the previous section, I would expect a significant amount of the measured impedance to be influenced by both the resistive and reactive part. However, Notz [2005] and Notz *et al.* [2005] assumed the impedance to be purely capacitive (i. e., they only considered reactance as being important), because they found during sensitivity studies that the *absolute* value of the impedance did not change when they varied the distance between the wires. Hence, they neglected the impact of the resistive part of the impedance in all interpretations of their data.

To find the flaw, I did sensitivity studies of the electrical setup of Notz [2005] and found that the crux is the amplifier and filter box they use (see Notz [2005, pg. 127]). Dependent on the resistance that is supposed to be measured, the applied voltage changes. To quantify this, I used a multimeter and measured the change of the output voltage dependent on different fixed resistances for an applied voltage of 1 V (which had to be set at the amplifier and filter box) and a frequency of 2 kHz. Both values were denoted by Notz [2005]; Notz *et al.* [2005] as the standard configuration. The result is shown in figure 4.4a and indicates that during both their experiments and sensitivity studies, where the latter were supposed to find the dependency of the absolute value of the impedance and the distance between the wires, the amplifier and filter box artificially increased the applied voltage with increasing resistance.

Thus, the authors measured an impedance that was lower than it would have been with a constant applied voltage, because in fact the resistance and hence the absolute value of the impedance *is* changing with distance. Results of preliminary tests for the development of the electrical setup of the Harp3d I did with an oscilloscope and a multimeter at various frequencies are exemplarily shown for 1, 1.5 and 2 kHz (see figure 4.4b). The results indicate that the influence of the distance between the wires on the impedance is rather small for distances below 5 mm, that it increases for

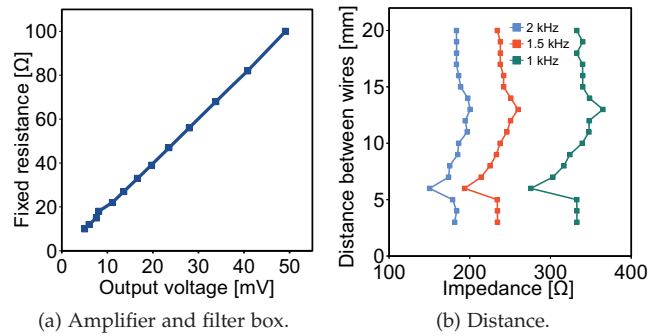


Figure 4.4: (a) Influence of amplifier and filter box of wire harp on output voltage. (b) Impedance as a function of distance between wires.

distances between 6 and 13 mm, and for distances between 14 and 20 mm it seems to decrease. The two jumps in the curve progression show even more clearly that a very careful calibration of the individual setup has to be done prior to a derivation of dependencies of the conductivity cell and finally the bulk salinity.

Moreover, we find the value of the applied voltage to be far below the author's intended value of 1 V. In a way, it was fortuitous that the box reduced the intended applied voltage, since the Gouy-Chapman theory, which describes the concept of the dlc, suggests that the applied voltage needs to be below 25 mV for the Debye-Hückel approximation, which describes electrostatic interactions between ions in electrolytes, to hold [Hunter, 1987; Lyklema, 1991]. This maximum of 25 mV for the applied voltage was one of the prerequisites for the Harp3d. The reason for the low voltage is that in the case it is too high, the ions in the solution will be accelerated to a velocity that allows them to leave the ion atmosphere (Wien effect). For the frequency with which the voltage is applied to the wires it is important that the relaxation time that is necessary for the ion atmosphere to form is 10^{-7} seconds, which implies that the frequency of the applied voltage has to be lower than 10 MHz. Otherwise the movement of the ions will be faster than the formation of an ion atmosphere and we would measure a too high conductivity (Debye-Falkenhagen effect). Preliminary tests to find an appropriate frequency did not show significant changes for several applied frequencies and we finally decided for 2 kHz to make the measurements comparable to those obtained by Notz *et al.* [2005].

Another modification for the Harp3d is the material of the wires. All of the previous versions of the instrument contained platinum wires. However, this material is very expensive, highly sensitive to any mechanical perturbations, and difficult to solder. This is why I performed tests with several materials, including tungsten, which gave very nice results during its first setup, but the wires corroded almost immediately once the device was exposed to air. Finally, I found a material that was cheap and insensitive to mechanical perturbations, yet still difficult to solder—stainless steel. The difficulties during soiling can be overcome by using the hardness of the material to form small loops, in which the thin cables can be placed to connect the device with the logger. A comparison between the different impedances for the two materials as obtained with an intermediate version of the Harp3d will be given in the next section.

4.4 INTERMEDIATE RESULTS OF HARP3D

Here, I describe results of a first experiment to test the general electrical and mechanical setup of the Harp3d during freezing and melting cycles, and to investigate the differences between platinum and stainless-steel wires. Therefore, I constructed a simple device that basically consists of two plates made from plastic with both platinum and stainless-steel wire pairs arranged at a distance of both 0.5 cm and 1 cm in between them, respectively (see figure 4.5). Two stainless-steel screws with a diameter of 0.8 cm held the plates in a distance of 9 cm from each other and the wires were thus spanned to a length of 9 cm. A thermistor² was arranged in the center of the device to measure the temperature at the wire level. This device was arranged approximately 1.5 cm below the surface of an insulated tank that was filled up to a water level of 1 m with a sodium-chloride solution mixed to a salinity of 31.4 g/kg. This implies a freezing temperature of the solution of $-1.88\text{ }^{\circ}\text{C}$.

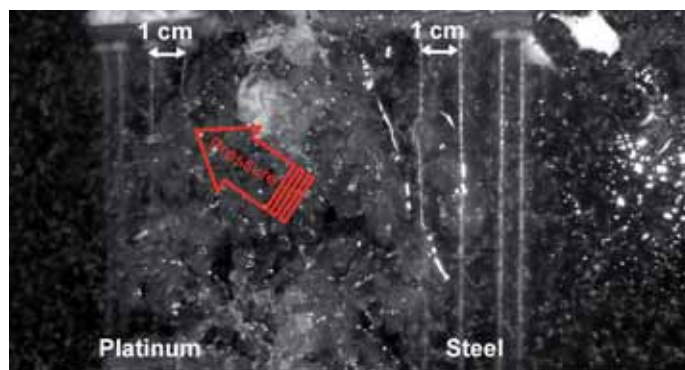


Figure 4.5: Top view of test device to measure the impedance between wires frozen into the ice. Data presented here stem from the two inner wire pairs that were arranged in a distance of 1 cm, where one was a platinum-wire pair, and the other was a stainless-steel wire pair. Note mechanical influence of the ice on wire pair to the left.

The tank has inside dimensions of $1.95 \times 0.67\text{ m}^2$ and a height of 1.2 m, and is housed in a cold room of $3 \times 1.25\text{ m}^2$ and a height of 2.25 m. The temperature of the cold room can be controlled down to $-25\text{ }^{\circ}\text{C}$. De-frost cycles of the cooling machine induce fluctuations of the preset ambient temperature. An air-temperature sensor³ was arranged in a distance of 30 cm from the water/ice surface. The sampling interval was set to 30 s. Temperature and impedance of the test device were measured with Harp3d at a temporal resolution of 7 s.

To observe how the impedance in water changes during cooling, I started the experiment when the water temperature was approximately $5\text{ }^{\circ}\text{C}$ above the freezing point of the solution, i. e., $+3\text{ }^{\circ}\text{C}$. The ambient air temperature was set to $-25\text{ }^{\circ}\text{C}$ for a duration of 22 hours and to $-5\text{ }^{\circ}\text{C}$ for the next 7 hours. Thereafter, I switched off the freezing machine and opened the door of the cold room to induce melting. In the following, I focus on the results obtained for the wire pairs with a distance of 1 cm. Results are shown in figure 4.6.

² 2.2K3A1 Series 1 Thermistor, calibrated to an accuracy of $0.01\text{ }^{\circ}\text{C}$

³ Campbell 43347 RTD temperature probe with Campbell 43502 aspirated radiation shield

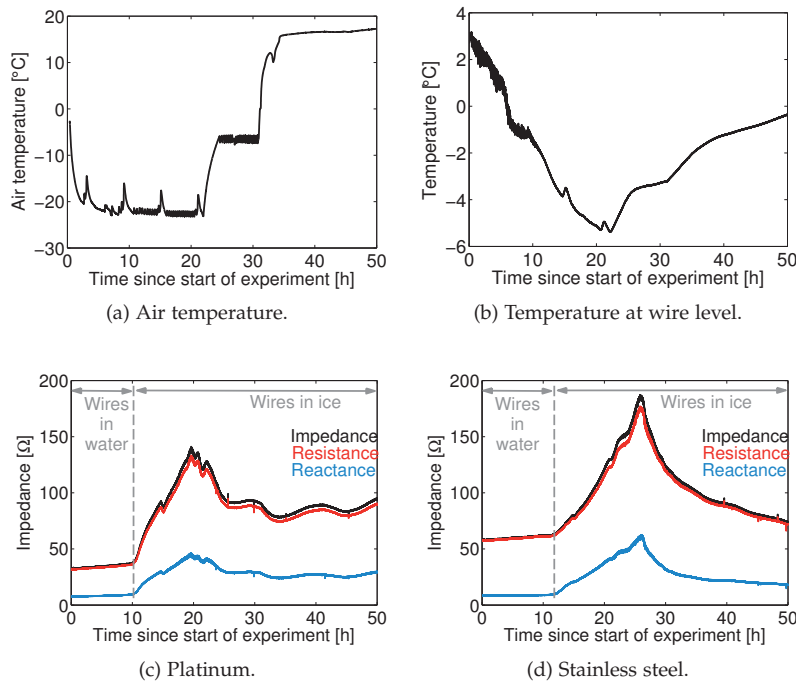


Figure 4.6: Temperature at (a) 30 cm above surface and (b) at wire level 1.5 cm below the surface. Impedance between (c) platinum-wire pair and (d) stainless-steel wire pair. See text for details.

Most striking is that for all periods the impedance is almost purely resistive for both platinum and stainless-steel wire pairs (see figure 4.6c and d). This substantiates that the assumption made by *Notz* [2005] that the impedance is purely capacitive and the resistive part of the impedance can be neglected is wrong.

Principally, the impedance-curve progression for both materials is similar. As long as no ice-formation occurred, impedance slightly increased with decreasing water temperature, which can be explained by the decreasing conductivity due to the decreasing mobility of the ions, as the viscosity of the water increases with decreasing temperature. After approximately 11 hours, the fluctuations in temperature measured by the thermistor at wire level considerably decreased (see figure 4.6b), which indicates ice formation at 1.5 cm below the surface. The temperature was -1.88 °C at that time, i. e., at the salinity-determined freezing temperature. Almost simultaneously⁴, the slope of the impedance considerably increases, which indicates ice formation, as the increasing fraction of pure ice and therewith resistance between the wires increases. Although not as steep as the resistance, the reactance increases as well. This indicates a decreasing fraction of ions in the immediate vicinity of the wires as the pure-ice fraction increases. Although salinity and conductivity of the brine increase due to the growth of pure ice at the expense of the brine water, the dlc gets weaker (see figure 4.3), because of fewer ions directly at the wires, (Recall that reactance is calculated as $X_C = -1/\omega C_d$. Hence, reactance increases with decreasing availability of

⁴ That the ice did not form *precisely* at the same time at both wire pairs was caused by different times of freeze-up at the surface above the respective wire pair.

ions and weaker dlc.).

After 19 hours, the curve progression of both materials began to differ considerably. The resistance and reactance of the platinum wires were at maximum at that time and then began to first gradually decrease, and after the air temperature was set to -5°C after 22 hours, both parts continuously decreased until hour 25. Thereafter, resistance and reactance alternately increased and decreased until the end of the experiment. In contrast, the resistance and reactance of the stainless-steel wires decreased continuously until the end of the experiment, after they had reached their respective maximum at hour 26.

The explanation for this quite different behavior I see in the different types of ice that grew between the respective wire pairs (see figure 4.5). The ice that had formed between the platinum wires was rough and uneven and differed strongly from the very smooth ice at the surface elsewhere in the tank. Moreover, one of the platinum wires was deformed by the pressure that was caused by the ice bubble in the center of the device (indicated by red arrow in figure 4.5). In contrast, the ice between the stainless-steel wires was very smooth, comparable to the smoothness of the ice surface elsewhere. This shows that although the device was arranged *below* the surface, and although the environmental conditions were calm, the instrument disturbed the natural growth conditions for the ice and thus caused the formation of an ice structure that was not representative for the environmental conditions.

Hence, the ice changed the setup for the platinum wires and I find it difficult to compare the curve progressions during the melting period. However, the steel resistance and reactance both show a continuous decrease. The resistance decrease indicates a decrease in the solid fraction and hence the melting of the solid-ice matrix. The reactance decrease indicates that the availability of ions in the immediate vicinity of the wires increases for the same reason as it was decreasing during freezing—the phase change of the solid ice comes along with an increasing fraction brine and therewith available ions in the immediate vicinity of the wires. Hence, the dlc gets stronger, and reactance decreases.

I find an additional contrast to the statement by *Notz* [2005] that the individual wire pairs of the instrument showed always the same impedance value for comparable setups. The results of the impedance measurements of the other wire pairs in a distance of 0.5 cm in the experiment described above (not shown) showed similar shapes in general though, but I found the values to strongly differ from wire pair to wire pair during several experiments, even from the same material, at the same distance, and under the same environmental conditions. This can only be explained by a very high sensitivity to the wire surface, which changes dependent on its history of both being deployed in saltwater and experiencing mechanical influence of the growing and melting of different structures of ice. Moreover, I suppose the tension of the wires to be important, too. The wires definitely need to be tighten in a similar way. Any change of the geometry of the conductivity cell will influence the measured impedance. This indicates that a calibration of the instrument should be done prior to each experiment for each individual wire pair, and that a regular cleaning of the wires is essential to obtain reliable results.

4.5 SUMMARY AND CONCLUSIONS

In this chapter, I discussed the reliability of assumptions made for past wire-harp measurements [Notz, 2005; Notz *et al.*, 2005], and indicated error sources of the wire harp. I have shown results of an intermediate version of the Harp3d [Fontes, 2009; Fontes *et al.*, 2009], which, as the wire harp, was developed based on the idea of the first development of such an instrument by *Shirtcliffe et al.* [1991]. The Harp3d is the first of such an instrument that is capable to measure the individual parts of the impedance, resistance and reactance, independently. This enables us to make statements about the fraction of pure ice in between the wires, and about the availability of ions in the immediate vicinity of the wires.

I have shown that, contrary to the assumptions of Notz [2005], the impedance is almost purely resistive. This implies that the impact of the geometrical distribution of the ice-brine mixture between the wires (resistance), and in the immediate vicinity of the wires (reactance), definitely need to be taken into account for a reliable calculation of the bulk salinity of sea ice when using this type of instrument; this was noted also by *Chiareli and Worster* [1992].

However, I have found difficulties comparable to those already mentioned by *Shirtcliffe et al.* [1991] and *Shirtcliffe and Kerr* [1992], in that the data are too difficult to interpret, and that the presence of the wires in the supercooled liquid just ahead of a growing crystal might act as a nucleation site and change the properties of the forming ice. Both problems occurred during my experiments, where the impedance values considerably changed for the same experimental setups, and where the presence of the instrument influenced the properties of the forming ice even under very calm conditions in the lab (see figure 4.5). Thus, I doubt the applicability of the instrument under rough environmental conditions in the field, except for short, controlled experiments, where holes are cut into the already existing sea ice. Even if there will be a solution for the permanently changing impedance values of individual wire pairs under the same environmental conditions, and even if we find a way to manage the instrument's perturbation influence on the properties of the forming ice, its field applicability is limited since any pressure caused by the moving of ice due to tides, winds, or currents very likely will deform the wires and thereby change the individual conductivity-cell setup and calibration.

Or—the instrument will be completely destroyed by ice pressure.

However, once the development of the electrical and mechanical setup allows for a careful calibration, impedance values for individual wire pairs might be more stable, and the influence of the instrument on the properties of the forming ice might be minimized. Then the instrument can be used during lab studies to examine the salinity evolution of sea ice under different experimental setups, and during field studies if steady supervision is guaranteed, to validate measurements of the microphysical properties of sea ice as obtained from cross-borehole resistivity studies [Ingham *et al.*, 2008; Jones *et al.*, 2010, 2011] and ice cores.

Part V

A SEA-ICE LIFE ON A WARM OCEAN

Dort nun wo das Wasser mit der Luft in Berührung tritt, wird es im Winter abgekühlt, es nähert sich seinem Dichtigkeitsmaximum, wird schwerer und sinkt, es treten wärmere Schichten von unten an seine Stelle, die wiederum eine Abkühlung erleiden, und wiederum anderen Platz machen. Aehnlich wie bei den Landseen sollte also eigentlich die Eisbildung erst dann stattfinden können, wann die ganze Wassermasse bis zum Gefrierpunkte erkaltet ist und ihre Wärme an die Luft abgegeben hat.

Allein ebenso wie bei directem Contacte mit der Luft die Abkühlung und damit die Eisbildung zu rasch vor sich geht, als dass bei letzterer das ganze Salz ausgeschieden werden könnte, ebenso findet die Vermischung des Wassers in Folge der Zunahme an Schwere nicht mit genügender Geschwindigkeit statt, um die Krystallisation der obersten Schichten verhindern zu können ehe sie sinken. Es bildet sich schon Eis, bevor die untersten, wärmeren an ihre Stelle getreten sind. Nimmt der Salzgehalt des Meerwassers mit der Tiefe zu, so würde dies erschwerend für die Vermischung wirken. Allein hierüber sind wir vor der Hand durchaus noch nicht im Klaren.

— Karl Weyprecht, 1879

HEAT EXCHANGE THROUGH GROWING AND MELTING FIRST-YEAR SEA ICE

ABSTRACT

I discuss the energy exchange between ocean and atmosphere during freeze-up, growth, and melt of first-year sea ice, based on a variety of measurements we carried out above and below the ocean surface during a winter-long field campaign in a small Greenlandic bay from November 2009 until May 2010.

Even though the seawater temperature at a depth of 0.5 m below the water/ice surface never reached the freezing point, sea ice eventually formed and grew up to an average final thickness of 0.33 m. To investigate how sea-ice formation on seawater that is well above its freezing point is possible, I carried out a lab experiment, which suggests low turbulence at the water surface and a sufficient temperature difference between ocean and atmosphere to be prerequisites for the formation to occur.

Maximum oceanic heat loss of 121 W/m^2 occurred during the initial formation of a continuous sea-ice cover. Once the ice had attained its equilibrium thickness, oceanic heat loss was about 63 W/m^2 . Estimated heat-transfer coefficients during the same periods were 230 and $130 \text{ W/m}^2\text{K}$, respectively.

I compare estimated and measured ice thicknesses. The results agree well until accumulation of heat at the ice surface induced melting of the ice interior.

5.1 INTRODUCTION

Sea ice has a significant influence on the thermodynamics of the ocean surface. During winter, sea ice insulates the ocean from the cold atmosphere; and during summer, sea ice reduces the penetration of solar energy into the ocean by reflecting the incoming shortwave radiation [see e. g. *Perovich et al.*, 1998]. Arctic sea ice has been undergoing significant changes concerning the reduction in coverage and thickness of multi-year sea-ice, accompanied by an overall increase in the areal fraction of first-year sea ice. [*McPhee et al.*, 1998; *Johannessen et al.*, 1999; *Rothrock et al.*, 1999; *Tucker et al.*, 2001; *Comiso*, 2002; *Maslanik et al.*, 2011]. Since measurements above, within, and below sea ice are rare and in the majority of cases were carried out on perennial sea ice, measurements above and below the practically inaccessible first-year sea ice are essential to understand the ocean-atmosphere-heat exchange through first-year sea ice in a future climate. In this chapter, I discuss changes of atmospheric and oceanic physical properties caused by growing and melting first-year sea ice that formed from seawater with temperatures well above freezing.

The freezing and melting of sea ice balance the discrepancy between the heat from the ocean, the heat conducted through the ice, and the heat from the atmosphere. The surface heat budget is the sum of the radiative fluxes of solar and longwave radiation, the turbulent fluxes of sensible and latent heat, and the heat conduction through the ice. The radiative fluxes dominate the heat balance [*Persson et al.*], and how much of the incoming solar radiation is absorbed by the ice is greatly affected by the albedo of the ice. The incoming longwave radiation is influenced by the cloud cover, and the outgoing longwave radiation is a function of the surface temperature. The wind speed, and the temperature and humidity differences between air and surface determine the turbulent fluxes, and the heat conduction of sea ice is set by air temperature, ice thickness, and the snow cover.

The ocean-heat flux is set by the conditions in the ice-ocean-boundary layer and changes on seasonal and spatial scales, which makes it one of the key difficulties in modeling the heat and mass balance of sea ice [*Maykut and Untersteiner*, 1971; *Maykut*, 1978; *Wettlaufer*, 1991; *Ebert et al.*, 1995; *McPhee*, 2008; *McPhee et al.*, 2008]. It was shown that models with a more reasonable seasonal cycle relative to observations project a faster future decline of september sea-ice extent [*Wang et al.*, 2009]. Hence, with the ongoing retreat of perennial sea ice in the Arctic, the seasonality of sea ice and the accompanied heat-flux changes at both the ice-atmosphere and the ice-ocean interface need to be included in climate models to more realistically predict the future sea-ice cover.

Here, I investigate the role of the evolution of first-year sea ice for the physical properties of its adjacent layers atmosphere and ocean, and on the heat flux at the ocean surface during both abrupt and gradual transitions from an ice-free to an ice-covered ocean. The study is based on a variety of data, which we obtained during a winterlong field campaign at the northwestern coast of Greenland during the unusually warm winter of 2009/2010 [*Jung et al.*, 2010]. Additionally, I did a lab experiment to understand under which conditions sea-ice formation can occur in seawater with a temperature above freezing.

The chapter is organized as follows: After a general description of the field

campaign in section 5.2, I discuss if it possible to estimate the state of the sea-ice cover from our measurements of relative humidity, and how the evolution of sea ice influenced the hydrography. In section 5.3, I present results of a lab study that I carried out to understand how sea ice could form on water that was above its salinity-determined freezing temperature. In section 5.4, I discuss how the heat exchange between ocean and atmosphere was influenced by the formation, growth, and melt of first-year sea ice. Section 5.5 gives a summary and presents conclusions of this chapter.

5.2 FIELD CAMPAIGN

From November 2009 until May 2010, we carried out a winterlong field experiment in a small Greenlandic bay (72.79° N, 56.06° W) to study the atmosphere-ice-ocean interaction during the formation, growth, and melt of first-year sea ice. The bay is 5 km beeline to the airport of the settlement Upernavik, which itself is located on an island within the fjord landscape of Western Greenland (see figure 5.1). The bay covers an area of $120 \times 100 \text{ m}^2$ and has an average depth of 8 m. Because oceanic currents were almost absent and surrounding mountains protected the bay from the wind, the bay turned out to be a perfect site to study the evolution of young sea ice under calm conditions.

We were on site three times during the experiment—in November 2009 (to set up the instruments), in March 2010 (to control the status of the instruments and to carry out additional experiments on the evolution of frost flowers (see chapter ff)), and in May 2010 (to recover the instruments). A sailing ship overwintering in the bay provided a basis for us and our scientific equipment during the whole time of the field campaign.

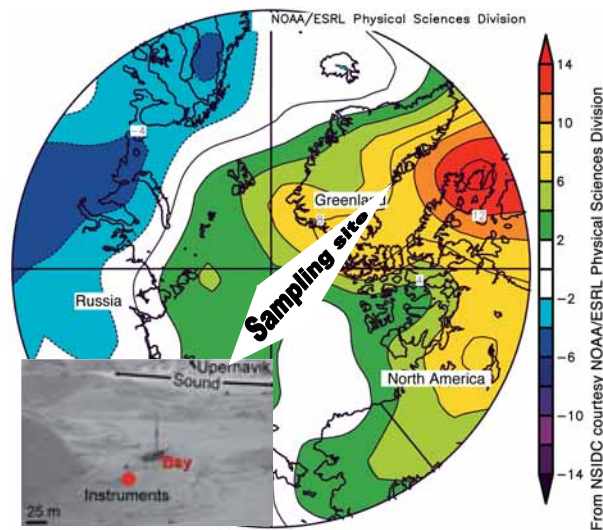


Figure 5.1: Map of air-temperature anomalies for February 2010.^a

^a Provided by the National Snow and Ice Data Center courtesy NOAA/ESRL Physical Sciences Division; source: <http://nsidc.org/arcticseaicenews/2010/030310.html>

5.2.1 Setup and methods

We chose the sampling site in the middle of the bay, to be as far as possible away from the surrounding land and from the sailing ship. In November 2009 we arranged air temperature¹, wind², and humidity³ sensors at a height of 2 m above the surface. A radiometer⁴ was arranged at a height of 50 cm above the surface. To measure the salinity and temperature evolution below the growing and melting ice, a conductivity-temperature sensor (CT)⁵ was deployed 50 cm below the water surface. The sampling interval of all instruments was set to 30 s.

The radiometer consists of five sensors: a pair of pyranometers with one facing upward, the other facing downward to measure both the incoming and surface-reflected shortwave radiation; and a pair of pyrgeometers in a similar configuration to measure both the incoming and outgoing longwave radiation. The fifth sensor is a temperature sensor measuring the internal temperature of the radiometer. It can be used to get more precise readings of the infrared radiation. Because pin space on the data logger was limited, we decided to use the air temperature instead, which might have caused small errors during the calculation of the longwave radiation. Other error sources are the instrument leveling and the cleanliness of the domes; if the domes are covered by hoar frost, rain or snow, readings are reduced. However, the overwinterers tried to check both the leveling and the cleanliness of the domes every two days, which is why I expect the errors to be within $\pm 2 \text{ W/m}^2$.

The wind sensor stopped working right at the beginning of the campaign, when wind speed was so high that the sensors broke. However, a comparison of the wind data measured by our sensors and the data measured at the Upernavik airport showed only small deviations with a maximum of $\pm 0.5 \text{ m/s}$, and I used daily wind data measured at Upernavik airport for this study.

From the end of March until the end of May, we additionally deployed a thermistor rod within the already existing sea ice. The rod was made of teflon, had a diameter of 4.5 cm, and contained twenty nine thermistors⁶ at a vertical resolution of 3 cm. The sampling interval was set to 10 min.

The overwintering crew provided information about the presence or absence of sea ice in the bay. From the end of March until the beginning of May one of the overwinterers occasionally took ice-core samples (see chapter sr). Bulk salinity and temperature along these cores were determined using standard methods [see *Eicken et al.*, 2009].

5.2.2 Observed ice and weather conditions

Influenced by an extreme negative phase of the Arctic Oscillation during the winter 2009/2010 [*Jung et al.*, 2010], which contributed to unusually high temperatures over Western Greenland (see figure 5.1), the freeze-up was extremely late, and—except for some ice floes with a thickness of approxi-

1 Campbell 43347 RTD temperature probe with Campbell 43502 aspirated radiation shield

2 Campbell A100R for velocity and Campbell W200P-1 for direction

3 rotronic hygrometer MP 100 A with RS 12 T radiation shield

4 Kipp & Zonen CNR4

5 SeaBird Electronics, SBE37

6 2.2K3A1 Series 1 Thermistor, calibrated to an accuracy of 0.05 °C

mately 20 cm that were floating in the bay in November and December—a continuous sea-ice cover did not form before January 2010, when air temperature had decreased from +4 °C on 1 January to −24 °C on 10 January (see figure 5.2a). A thin sea-ice cover formed on that day and grew up to a thickness of about 20 cm on 23 January. On 29 January, air temperature had increased to 0 °C. Together with winds of maximum velocities of 13 m/s, the ice became wet and porous and was breaking into small ice floes. From 11 February until 18 February air temperature decreased below −10 °C, a thin ice cover formed, which again was hindered to cover the whole bay by the upcoming air-temperature increase and an accompanied storm with wind velocities of up to 12 m/s on 21 February. Air temperature stayed below −10 °C from 23 February until 26 March 2010. During this period of one month, a continuous sea-ice cover formed both in the bay and in the sound between the bay and Upernavik. To reach the bay on 12 March, we were passing the sound with snow mobiles on 10 cm thin sea ice. However, the ice in the bay showed an average thickness of 30–35 cm. While the sound was already ice free when we were on site to recover some of the instruments in May, the ice thickness in the bay was then still 30 cm. On the day of our arrival on 9 May, the ice-surface structure showed a continuous snow cover as in March. However, the ice bottom was covered with algae-filled holes all over and the algae served as food for crustaceae. When we left the site three days later on 12 May, the ice-surface structure had changed from a continuous snow cover to a snow skeleton filled with meltwater. The ice had completely melted around 20 May 2010.

5.2.3 Estimation of sea-ice state from humidity

Here, I investigate if it is possible to use our measurements of relative humidity above the growing and melting ice as a diagnostical tool to determine the times of sea-ice formation and sea-ice melt.

Since the relative humidity is a measure of the rate of water evaporation as it takes into account the saturated vapor pressure, I expected significant changes in relative humidity during the formation and melting of the ice. However, the relative humidity during the times where we know about the occurrence of sea-ice formation and melt did not differ significantly compared to values obtained with sea ice present in March, for example.

This changes if we convert the measured relative humidity with respect to *water* saturation, to the relative humidity with respect to *ice* saturation. Measurements of relative humidity obtained during the yearlong Surface Heat Budget of the Arctic Ocean experiment (SHEBA) and during additional observations in the Antarctic that lasted for several months have shown that the relative humidity with respect to *ice* over sea ice is always near ice saturation; sometimes it is even supersaturated [Andreas *et al.*, 2002]. The authors argued that the high relative humidity with respect to ice is a consequence of the large amount of water vapor given up by leads and polynyas, and that supersaturation becomes more likely with an increasing fraction of leads and decreasing ice-surface temperature. Modeling studies let them conclude that the transfer of water droplets to the ice surface is not rapid enough to entirely relieve the supersaturation with respect to ice.

However, the measurements of Andreas *et al.* [2002, and references therein] were carried out over perennial sea ice. Our measurements can provide an insight into the different conditions concerning the relative humidity over

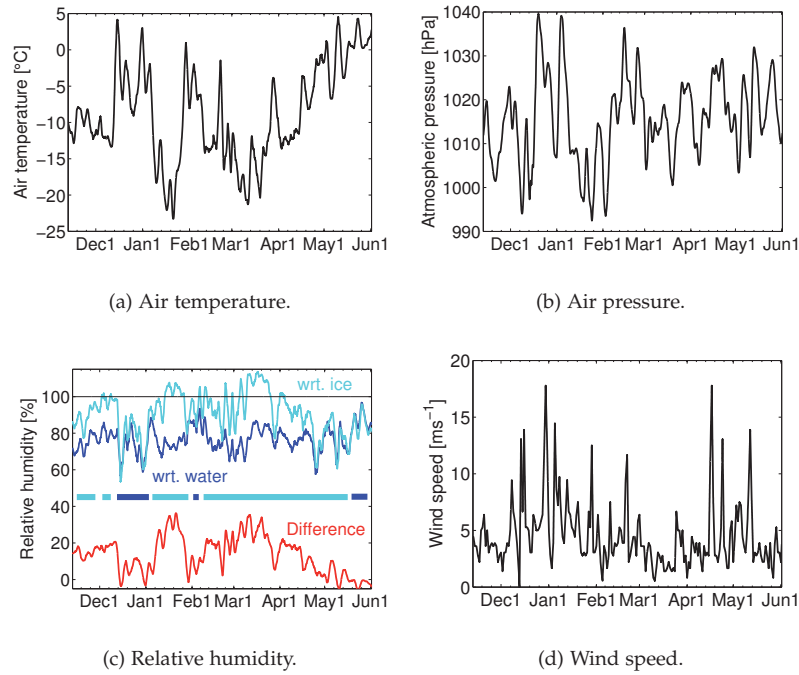


Figure 5.2: (a) Air temperature; (b) air pressure; (c) relative humidity with respect to (wrt.) water and with respect to ice, and the difference between the two; line in the middle indicates state of ice coverage in the bay as ice free (blue) and ice covered (turquoise); (d) wind speed during the field campaign. Data were averaged over a sliding window of one day.

growing and melting first-year sea ice, which will be the prevailing sea-ice type in the Arctic in the near future.

The measured relative humidity with respect to water saturation rh_w can be converted to the relative humidity with respect to ice saturation rh_i by

$$rh_i = rh_w \left[\frac{e_{sat,w}(T_a)}{e_{sat,i}(T_a)} \right], \quad (5.1)$$

where for $-40 \text{ }^\circ\text{C} \leq T_a \leq 0 \text{ }^\circ\text{C}$, [Buck, 1981]

$$e_{sat,w}(T_a) = (1.0007 + 3.46 \cdot 10^{-6} \cdot P) \cdot 6.1121 \exp\left(\frac{17.966 \cdot T_a}{247.15 + T_a}\right), \quad (5.2)$$

and for $-50 \text{ }^\circ\text{C} \leq T_a \leq 0 \text{ }^\circ\text{C}$

$$e_{sat,i}(T_a) = (1.0003 + 4.81 \cdot 10^{-6} \cdot P) \cdot 6.1115 \exp\left(\frac{22.452 \cdot T_a}{272.55 + T_a}\right). \quad (5.3)$$

The measured air temperature T_a is in $^\circ\text{C}$, and the barometric and saturation-vapor pressures over water and ice, P , $e_{sat,w}$ and $e_{sat,i}$ are in hPa, respectively. Relative humidity with respect to ice is shown together with the measured relative humidity with respect to water and the difference between the two in figure 5.2c. The state of the water/ice surface is indicated by the line in the middle of figure 5.2c, with a turquoise line when the bay was ice covered, and a blue line when the bay was ice free.

The relative humidity with respect to ice is increasing with a decreasing

fraction of open water, which was the case in January and in March, when ice was forming and growing in both the bay and the sound between the bay and the settlement Upernavik. Only during these times of high ice-formation rates, the relative humidity with respect to ice shows supersaturation. In November and the first half of December, when thicker ice floes were floating in the bay, the relative humidity with respect to ice was near saturation. The strong decrease in relative humidity with respect to ice close to 26 March can be explained by the strong air-temperature increase, which is very likely to have enhanced the melting of the thin ice in the sound close-by, which substantiates that an increasing fraction of open water decreases the relative humidity with respect to ice.

The difference between both humidities shows the dependence of the relative humidity with respect to ice on the state of the ice cover even more clearly. During ice-free states, the difference is close to zero, or it gets slightly negative. During times of high ice production, the difference is largest. When the ice in the bay started to melt at the beginning of May, the difference between both humidities gradually decreases until it reaches zero, when all ice had melted.

I conclude that supersaturation of relative humidity with respect to ice occurs during sea-ice growth, the relative humidity with respect to ice is near saturation when sea ice has reached an equilibrium state, and the relative humidities with respect to ice and water reach approximately the same value during sea-ice melt. This picture still holds in the light of the measurements carried out by *Andreas et al.* [2002, and references therein], as the opening of leads and polynyas within perennial sea ice increases the amount of water vapor in the atmospheric boundary layer. As they freeze-over again, which is comparable to our measurements in January and March, supersaturation of relative humidity with respect to ice can be found also over perennial sea ice.

Hence, the near-surface water vapor with respect to ice can be used to determine the times of sea-ice formation (supersaturation, $rh_i > 100\%$), to estimate when the ice reached an equilibrium state (saturation, $rh_i = 100\%$), and to determine when sea ice melts ($rh_i \approx rh_w$).

5.2.4 *Impact of sea ice on hydrography*

In this section, I describe how the formation, growth and melt of the ice influenced both the temperature and salinity evolution at a depth of 50 cm below the water/ice surface, and the exchange of heat between ocean and atmosphere.

Measured oceanic temperature and salinity below the growing and melting ice are shown in figure 5.3a and b, averaged over a sliding window of one day. From November until 10 February, oceanic temperature gradually decreased from -0.6 °C to -1.1 °C. During this period, the fluctuations of oceanic temperature were larger than during the following period from 10 February until approximately 10 May, which can be explained by strong winds in December and at the beginning of January (see figure 5.2d). After 10 May, oceanic temperature strongly increased from approximately -0.6 °C to $+1$ °C. This strong ocean-temperature increase was caused by sufficient warming of the surface and accompanied onset of ice melt.

Oceanic salinity increased from 33 g/kg in November to 33.7 g/kg on 20 Jan-

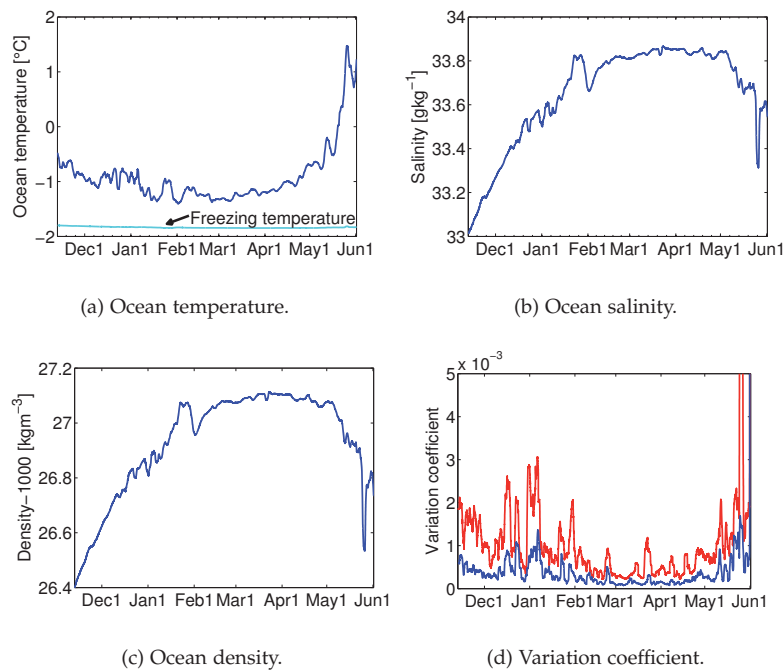


Figure 5.3: (a) Oceanic temperature; (b) salinity and (c) density 50 cm below growing and melting sea ice. (d) shows the variation coefficients for salinity and temperature. All data were averaged over a sliding window of one day

uary. Caused by strong storms, fluctuations in oceanic salinity were higher than average fluctuations from mid December until 10 January, when ice formation occurred. Salinity then further increased to 33.8 g/kg on 23 January, where it remained until 27 January. High air temperatures and strong winds led to melting of the thin ice accompanied by an enhanced freshwater input, causing salinity to strongly decrease to 33.6 g/kg on 10 February. From 10 to 22 February, salinity increased again to 33.8 g/kg, where it remained until 4 May. The period from 10 to 22 February most likely was the time when sea-ice formation occurred both in the bay and the sound. From 4 May until 1 June, salinity gradually decreased to a final measured value of 33.5 g/kg, with the exception of the strong decrease at the end of the field study, which was caused by the freshwater input due to the complete melt of the ice (see also chapter 3).

The change in fluctuations of oceanic salinity and temperature can be quantified by the variation coefficient (the standardization of the variance), which considerably decreases on 10 January (see figure 5.3d), when formation of a continuous sea-ice cover was first observed. This shows that already a very thin sea-ice cover is capable to strongly dampen the momentum exchange between atmosphere and ocean. However, after only 10 days high variations appear again, because the thin ice could not sustain the storm and high air temperatures at the end of February, which also illustrates the sensibility of such a thin ice cover. Once the ice had turned into a stable state, variations were significantly lower than average, and started to increase again around 23 April, when an ice-temperature changeover occurred, and flushing and bottom-ice melt were observed shortly thereafter (see chapter 3).

The salinity measurements show that once the ocean was covered by ice

with a thickness of approximately 20 cm, the salinity and hence density increase stagnates, which indicates decreasing ice formation at the bottom with increasing ice thickness (see period from mid February to beginning of May in figures 5.3b,c). The salinity-curve and density-curve progression substantiate the well-known assumption that it is mainly the initial sea-ice formation that is important for the formation of dense polar bottom waters [e. g. *Aagaard et al.*, 1981; *Carmack*, 2000; *Martinson and Steele*, 2001]. This implies that with an increasing fraction of first-year sea-ice formation in winter, more salt is expelled into the ocean, which is very likely to have an influence on the general deep-water formation in the Arctic.

To investigate how the formation, growth and melt of the ice in concert with the observed air-temperature and wind forcing modified the heat loss from the ocean, I performed a cross correlation between air and ocean temperature over a sliding window of 20 days. The correlation was estimated at the 99% confidence interval.

Results of the cross correlation between air and ocean temperature are shown in figure 5.4. Most obvious is the positive correlation during nearly the whole time of the field study (see figure 5.4b). Exceptions can be found from 15 to 25 January, and from 1 to 10 February, where correlations are negative and indicate that although air temperature increased or fluctuated between 0 and -5 °C (see figure 5.2a), respectively, ocean temperature did not adapt to these changes.

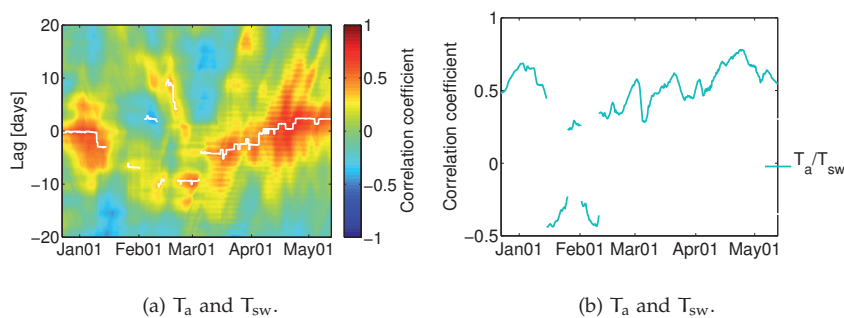


Figure 5.4: (a) Cross correlation over a sliding window of 20 days between air and ocean temperature. White line marks the lag of maximum correlation. (b) shows maximum correlation.

An answer as to why the correlation was negative can be found if we consider the lag, which helps us to determine who was leading—the atmosphere or the ocean (see figure 5.4a). From December until the beginning of January, when the bay was only partly covered by some ice floes, and strong winds and high air temperatures (see figure 5.2d and a) led to a well mixed oceanic layer, the exchange between ocean and air-temperature signals occurred almost immediately, which is indicated by the highest correlation appearing at lag zero. This changes on 10 January, when ice formation occurred and the lag of highest correlation turns to be -3 days, indicating both that the ocean was leading the atmosphere and that the transport of the temperature signal from ocean to atmosphere took about 3 days. Hence, as the ocean-temperature for example increased on 18 January, it took 3 days for the temperature signal to reach the atmosphere, where temperature indeed started to increase on 21 January. Physically, the negative correlation

from 15 to 25 January illustrates that ice formation caused both the isolation of the ocean from the atmosphere, and an enhanced convection within the upper-ocean mixed layer due to the accompanied sinking of dense brine, which led to a decrease in ocean temperature, although air temperature was increasing during this time.

The short period of positive correlation prior to the second period of negative correlation can be explained by the melting of the ice, which was caused by high air temperatures and a storm with wind velocities of about 13 m/s. The warm and fresh ice meltwater considerably increased the seawater temperature and decreased oceanic salinity (see figure 5.3a,b).

During the second period of negative correlation, the atmosphere was leading the ocean with a lag of approximately 2 days. Air temperature fluctuated between 0 and -5 °C with a negative trend, and ocean temperature was increasing. The negative correlation at that time comes due to the time the ocean (which was just warmed by the warm meltwater) needs to adapt to the strongly fluctuating and decreasing air temperature.

From 10 February until the end of the experiment in June, the correlation between air and ocean temperature was positive. The lag, however, was changing, indicating that prior to ice formation, the atmosphere was leading the ocean; and as soon as the surface was ice covered, the ocean took the lead. On average, the temperature was transported through 30-35 cm thick sea ice within approximately 3-4 days. As the sun was rising in March, the lag gradually decreased until it reached zero on 5 April, where it remained until atmosphere took the lead on 20 April. On that day, the correlation between air and ocean temperature was highest, and an ice-temperature changeover was observed that was accompanied by frequent ice-desalination events over a period of 10 days (see chapter 3). The overall increase in the correlation between air and ocean temperature, accompanied by the decreasing lag might give us an idea of the thermal conductivity of the ice, which should decrease as well with increasing temperatures. An investigation of this question will be left for later studies.

However, all processes described above occurred even though the seawater temperature at a depth of 50 cm below the surface never reached the freezing point (see figure 5.2a). Since it is generally agreed that sea-ice formation can only happen once the oceanic-mixed layer is cooled down to its salinity-determined freezing temperature [see e.g. Carmack, 2000; Aagaard *et al.*, 1981], I carried out a lab experiment to understand which processes might have led to the observed sea-ice formation on warm seawater.

5.3 A LAB STUDY ON SEA-ICE FORMATION ON WARM WATER

Motivated by observations of sea-ice formation on seawater the temperature of which was above its freezing point, I carried out a lab experiment to understand which processes can lead to sea-ice formation on warm seawater.

For multi-year ice, it was shown earlier that once sea ice exists, it can persist and even grow although the upper-ocean temperature is above its salinity-determined freezing temperature as long as ice conduction exceeds the oceanic heat flux [McPhee, 2008; MCPhee *et al.*, 2008]. However, the *formation* of sea ice on warm seawater has not been observed before.

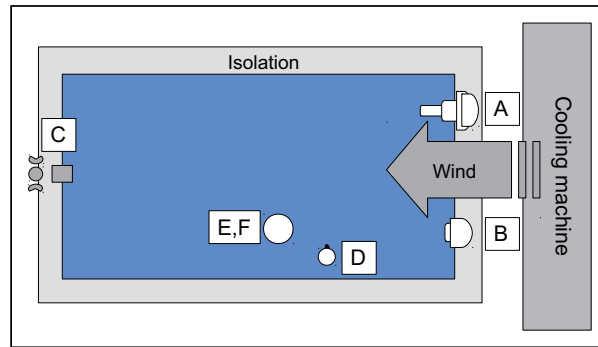


Figure 5.5: Tank setup during the experiment with sensors installed to measure (A) air temperature, (B) relative humidity, (C) wind speed, (D) temperature across the air-water-ice interface, and (E,F) temperature and salinity below the growing ice.

5.3.1 Setup and method

The experiment was carried out in an insulated tank with inside dimensions of $1.95 \times 0.67 \text{ m}^2$ and a height of 1.2 m, which itself is housed in a cold room of $3 \times 1.25 \text{ m}^2$ and a height of 2.25 m (see figure 5.5). The temperature of the cold room can be controlled down to $-25 \text{ }^\circ\text{C}$. De-frost cycles of the cooling machine induce fluctuations of the preset ambient temperature. During cooling cycles, the cold-room ventilator causes average wind velocities of about 0.25 m/s. The tank was filled up to a water level of 1 m with a sodium-chloride solution mixed to a salinity of 31.2 g/kg, which implies a freezing temperature of the solution of about $-1.87 \text{ }^\circ\text{C}$.

Heat panels were arranged along the tank sidewalls to avoid pressure generation caused by a complete ice cover. To simulate an oceanic heat flux of 4 W/m^2 , a heating cable was arranged on the floor of the tank to provide this heat flux. The cable also inhibited supercooling of the water below the growing ice. Air temperature⁷, wind⁸, and humidity⁹ sensors were arranged in a distance of 30 cm from the water/ice surface. The sampling interval of the sensors was set to 30 s. The temperature across the air-ice-water interface was measured using a thermistor rod with a spatial resolution ranging from 0.5 cm to 1 cm. The rod was made of teflon, had a diameter of 4.5 cm, and contained eight thermistors¹⁰. The sampling interval was set to 7 s. A conductivity-temperature sensor (CT)¹¹ was arranged 8 cm below the surface. The sampling interval of the CT was set to 10 s. Pumps were installed to mix the water prior to the experiment.

I started the experiment after the initial condition—a homogeneous temperature distribution within the tank of approximately $+1 \text{ }^\circ\text{C}$ —was reached. Then I switched off the pumps and turned the cold room to $-25 \text{ }^\circ\text{C}$, i. e., the strongest cooling possible.

7 Campbell 43347 RTD temperature probe with Campbell 43502 aspirated radiation shield
 8 Campbell A100R for velocity and Campbell W200P-1 for direction
 9 rotronic hygrometer MP 100 A with RS 12 T radiation shield
 10 2.2K3A1 Series 1 Thermistor, calibrated to an accuracy of $0.05 \text{ }^\circ\text{C}$
 11 SeaBird Electronics, SBE37

5.3.2 Results and discussion

The activation of the cooling machine immediately caused turbulence at the water surface. After 82 min, air temperature had decreased from -2 to -17 °C, relative humidity had increased from 47% to 70%, temperatures at the water surface and the water below had decreased to -1.43 °C and 0.5 °C, respectively, and the salinity was still at its initial value of 31.23 g/kg (figure 5.6).

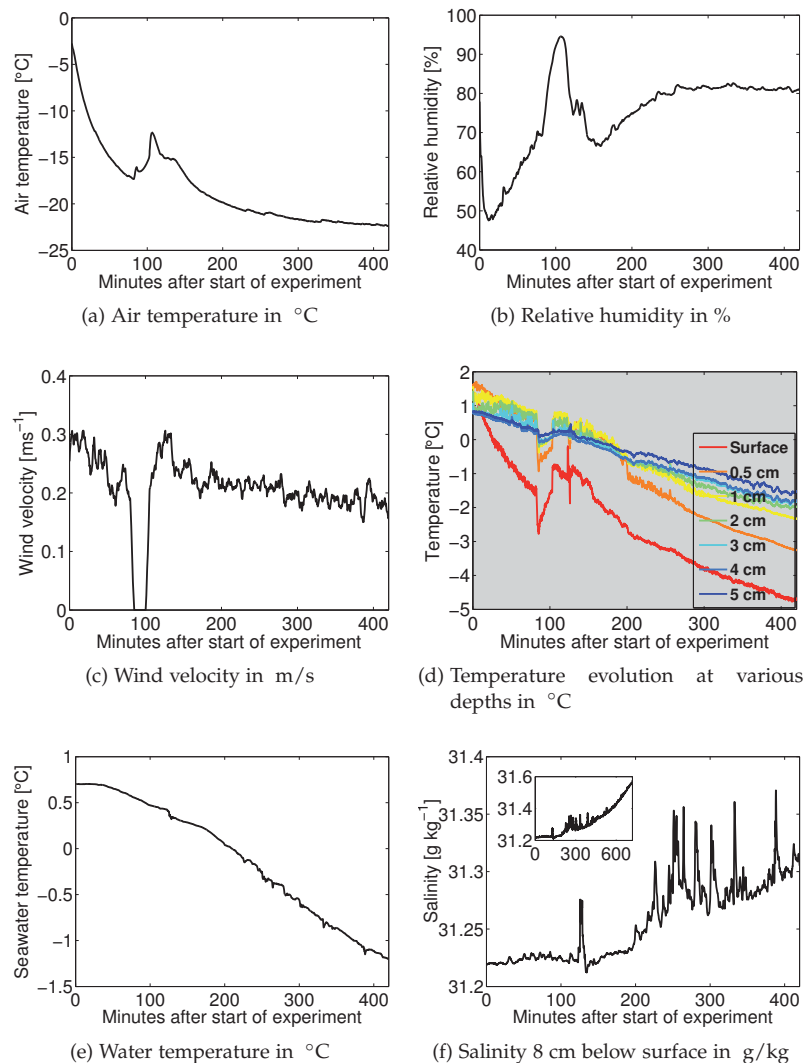


Figure 5.6: Temporal evolution of parameters measured across the air-ice-water interface.

At this point, a de-frost cycle of the cooling machine caused the wind speed to go down to 0 m/s. Within the next 3 min, the surface temperature decreased from -1.43 °C to -2.78 °C. Below the surface, a significant decrease in temperature can be observed down to 5 cm; the amount of cooling decreasing with depth (see figure 5.6d). During the next 17.5 min, the temperatures gradually increased up to almost the same value as before the strong decrease. Simultaneous to the observed temperature decreases and

increases, relative humidity increased from 69.7% to 94.6%, which was the highest value for the whole time of the experiment (see figure 5.6b). Salinity slightly increased by approximately 0.1 g/kg and showed frequent fluctuations of about 0.01 g/kg.

These temperature fluctuations indicate a tremendous supercooling of 0.9 °C at the water surface and show that heat was extracted from the upper water column, resulting in a strong increase in relative humidity above the surface. The observations also imply that wind speeds need to be very low for such a strong supercooling to occur. Fluctuations in salinity during that time were negligible.

With -0.75 °C, the surface temperature then was higher than prior to the supercooling (-1.43 °C). With the onset of the next freezing cycle 107 min after start of the experiment, the wind speed increased to approximately 0.25 m/s again and caused turbulence at the water surface. While the surface temperature began to decrease immediately, temperatures in the water below stayed almost constant. The surface temperature decreased to -1.17 °C within the following 16 min, accompanied by a relative-humidity decrease to 74.5%.

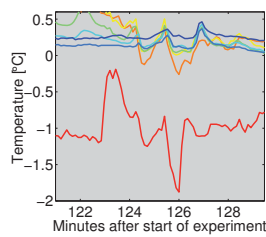


Figure 5.7: Zoom into equilibration

During the next 4 min (123 to 127), the surface temperature increased from -1.17 to -0.19 °C within 36 s, decreased from -0.19 to -1.25 °C within 78 s, slightly increased to -0.84 °C within 42 s, decreased to -1.87 °C within 36 s, and increased again to -1.1 °C within 42 s. Except for the initial increase of the surface temperature, which is accompanied by decreasing temperatures below the surface, a similar shape of the temperature fluctuations can be observed down to a depth of 5 cm. The fluctuations can even be observed 0.5 cm above the surface, where temperature fluctuated between -5.4 and -4.2 °C (not shown). Two minutes after the first strong temperature increase at minute 123, both a significant increase in salinity from 31.23 to 31.28 g/kg (see figure 5.6f) and temperature decrease from 0.42 to 0.32 °C were measured by the conductivity-temperature sensor 8 cm below the surface. Moreover, air temperature, wind speed, and relative humidity plateaued at -15 °C, 0.3 m/s and 76%, respectively. Salinity decreased to the initial value of 31.23 g/kg within the next 8 min.

Unfortunately, the state of the surface was not captured by a camera; hence, in the following, I can only infer what has happened. I argue that the processes described above (minute 123 to 127) happened when an initial nucleation of a very thin ice cover occurred. The first increase in surface temperature (minute 123) and the accompanying decrease of the temperatures below the surface show that heat was released from the surface (which is well known to happen during ice production [see e.g. Weeks, 2010]), and that the heat loss needed to form ice was extracted from the upper water column. Since the time of the surface-temperature decrease to -1.87 °C exactly coincides with the time of the strong salinity increase, and since the value of the negative peak of -1.87 °C was the salinity-determined freezing temperature, I conclude that this was initial thin-ice formation.

However, the curve progression of relative humidity suggests that a *continuous* ice cover did not form before the surface temperature had reached the freezing point, which was the case half an hour later (minute 163). An

explanation could be the irregular freezing of the water surface, which is caused by temperature gradients appearing due to the different wind conditions relative to the position of the cold-room ventilator. Relative humidity had decreased to 67% at that time, and started to increase until it reached approximately 80% after 260 min, where it lasted for the remainder of the experiment. Additionally, the temperature at a depth of 0.5 cm below the surface had decreased to the freezing temperature after these 260 min.

In any case, sea-ice formation occurred when the water below the surface was well above freezing. Assuming the ice formation occurred when the surface temperature had reached the freezing point, the temperature difference to the next sensor at a depth of 0.5 cm was 1.8 °C.

After the initial formation of the thin sea-ice layer in minute 163, a considerable increase in salinity accompanied by frequent deviations from the average salinity occurred. The frequent deviations stopped once the ice had grown to a thickness of 2 cm. Thereafter, the salinity was smoothly increasing to 31.6 g/kg at the end of the experiment after 12 h (see zoom-out in figure 5.6f). The final ice thickness was 5 cm.

The fact that the surface temperature during the initial formation of the thin sea-ice layer was lower by 1.8 °C than the temperature 0.5 cm below, suggests an upper bound for the seawater temperature at which sea-ice formation can occur to be about 1.8 °C above the freezing point. In the field, the difference between the freezing temperature and the temperature at 50 cm below the surface was about 0.6-0.7 °C on 10 January, the day on which the formation of a continuous ice cover was observed (see section 5.2.2).

However, additional lab experiments with even higher initial water temperatures and different simulated atmospheric temperatures and winds are needed to substantiate the observations and to be able to come up with a reliable statistic.

5.3.3 Conclusions

Sea-ice formation on seawater that is well above its freezing point is possible. Prerequisites for the formation to occur are low turbulences at the water surface and a sufficient temperature difference between ocean and atmosphere. Under these conditions, heat is extracted from the upper ocean, which leads to supercooling and initial nucleation of a thin ice cover that, once formed, prevents lower layers from atmospheric turbulence and effectively conducts heat, which further allows ice growth.

Together with the measurements we carried out in the field, these results take a step forward in getting an idea of prerequisites for the existence of Polar sea ice in a climate with oceanic temperatures above freezing.

5.4 HEAT-FLUX ESTIMATES

In this section, I investigate how the observed evolution of first-year sea ice influenced the heat exchange between atmosphere and ocean.

The total downward flux of heat across the ocean surface is determined by the radiative fluxes of net solar (H_{sw}) and net longwave (H_{lw}) radiation, and the turbulent fluxes of sensible (H_{sens}) and latent heat (H_{lat}).

$$H = H_{sw} - (H_{lw} + H_{sens} + H_{lat}) \quad (5.4)$$

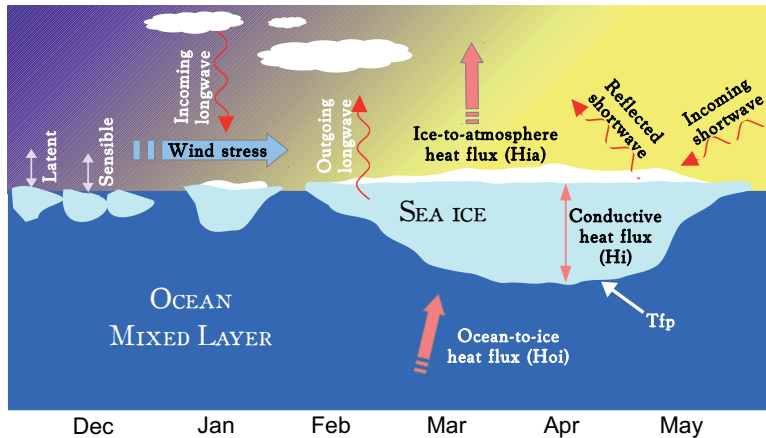


Figure 5.8: Sketch of sea-ice-heat budget.

The presence of sea ice significantly alters this energy exchange, as it moderates the momentum exchange by building an effective barrier between atmosphere and ocean, and as the ice reduces the heat input into the ocean by reflecting a significant amount of the incoming shortwave radiation. Hence, how much energy can be exchanged between atmosphere and ocean is determined by the ability of the ice to conduct heat, and by the thickness of the ice (see figure 5.8 for a sketch of involved fluxes). Both factors are different for perennial sea ice compared to first-year sea ice, which will be the prevailing sea-ice type in the near future. Hence, properly describing the heat fluxes at both the ice-atmosphere interface and the ice-ocean interface is essential for modeling the energy and mass balances. However, most of existing measurements were carried out over perennial sea ice. Measurements over first-year sea ice are rare, and the following heat-flux measurements will enhance our understanding of the heat exchange between atmosphere and ocean during the evolution of first-year sea ice.

5.4.1 Longwave and shortwave radiation

The basis for the calculation of the total heat flux that will follow are our radiation measurements, which I will shortly describe in this section.

Measured net longwave and shortwave radiation at the water/ice surface are shown in figure 5.9. Longwave and shortwave quantities were obtained by converting the measured voltages of the pyrgeometers and pyranometers to incoming and outgoing longwave radiation, and incoming and reflected shortwave radiation, respectively. Sometimes net-shortwave balances showed small deviations to positive values during night, which would imply an impossible negative albedo. Those data were manually set to zero. Moreover, shortwave-radiation measurements are reliable only once the solar elevation angle was above 10° (mentioned by manufacturer), which is why data were removed from the time series when the angle was below 10° . Hence, shortwave-radiation measurements will be included in the heat-flux calculations from beginning of March 2010.

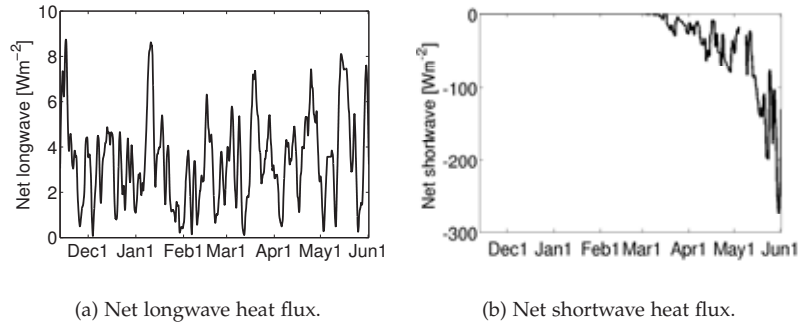


Figure 5.9: (a) Net longwave radiation, averaged over a sliding window of one day.
(b) Net shortwave radiation, averaged over a sliding window of 12 h.

5.4.2 Surface-temperature estimation

To properly calculate turbulent heat fluxes and the total heat flux, an appropriate water/ice surface temperature is essential. Since we did not measure the temperature at the water/ice surface directly, the surface temperature was derived from the emitted $Q_{L\uparrow}$ and incoming $Q_{L\downarrow}$ longwave radiation [Andreas *et al.*, 2010a] measured by the radiometer as:

$$T_{\text{surf},lw} = (\sigma \varepsilon)^{-1/4} \{H_{L\uparrow} - (1 - \varepsilon)H_{L\downarrow}\}^{1/4}, \quad (5.5)$$

where σ is the Stefan-Boltzmann constant and the surface emissivity ε is 0.99 [Jordan *et al.*, 1999]. The result is shown as the blue curve in figure 5.10. However, I do not trust the result. Even though daily averaged air tempera-

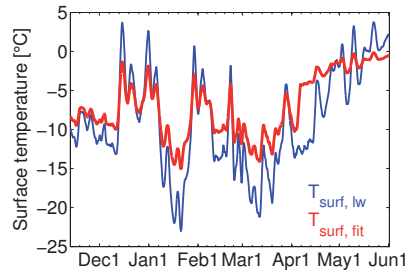


Figure 5.10: Surface temperature derived from measurements of longwave radiation (blue curve) and from fit between longwave-derived and measured temperature. See text for details.

ture data show maxima of +4 °C for short periods in December and January, I do not believe that the water surface was as warm as the air. The same impression holds for periods of air temperatures below -15 °C. In both cases, longwave-derived surface temperatures seem to be overestimated relative to the absolute value.

Hence, a second estimate of the surface temperature was applied by using the temperature we measured at the surface of the ice from the end of March until mid May 2010. The measured surface-temperature data were linearly fitted to the longwave-derived surface temperature during the same period. High variations in air temperature and thus surface temperature during this

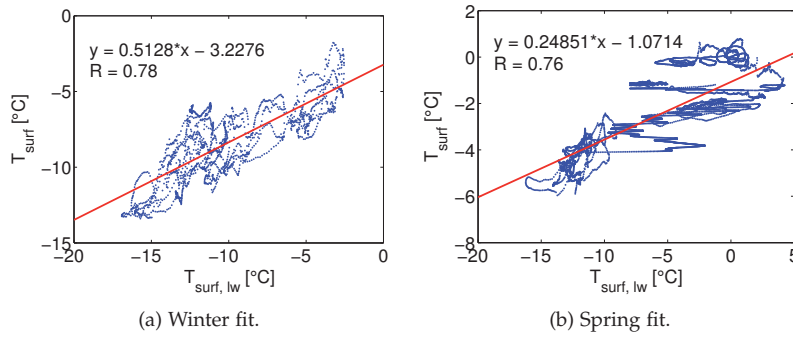


Figure 5.11: Linear fits to derive the surface temperature from longwave-radiation measurements during (a) winter conditions, and (b) spring conditions. Note different x-axes and y-axes.

time of a transition from a winter state to a summer state allow for a split of the fitted data to respective periods. Equations and R-values for the respective fits are shown in figure 5.11. The result of the fitted surface temperature is shown as a red curve in figure 5.10 above. It reveals the possible failure we might get in deriving the surface temperature of sea ice from measurements of the longwave radiation using equation 5.5. However, to me it seems more reliable, and the fitted surface temperature $T_{\text{surf,fit}}$ has been used for the following heat-flux calculations.

5.4.3 Turbulent heat exchange

Turbulence in the atmospheric boundary layer causes sensible and latent heat fluxes. Sensible heat is the heat flux that is caused by the temperature difference at the ice-atmosphere interface. The temperature difference leads to a transfer of heat down the temperature gradient and is strongly influenced by wind and small eddies in the boundary layer. Latent heat, the heat transfer that occurs due to sublimation or evaporation at the surface, is also strongly influenced by the wind conditions. The sensible heat was calculated as

$$H_{\text{sens}} = \rho_a \cdot C_d \cdot u \cdot c_{p_a} \cdot (T_{\text{surf}} - T_a), \quad (5.6)$$

where ρ_a is density of air, C_d is the drag coefficient, u is wind speed, c_{p_a} is specific heat of air, and $(T_{\text{surf}} - T_a)$ is the difference between surface and air temperatures. Latent heat was calculated as

$$H_{\text{lat}} = \rho_a \cdot C_d \cdot u \cdot L_{\text{vap}} \cdot (q_{\text{surf}} - q_a), \quad (5.7)$$

where L_{vap} is latent heat of vaporization, and $(q_{\text{surf}} - q_a)$ is the difference between specific humidities at the surface and 2 m above surface. Quantities were calculated following parameterizations given in *Andreas* [2005]. Results are shown in figure 5.12.

I find strongest positive sensible heat fluxes of about 120 W/m^2 for the period of the initial formation of a continuous ice cover in the bay in January. From 6 April until 23 April, the sensible heat flux was approximately 60 W/m^2 . During this period, warming-induced gravity drainage was observed (chapter 3). The strongest negative sensible heat fluxes occurred during the storm events on 13 and 31 December 2009. Latent heat flux was

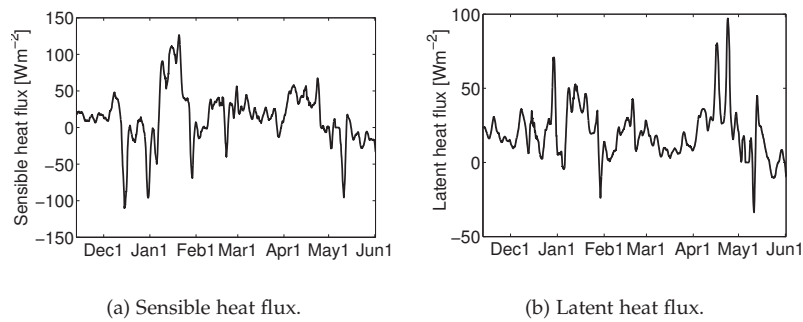


Figure 5.12: Turbulent heat fluxes. (a) sensible heat flux (b) latent heat flux. Data were averaged over a sliding window of one day.

highest during two storms in April, which was at the time when a considerable desalination of the whole ice column was observed (see chapter 3).

5.4.4 Methods for heat-flux calculations

The total heat flux was obtained by using two different implementations of the boundary-layer formulations. In principle, both formulations are physically equivalent in that the longwave, sensible and latent heat fluxes are linearized. However, using both implementations provides a minimum estimation of uncertainties.

1. **HANEY METHOD:** The charm of this method arises from the fact that the upward heat flux across the ocean surface is given in terms of an apparent atmospheric equilibrium state as:

$$H = H_2 \cdot (T_a^* - T_{\text{surf}}), \quad (5.8)$$

where

$$T_a^* = T_a - H_1/H_2, \quad (5.9)$$

with H_1 containing net downward fluxes of solar radiation and upward fluxes of longwave radiation and latent heat across and from the ocean surface at air temperature T_a ; and H_2 contains net upward fluxes of longwave radiation and sensible and latent heat per degree Celsius excess of the ocean-surface temperature over the atmospheric equilibrium temperature T_a (see *Haney* [1971] for details).

Parameters such as the saturation-vapor pressure, air density, latent heat of vaporization and so forth that are needed to calculate sensible and latent heat fluxes were calculated according to formulas in *Andreas* [2005]. The drag coefficient was calculated after *Andreas et al.* [2010a, pg. 933].

2. **ANDREAS METHOD:** This method relies on state-of-the-art formulations of turbulent exchanges over both winter and summer sea ice, where multiple data sets collected during the year-long experiment to study the Surface Heat Budget of the Arctic Ocean (SHEBA, from 1997 to 1998) were used to develop a bulk-flux algorithm for predicting the surface fluxes of momentum and sensible and latent heat [*Andreas et al.*, 2010a,b, and references therein]. The algorithm used here was

downloaded from <http://www.nwra.com/resumes/andreas/software.php>, and slightly modified to handle long time series.

For both methods, the ice concentration that is contained in the formulae is an important factor concerning the drag-coefficient calculation, and I did a raw guess of the percentual ice coverage by applying the visual observations and the estimates from our measurements of relative humidity with respect to ice saturation (see also section 5.2.3). Hence, an ice concentration of 100% was applied for March only, when both the bay and the sound were ice covered. In the remaining time, the ice concentration was below 99%, so that using the Andreas method, all heat fluxes were calculated as for conditions over summer sea ice.

5.4.5 Results and discussion

Measurements of incoming and outgoing longwave and shortwave radiation, wind speed, air temperature, relative humidity, barometric pressure, and the estimated ice concentration and surface temperature were used to calculate the net heat flux at the water/ice surface by using the two methods described above. Resulting heat fluxes are shown in figure 5.13 together with the bulk heat flux of the ice for the period from end of March until mid May, when temperature measurements in the ice were available. Bulk conductive heat flux of the ice was calculated by

$$H_{\text{bulk, ice}} = -k \cdot \frac{T_{i,s} - T_{i,\text{bot}}}{h}, \quad (5.10)$$

where $T_{i,\text{surf}}$ and $T_{i,\text{bot}}$ are the temperatures at the ice surface and ice bottom, respectively, h is ice thickness, and the thermal conductivity of the ice k was calculated dependent on measured bulk salinities and temperatures. Black crosses indicate times when strong deviations from average oceanic salinity and temperature were observed (see chapter sr for details). A positive value for the heat flux corresponds to a heat flux from the ocean/sea-ice surface to the atmosphere.

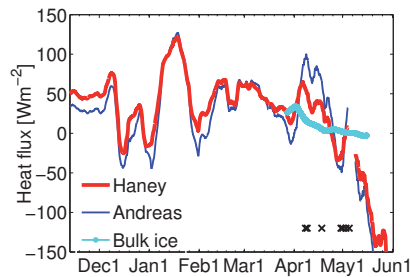


Figure 5.13: Daily averaged heat flux calculated with described methods. Red curve shows net heat flux calculated with Haney method, blue curve shows net heat flux calculated with Andreas method. Light blue shows bulk heat flux of the ice. Black crosses indicate times when strong deviations from average oceanic salinity and temperature indicated brine outflow.

Striking is the similarity of both heat fluxes during times of high ice production and a continuous ice cover (as was the case in January and March). During transitions from partly ice-covered to ice-covered states or vice versa,

the differences between both heat-flux estimates are highest, peaking at 46 W/m^2 during the transition from winter to spring on 8 April. With decreasing ice coverage at the end of the field study, the agreement between both fluxes increases again. On average, the results obtained by the two methods differ by 9 W/m^2 , the heat flux calculated with the Haney method being higher. Negative values indicate a changeover of the heat-flux direction from ocean-to-atmosphere to atmosphere-to-ocean (for example on 13 December 2009 and 1 January 2010).

In the period from beginning until mid of April, the heat fluxes calculated with the Andreas method seem overestimated, because solar radiation was increasing during that time, indicating that more heat must have been put into the surface. Nevertheless, the fluxes calculated with the Andreas method strongly increase to values comparable to those obtained during ice production. Since the Andreas algorithm also considers the appearance of melt ponds at specified air temperatures, but melt ponds did not appear on the ice during that time, the increase might have been caused by different calculations of the drag coefficient over melt ponds, or a different handling of the percentual ice coverage.

For the Haney-method results, the surface received more heat as the sun was rising as expected. This seems more reliable to me and I will focus on the heat-flux changes calculated with the Haney method hereafter.

Dependent on ice coverage, more or less heat was put into the ocean during storms. For example, the storms both on 1 January and 16 April showed the same wind speed of 17.8 m/s . On 1 January, the bay was ice free, and the heat flux changed from $+76 \text{ W/m}^2$ to -21 W/m^2 . In contrast, the decrease in heat flux from $+38 \text{ W/m}^2$ to $+15 \text{ W/m}^2$ on 16 April, when the bay was covered by 30-35 cm thick sea ice, is comparatively small. This gives but one expression of how effective already 30 cm thick sea ice is in moderating the heat exchange between atmosphere and ocean by building a barrier and impeding momentum exchanges between the two.

With 121 W/m^2 , heat fluxes were highest during the initial formation of a continuous ice cover on 10 January. In February and at the beginning of March, when a continuous ice cover formed a second time after a storm had destroyed the initial continuous ice cover at the end of January, the average heat flux from the ice surface to the atmosphere was about 63 W/m^2 . As the sun was considerably rising above the horizon at the beginning of March, the heat flux decreased to 12 W/m^2 on 29 March. The heat flux then strongly increased to 65 W/m^2 on 6 April, which might be explicable by the melting of the only 10 cm thin ice cover in the sound close-by, caused by the strong air-temperature increase at the end of March (see figure 5.2a). Heat flux then gradually decreased to -34 W/m^2 on 25 April. From 25 April to 5 May, the heat flux increased from -34 W/m^2 to 10 W/m^2 , and decreased to -34 W/m^2 again. During this period, a temperature changeover in the ice from highest temperatures at the ice bottom to highest temperatures at the ice surface was observed (see chapter 3). The bulk heat flux in the ice did not change considerably and was about 1 W/m^2 during the whole time of the temperature changeover.

The heat flux further decreased to -59 W/m^2 on 12 May, when flushing was observed (see chapter 3). The heat flux was about -65 W/m^2 during the onset of ice melt on 15 May 2010; and gradually decreased to -138 W/m^2 when all ice in the bay had melted.

The results show that during initial ice formation in winter, the heat released to the atmosphere was twice as high as the heat the atmosphere received once the ice had reached its equilibrium thickness. With sun rising above the horizon, the amount of heat released to the atmosphere gradually decreased until all ice had melted. This decrease was interrupted once the heat flux approached zero. The onset of an ice-temperature changeover, accompanied by a frequent outflow of brine from the ice was observed beginning at that time. This can be seen as an equilibration of the whole system, where the heat the ice received from the atmosphere resulted in an ice-temperature changeover, accompanied by frequent brine release until both the ice temperature and the ice salinity were almost homogeneous throughout the whole ice column (see also chapter 3). Once the ice had adapted to air and ocean temperatures, all heat supplied by the atmosphere resulted in melting of the ice.

5.4.6 Estimation of heat-transfer coefficients

One of the least known coefficients in modeling the heat exchange between ocean and atmosphere in coupled climate models is the heat-transfer coefficient between ocean and ice. Due to this uncertainty, various values for this coefficient have been used in several modeling studies in the past, ranging from 2-250 W/m²K [see e. g. *Yang and Neelin, 1993; Zhang et al., 1995; Yang and Neelin, 1997; Gordon et al., 2000*]. Thus, the estimation of the heat-transfer coefficient between ocean and ice based on our data will give new insights into the possible variability of this coefficient during the formation, growth and melt of first-year sea ice.

To estimate the coupling coefficients between both ice and atmosphere and ocean and ice, I used a simple energy-balance model, where for simplicity the ice is assumed to have zero heat capacity; and the ice-bottom temperature is assumed to be at the salinity-determined freezing temperature T_{fp} .

Applying the Haney method, the upward heat flux across the water/ice surface is calculated in terms of an atmospheric equilibrium state [*Haney, 1971*]. The equilibrium state is represented by an *apparent* equilibrium air temperature T_a^* , a coupling coefficient λ , and the ice-surface temperature T_{is} as

$$H_{ia} = \lambda (T_{is} - T_a^*). \quad (5.11)$$

The heat flux at the ice bottom H_{ib} is calculated as

$$H_{ib} = -k \left(\frac{T_{fp} - T_{is}}{h} \right), \quad (5.12)$$

where $k = 2$ W/mK is thermal conductivity of the ice, h is ice thickness and T_{fp} ¹² is the temperature at the ice bottom. Every heat that is necessary to grow or melt the ice must equal

$$L_f \rho_i \frac{dh}{dt} = H_{ib} - H_{oi} \quad (5.13)$$

where L_f is the latent heat of fusion of sea ice, ρ_i is ice density, and the heat flux at the ice bottom H_{oi} is

$$H_{oi} = \gamma (T_o - T_{fp}). \quad (5.14)$$

¹² fp stands for freezing point

T_o is the ocean near-surface temperature, which we measured at a depth 50 cm below the growing and melting ice. The balance at the ice-ocean interface is

$$L_f \rho_i \frac{dh}{dt} = -k \left(\frac{T_{fp} - T_{is}}{h} \right) - \gamma (T_o - T_{fp}). \quad (5.15)$$

Hence, the ice growth is a function of the temperature at the ice bottom, oceanic temperature, and the temperature at the surface of the ice ($h = h(T_{fp}, T_o, T_{is})$); and the temperature at the ice surface is determined by the ice-bottom temperature, the ice thickness, and the equilibrium air temperature ($T_{is} = T_{is}(T_{fp}, h, T_a^*)$).

In thermal equilibrium, the ice neither grows nor melts ($\frac{dh}{dt} = 0$), and the heat flux at the bottom of the ice is balanced by both the ocean-ice heat flux ($H_{ib} = H_{oi}$), and the ice-atmosphere heat flux ($H_{ib} = H_{ia}$). Thus we arrive at

$$\lambda (T_{is} - T_a^*) = \gamma (T_o - T_{fp}), \quad (5.16)$$

where λ is the heat-transfer coefficient between ice and air, and the only unknown is γ , the heat-transfer coefficient between ocean and ice, which now can be calculated as

$$\gamma = \frac{\lambda (T_{is} - T_a^*)}{(T_o - T_{fp})}. \quad (5.17)$$

The calculated coupling coefficient between ocean and ice is shown together with the coupling coefficient between the water/ice surface and the atmosphere in figure 5.14.

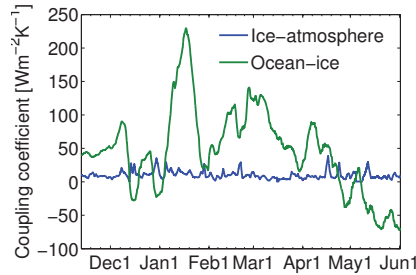


Figure 5.14: Estimated heat-transfer coefficients between both ice and atmosphere, and ocean and ice, averaged over a sliding window of one day.

As for the surface heat flux, highest values for the heat-transfer coefficient between ocean and ice can be found during the formation of an initial continuous sea-ice cover on 10 January, and when the ice had reached its maximum thickness of 30-35 cm in March. Interestingly, the values of 230 W/m^2K and 130 W/m^2K obtained during these times, respectively, agree with the range of values for heat-transfer coefficients between ocean and ice of 125-250 W/m^2K that were applied by *Zhang et al.* [1995], since their model results were not sensitive to the coefficients in this range only.

With decreasing ice coverage and increasing air temperature, the coefficient gradually decreased until it showed about $-60 W/m^2K$ when all ice had

melted. Normally, it is necessary to also consider the speed of oceanic currents below the ice and ice-bottom topography [McPhee *et al.*, 2008]. However, currents were almost absent in the bay and the ice-bottom topography was very smooth. Hence, the formulations given above are applicable for our measurements.

The heat-transfer coefficient between the surface and the atmosphere ranges from a minimum of 0.5 to a maximum of 39 W/m²K, where the latter was observed during the storm on 16 April 2010. In general, the transfer coefficient between ice and air decreased with increasing ice coverage, which can be explained by the wind speed, which was decreasing with increasing ice coverage, too. Moreover, the occurrence of storms decreased with increasing ice coverage (see figure 5.2d).

5.4.7 Estimation of ice thickness

Based on the theoretical considerations above, it should also be possible to estimate the ice thickness from heat-flux measurements as

$$h = \frac{k}{\gamma} \frac{T_{fp} - T_a^*}{T_o - T_{fp}} - \frac{k}{\lambda}. \quad (5.18)$$

The result was quite noisy though, and I removed unreliable fluctuations such as ice thicknesses of, for example, ± 1000 m. After removing these values, the result was smoothed with a moving average lowpass filter over a sliding window of both three days and one week. Results are shown in figure 5.15, together with in-situ measured ice thicknesses obtained by ice-core measurements and visual observations.

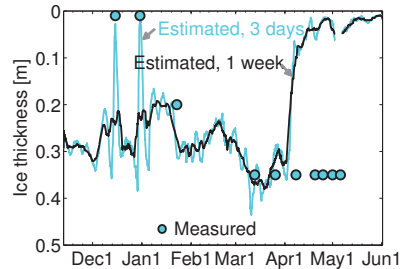


Figure 5.15: Estimated ice thickness, averaged over a sliding window of both, three days and one week.

Estimated ice thicknesses agree well with measured ice thicknesses. Even completely ice-free states were estimated, using the result that was smoothed over three days. Uncertain is the estimated ice thickness at the beginning of February, when the initial continuous ice cover was destroyed by a storm and the ice was broken into ice floes. However, floes still were present and their thickness might have been about 0.3 m, when the floes were pushed against and on top of each other. However, I am lacking information on effects like this and thus the thickness estimate at the beginning of February needs to be called into question.

However, most striking is the deviation between measured and estimated ice thicknesses, starting from the beginning of April. Although the ice in

the bay showed a thickness of 30-35 cm from mid March until 9 May 2010 (the day on that we arrived to recover some instruments), the estimated ice thickness strongly decreases to almost 5 cm within about six days from 30 March to 6 April, and further decreased to a thickness of 0 cm thereafter.

To investigate why estimated and measured ice thicknesses do not agree anymore, I subtracted the difference between the lower boundary of the atmosphere, i. e., the surface temperature $T_{i,s}$ and the upper bound of the atmosphere, i. e., the air temperature T_a , from the difference between the temperature at the lower boundary of the ice, i. e., the assumed ice-bottom temperature T_{fp} and the temperature at the upper boundary of the ice, i. e., the surface temperature $T_{i,s}$.

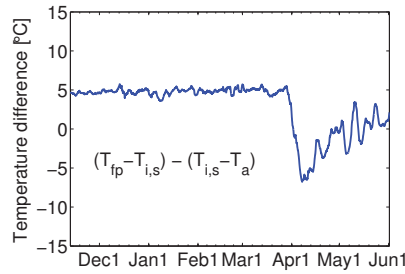


Figure 5.16: Difference between bulk-ice and surface-air temperatures.

The result (see figure 5.16) shows almost constant temperature differences of about 5 °C from November 2009 until 29 March 2010. On that day, the differences steeply decreased to about -6 °C on 6 April, and then gradually increased to 0 °C at the end of the field study. The interpretation of the result is more straightforward, if we re-write the differences to

$$(T_{fp} - T_{i,s}) - (T_{i,s} - T_a) = T_{fp} - 2T_{i,s} + T_a. \quad (5.19)$$

This is the discretization of the Laplacian operator and thus stands for a diffusive heat-flux convergence, indicating if heat is accumulated at the surface, or if heat is dissipated at the surface. This is only possible with an additional heat-transport process. Likely candidates are the lateral transport of heat due to the melting of the thin ice in the sound, which was accompanied by an increase in the absorption of solar radiation into the ocean; and local melting of the ice and accompanied increased evaporation from the ice surface.

To study the changing relation between the difference between surface and air temperature and the bulk-ice temperature separately, I cross correlated the two temperature differences over a sliding window of 20 days at the 99% confidence interval. The result is shown in figure 5.17.

It becomes abundantly clear that something significant must have happened during the period from approximately 12 March to 25 April. Before discussing this period, I describe the remainder of the correlations.

The correlation between the difference between surface and air temperature and bulk-ice temperature was positive for the whole time from December 2009 to May 2010. As indicated by the lag of maximum correlation, the the heat provided by the atmosphere reaches the ice after approximately three

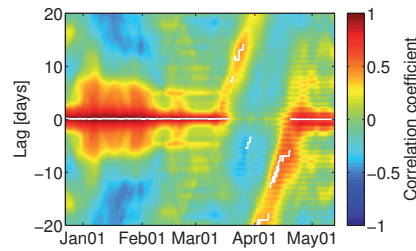


Figure 5.17: Cross correlation between difference between surface and air temperature and bulk-ice temperature over a sliding window of 20 days. White line marks the lag of maximum correlation.

hours with correlation coefficients above 0.95 prior to 18 March. After 19 April, the lag is 0 hours, indicating that heat was transported immediately from one medium to the other. Correlation coefficients decreased from 0.93 to 0.81 in mid May.

During the period from 12 March until 25 April, the correlation at lag zero considerably decreases to a correlation of about 0. Striking is the appearance of the daily cycle starting from 12 March, which can be identified as stronger signals at a lag distance of one day. Starting on 12 March, the lag of maximum correlation increases accompanied by a decrease in correlation until approximately 26 March. At this point, the maximum correlation is negative for a period of about four days. From 27 March until the end of the field study, the maximum correlation was positive again, but the lag of maximum correlation had turned from positive to negative.

The correlation shows that with increasing solar radiation, something happened that led to a complete changeover of the atmosphere-ice system. Interestingly, the period of negative lags and positive correlations coincide with the appearance of warming-induced gravity drainage, which was discussed in a previous chapter of this thesis (see chapter 3). Moreover, I indicated a frequent release of brine from the ice accompanied by an ice-temperature changeover beginning on 21 April in chapter 3, which coincides with the time of the maximum correlation appearing at lag zero in this chapter. Hence, the accumulation of heat at the surface led to and increase in the liquid fraction of the ice and warming-induced gravity drainage.

These results substantiate the assumption already made in the previous sections in that the sound, which was covered by 10 cm thin ice in March, got ice free due to the overall increasing air temperature and solar radiation at the beginning of April. Hence, the ice-free conditions in the sound that was only a few hundred meters apart from and connected to the bay, influenced the conditions in the bay, too. The absorption of the increasing solar radiation in the sound strongly affected air and ice temperatures in the bay. Moreover, due to the increasing open-water fraction, the wind conditions and relative humidity changed. Both changes we can find at the time the melting of the sound is likely to have been occurred as a strong decrease in relative humidity with respect to ice and an increase in wind speed (see figure 5.2c and d).

Hence, the estimation of the ice thickness failed from April until the end of the field study, because the higher absorption of solar radiation in the ice-free sound affected the heat fluxes through the ice that was present in

the bay until 20 May 2010.

5.5 SUMMARY AND CONCLUSIONS

In this chapter, I investigated how the formation, growth and melt of first-year sea ice influenced both physical properties above and below the water/ice surface and the heat exchange between the ocean surface and the atmosphere.

I have shown that the relative humidity with respect to ice can serve as a diagnostic tool to determine states of sea ice. When sea ice grows, relative humidity with respect to ice shows supersaturation, when sea ice is in equilibrium with its surroundings, relative humidity with respect to ice is near saturation, and when sea ice melts, relative humidities with respect to ice and water are of equal magnitude.

I have discussed results that I obtained during a lab study, carried out to investigate how sea-ice formation can occur on seawater with temperatures well above freezing. I have shown that sea-ice formation can occur even if the water temperature is not at its salinity determined freezing point.

Heat flux reached its maximum of 121 W/m^2 during the initial formation of a continuous sea-ice cover. When sea ice reached its equilibrium thickness, the heat delivered to the atmosphere was about 63 W/m^2 . The onset of ice melt occurred, when the ice surface received approximately 65 W/m^2 .

I estimated the heat-transfer coefficient between ocean and ice, which is one of the least known parameters in climate models. The coefficient was highest with $230 \text{ W/m}^2\text{K}$ during the initial formation of a continuous sea-ice cover, and reached about $130 \text{ W/m}^2\text{K}$ once a stable ice cover had evolved.

I have shown that—within limits—it is possible to estimate the ice thickness from radiation and temperature measurements in both atmosphere and ocean.

The data and results presented in this study represent the thermal response of first-year sea ice that grew under calm conditions and on seawater that was well above its freezing point. The results might be used to investigate the influence of sea-ice and ocean dynamics on the observed freezing and melting processes in a warmer climate with oceanic temperatures well above freezing.

Part VI

SUMMARY

Many recent reports indicate that a significant shrinkage of the Arctic Ocean pack ice has occurred during the first half of the 20th century ... other investigators have speculated on the climatic consequences of an ice-free Arctic Ocean. In view of these reports and speculations, it seems appropriate to estimate whether an ice-free condition of the North Polar Sea (the name often used for the central ice-covered part of the Arctic Ocean) can be maintained by the resulting thermal regime. To make such an estimate we must examine the pertinent factors of the present heat balance of this region to deduce the changes that would occur upon the disappearance of the ice, whether from natural or artificial causes. Admittedly, the magnitudes of many of the values involved are still uncertain, but, within limits, a reasonable approach to the problem can be made. When available, data from polar-orbit satellites will permit refinement of results.

— William L. Donn, 1966

SUMMARY

In this thesis, I investigated processes involved in the seasonal variation of first-year sea ice. I conclude by giving concise answers to the research questions posed in the introduction. For more detail, please refer to the individual conclusions of chapters 2, 3, 4 and 5.

FROST FLOWERS AND SEA ICE

What are possible condensation nuclei for frost flowers? How do the temperatures above, within, and below frost-flower-covered ice evolve compared to those for bare ice at the same level? Is there a dependency between the salinity evolution of both frost flowers and the underlying sea ice? Do frost flowers influence the thickness and morphology of the underlying sea ice?

Based on various visual observations and the temperature measurements, I suggest sea-ice platelets that have a higher solid fraction than the surrounding platelets to serve as condensation nuclei for frost flowers. From the measurements I obtained during field and lab studies, I conclude that frost-flower-covered sea ice grows more slowly and is warmer than bare ice that grew under the same environmental conditions, which results in frost-flower-covered sea ice being thinner than bare ice. I find the salinity of frost flowers to be dependent on the bulk salinity of the underlying sea ice, as both salinities were decreasing with age, and the frost-flower salinities being higher on sea ice with a higher bulk salinity. During melting, the salty frost-flower meltwater dissolves the underlying sea ice and increases the permeability of the ice, which leads to a faster melting process.

SEA-ICE DESALINATION

Which processes lead to the desalination of first-year sea ice during its transition from winter to summer?

During the winter-spring-summer transition, the enhanced warming of the ice caused a changeover of the whole ice column from highest temperatures at the ice bottom to highest temperatures at the ice surface. This temperature changeover was accompanied by a stabilization of the density profile, a considerable increase of ice permeability, and a continuous outflow of brine until an almost homogeneous temperature and salinity profile was reached. The bulk salinity of 6 g/kg at the end of the changeover was comparable to the bulk salinity of young, multi-year sea ice. Flushing occurred 4 days later and further decreased the bulk salinity of the ice. The observed overall warming of the ice caused considerable melting of the salty ice surface, which led to an increase in the brine volume. Due to the unstable density profile, the salty brine moved towards the ice bottom, thereby dissolving the freshwater-ice matrix and considerably increasing the permeability of the ice, which enhanced the outflow of brine. Hence, during the winter-spring transition, sea ice desalinated by warming-induced permeability drainage.

IN SITU BULK-SALINITY MEASUREMENTS

How applicable are electrical impedance measurements between two thin metallic wires to obtain the bulk-salinity evolution of sea ice in situ?

The sensitivity studies show the individual wire pairs to be highly sensitive to environmental conditions, which results in different values for the impedance even under the same conditions. I observed mechanical deformation of the wires by the ice growing in between them, which implies the conductivity-cell calibration not to hold anymore. Moreover, the instrumental setup modifies the properties of the ice the instrument is supposed to measure. Hence, I call the applicability of the current version of this instrument into question.

HEAT FLUX THROUGH FIRST-YEAR SEA ICE

How does the formation, growth, and melt of first-year sea ice influence the heat exchange between ocean and atmosphere? How can sea-ice formation occur on seawater that is well above its freezing point? Is it possible to estimate ice thicknesses and ocean-to-ice heat-transfer coefficients from the derived surface heat fluxes?

I find that highest surface-heat fluxes of 121 W/m^2 occurred during the initial formation of a continuous sea-ice cover. When the ice reached its equilibrium thickness, the heat delivered to the atmosphere was about 63 W/m^2 . The onset of ice melt occurred, when the ice surface received approximately 65 W/m^2 . From results of a lab study and the field measurements, I conclude that sea-ice formation on seawater that is well above its salinity determined freezing temperature is possible. Prerequisites for the formation to occur are low turbulence at the water surface and a sufficient temperature difference between ocean and atmosphere. Under these conditions, heat is extracted from the upper ocean, which leads to supercooling and initial nucleation of a thin ice cover that, once formed, prevents lower layers from atmospheric turbulence and effectively conducts heat, which further allows ice growth. I successfully estimated ice thicknesses and the heat-transfer coefficient between ocean and ice, which is one of the least known parameters in climate models. The estimation was valid until accumulation of heat at the ice surface induced melting of the ice interior.

BIBLIOGRAPHY

- K Aagaard, LK Coachman, and EC Carmack. On the halocline of the arctic ocean. *Deep-Sea Research*, 28A(6):529–545, 1981. (Cited on pages 3, 38, 71, and 72.)
- EL Andreas. *Handbook of physical constants and functions for use in atmospheric boundary layer studies*. US Army Cold Regions Research and Engineering Laboratory, Hanover, NH, 2005. (Cited on pages 79 and 80.)
- EL Andreas, PS Guest, POG Persson, CW Fairall, TW Horst, RE Moritz, and SR Semmer. Near-surface water vapor over polar sea ice is always near ice saturation. *Journal of Geophysical Research*, 107(C10):SHE8–1–15, 2002. (Cited on pages 67 and 69.)
- EL Andreas, TW Horst, AA Grachev, POG Persson, CW Fairall, P Guest, and RE Jordan. Parameterizing turbulent exchange over summer sea ice and the marginal ice zone. *Quarterly Journal of the Royal Meteorological Society*, 136:927–943, 2010a. (Cited on pages 78 and 80.)
- EL Andreas, POG Persson, RE Jordan, TW Horst, PS Guest, AA Grachev, and CW Fairall. Parameterizing turbulent exchange over sea ice in winter. *Journal of Hydrometeorology*, 11(1):87–104, 2010b. (Cited on page 80.)
- AL Buck. New equations for computing vapor-pressure and enhancement factor. *Journal of Applied Meteorology*, 20(12):1527–1532, 1981. (Cited on page 68.)
- EC Carmack. *The Arctic Ocean's freshwater budget: Sources, storage and export*. Dordrecht: Kluwer Academic Publishers, 2000. (Cited on pages 3, 38, 71, and 72.)
- AOP Chiareli and MG Worster. On measurement and prediction of the solid fraction within mushy layers. *Journal of Crystal Growth*, 125(3-4):487–494, 1992. (Cited on page 59.)
- JC Comiso. A rapidly declining perennial sea ice cover in the Arctic. *Geophysical Research Letters*, 29(20):17–1–4, 2002. (Cited on pages 3, 38, and 64.)
- GFN Cox and WF Weeks. Salinity variations in sea ice. *Journal of Glaciology*, 13(67):109–120, 1974. (Cited on pages 4 and 38.)
- GFN Cox and WF Weeks. *Brine Drainage and Initial Salt Entrapment in Sodium Chloride Ice*. US Army Cold Regions Research and Engineering Laboratory, Hanover, NH, 1975. (Cited on page 39.)
- F Domine, AS Taillandier, WR Simpson, and K Severin. Specific surface area, density and microstructure of frost flowers. *Geophysical Research Letters*, 32(13):4 pp, 2005. doi: 10.1029/2005GL023245. (Cited on page 16.)
- EE Ebert, JL Schramm, and JA Curry. Disposition of solar radiation in sea-ice and the upper ocean. *Journal of Geophysical Research*, 100(C8):15965–15975, 1995. (Cited on page 64.)

- H Eicken. *From the Microscopic, to the Macroscopic, to the Regional Scale: Growth, Microstructure and Properties of Sea Ice*. Blackwell Science Ltd, 2003. (Cited on pages 3, 39, and 50.)
- H Eicken, R Gradinger, M Salganek, K Shirasawa, D Perovich, and M Lepäranta. *Field techniques for sea ice research*. University of Alaska Press, 2009. (Cited on pages 4, 38, 41, and 66.)
- H Eicken, HR Krouse, D Kadko, and DK Perovich. Tracer studies of pathways and rates of meltwater transport through Arctic summer sea ice. *Journal of Geophysical Research*, 107(C10), 2002. doi: {10.1029/2000JC000583}. (Cited on pages 39 and 43.)
- H Eicken, TC Grenfell, DK Perovich, JA Richter-Menge, and K Frey. Hydraulic controls of summer Arctic pack ice albedo. *Journal of Geophysical Research*, 109(C8), 2004. doi: {10.1029/2003JC001989}. (Cited on pages 39 and 43.)
- R Feistel, DG Wright, K Miyagawa, AH Harvey, J Hrubby, DR Jackett, TJ McDougall, and W Wagner. Mutually consistent thermodynamic potentials for fluid water, ice and seawater: a new standard for oceanography. *Ocean Science*, 4:275–291, 2008. (Cited on page 45.)
- DL Feltham, N Untersteiner, JS Wettlaufer, and MG Worster. Sea ice is a mushy layer. *Geophysical Research Letters*, 33, 2006. doi: 10.1029/2006GL026290. (Cited on page 44.)
- R Fontes. On the development of an independent and accurate measuring instrument based on a fpga for measuring the solid fraction in multiphase systems. Master's thesis, Hamburg University of Applied Sciences, 2009. (Cited on pages 50, 51, 54, and 59.)
- R Fontes, R Fitz, and I Ehlert. Ein Messgerät zur Bestimmung des Festkörperanteils bei der Meereisentstehung. *eForum, Magazin des Departments Informations- und Elektrotechnik*, 2009. (Cited on pages 50, 51, 54, and 59.)
- J Freitag and H Eicken. Meltwater circulation and permeability of Arctic summer sea ice derived from hydrological field experiments. *Journal of Glaciology*, 49(166):349–358, 2003. (Cited on pages 39 and 44.)
- H Goosse, JM Campin, T Fichefet, and E Deleersnijder. Impact of sea-ice formation on the properties of Antarctic bottom water. In Walsh, JE, editor, *Annals of Glaciology*, volume 25, pages 276–281, 1997. (Cited on page 38.)
- C Gordon, C Cooper, CA Senior, H Banks, JM Gregory, TC Johns, JFB Mitchell, and RA Wood. The simulation of SST, sea ice extents and ocean heat transports in a version of the Hadley Centre coupled model without flux adjustments. *Climate Dynamics*, 16(2-3):147–168, 2000. (Cited on page 83.)
- TC Grenfell and GA Maykut. The optical properties of ice and snow in the Arctic Basin. *Journal of Glaciology*, 18:445–463, 1977. (Cited on page 38.)
- P Griewank and D Notz. A 1d model study of gravity drainage in sea ice. *in preparation*, 2012. (Cited on pages 39 and 45.)
- RL Haney. Surface thermal boundary condition for ocean circulation models. *Journal of Physical Oceanography*, 1(4):241–248, 1971. (Cited on pages 80 and 83.)

- AK Huff and JPD Abbatt. Kinetics and product yields in the heterogeneous reactions of HOBr with ice surfaces containing NaBr and NaCl. *Journal of Physical Chemistry A*, 106(21):5279–5287, 2002. (Cited on page 11.)
- EC Hunke, D Notz, A Turner, and M Vancoppenolle. The multiphase physics of sea ice: a review for modellers. *The Cryosphere*, 5, 2011. doi: 10.5194/tc-5-989-2011. (Cited on page 39.)
- RJ Hunter. *Foundations of colloid science*. Oxford University Press, 1st edition, 1987. ISBN 0-19-855187-8. (Cited on pages 52 and 55.)
- M Ingham, D Pringle, and H Eicken. Cross-borehole resistivity tomography of sea ice. *Cold Regions Science and Technology*, 52(3):263–277, 2008. (Cited on pages 50 and 59.)
- D Isleifson, B Hwang, DG Barber, RK Scharien, and L Shafai. C-Band Polarimetric Backscattering Signatures of Newly Formed Sea Ice During Fall Freeze-Up. *IEEE Transactions on Geoscience and Remote Sensing*, 48(8):3256–3267, 2010. (Cited on pages 4 and 10.)
- FP Jardon, F Vivier, M Vancoppenolle, A Lourenço, P Bouruet-Aubertot, and Y Cuypers. Full-depth desalination of warm sea ice. *Journal of Geophysical Research*, in press. (Cited on page 39.)
- OM Johannessen, EV Shalina, and MW Miles. Satellite evidence for an Arctic sea ice cover in transformation. *Science*, 286(5446):7215–7236, 1999. (Cited on pages 3, 38, and 64.)
- AE Jones, PS Anderson, EW Wolff, J Turner, AM Rankin, and SR Colwell. A role for newly forming sea ice in springtime polar tropospheric ozone loss? Observational evidence from Halley station, Antarctica. *Journal of Geophysical Research-Atmospheres*, 111(D8), 2006. doi: {101029/2005JD006566}. (Cited on page 10.)
- K Jones, M Ingham, D Pringle, and H Eicken. Cross-borehole resistivity tomography of Arctic and Antarctic sea ice. *Annals of Glaciology*, 52(57, Part 1):161–168, 2011. (Cited on pages 50 and 59.)
- KA Jones, M Ingham, DJ Pringle, and H Eicken. Temporal variations in sea ice resistivity: Resolving anisotropic microstructure through cross-borehole DC resistivity tomography. *Journal of Geophysical Research*, 115, 2010. doi: {101029/2009JC006049}. (Cited on pages 50 and 59.)
- RE Jordan, EL Andreas, and AP Makshtas. Heat budget of snow-covered sea ice at North Pole 4. *Journal of Geophysical Research*, 104(C4):7785–7806, 1999. (Cited on page 78.)
- T Jung, F Vitart, L Ferranti, and J-J Morcette. Origin and predictability of the extreme negative NAO winter of 2009/10. *Geophysical Research Letters*, 38, 2010. doi: {101029/2011GL046786}. (Cited on pages 4, 11, 64, and 66.)
- L Kaleschke, A Richter, J Burrows, O Afe, G Heygster, J Notholt, AM Rankin, HK Roscoe, J Hollwedel, T Wagner, and H-W Jacobi. Frost flowers on sea ice as a source of sea salt and their influence on tropospheric halogen chemistry. *Geophysical Research Letters*, 31(16):4 pp, 2004. doi: {101029/2004GL020655}. (Cited on page 10.)

- A Kovacs. *Sea ice part I. Bulk salinity vs. ice floe thickness*. US Army Cold Regions Research and Engineering Laboratory, Hanover, NH, 1996. (Cited on pages 4 and 38.)
- R Kwok, GF Cunningham, M Wensnahan, I Rigor, HJ Zwally, and D Yi. Thinning and volume loss of the Arctic Ocean sea ice cover: 2003-2008. *Journal of Geophysical Research*, 114, 2009. doi: {10.1029/2009JC005312}. (Cited on pages 3 and 38.)
- B Light, GA Maykut, and TC Grenfell. Effects of temperature on the microstructure of first-year Arctic sea ice. *Journal of Geophysical Research*, 108 (C2), 2003. doi: {10.1029/2001JC000887}. (Cited on pages 43 and 46.)
- J Lyklema. *Fundamentals of interface and colloid science*. Academic Press, 1st edition, 1991. ISBN 978-0124605251. (Cited on page 55.)
- S Martin, R Drucker, and M Fort. A laboratory study of frost flower growth on the surface of young sea-ice. *Journal of Geophysical Research-Oceans*, 100 (C4):7027-7036, 1995. (Cited on pages 4, 16, and 25.)
- S Martin, YL Yu, and R Drucker. The temperature dependence of frost flower growth on laboratory sea ice and the effect of the flowers on infrared observations of the surface. *Journal of Geophysical Research-Oceans*, 101(C5): 12111-12125, 1996. (Cited on pages 4, 10, 16, 20, 22, and 32.)
- DG Martinson and M Steele. Future of the Arctic sea ice cover: Implications of an Antarctic analog. *Geophysical Research Letters*, 28(2), 2001. doi: {10.1029/2000GL011549}. (Cited on pages 3 and 71.)
- J Maslanik, S Drobot, C Fowler, W Emery, and R Barry. On the Arctic climate paradox and the continuing role of atmospheric circulation in affecting sea ice conditions. *Geophysical Research Letters*, 34(3), 2007. doi: {10.1029/2006GL028269}. (Cited on pages 3 and 38.)
- J Maslanik, J Stroeve, C Fowler, and W Emery. Distribution and trends in Arctic sea ice age through spring 2011. *Geophysical Research Letters*, 38, 2011. doi: {10.1029/2011GL047735}. (Cited on pages 3, 38, and 64.)
- GA Maykut. Heat and mass balance of Arctic ice pack. *Naval Research Reviews*, 31(7):17-35, 1978. (Cited on page 64.)
- GA Maykut and N Untersteiner. Some results from a time-dependent model of sea ice. *Journal of Geophysical Research*, 76(6):1550-&, 1971. (Cited on page 64.)
- M McPhee. *Air-Ice-Ocean Interaction: Turbulent Ocean Boundary Layer Exchange Processes*. Springer Verlag, 2008. (Cited on pages 64 and 72.)
- MG McPhee, JH Morison, and F Nilsen. Revisiting heat and salt exchange at the ice-ocean interface: Ocean flux and modeling considerations. *Journal of Geophysical Research*, 113, 2008. doi: {10.1029/2007JC004383}. (Cited on pages 64, 72, and 85.)
- MG McPhee, TP Stanton, JH Morison, and DG Martinson. Freshening of the upper ocean in the Arctic: Is perennial sea ice disappearing? *Geophysical Research Letters*, 25(10):1729-1732, 1998. (Cited on page 64.)
- RM Morey, A Kovacs, and GFN Cox. Electromagnetic properties of sea ice. *Cold Regions Science and Technology*, 9(1):53 - 75, 1984. (Cited on page 38.)

- F Nansen. *Nebelheim Entdeckung und Erforschung der nördlichen Länder und Meere*. Leipzig, FA Brockhaus, 1911. (Cited on page 101.)
- SV Nghiem, IG Rigor, DK Perovich, P Clemente-Colon, JW Weatherly, and G Neumann. Rapid reduction of Arctic perennial sea ice. *Geophysical Research Letters*, 34(19), 2007. doi: {10.1029/2007GL031138}. (Cited on pages 3 and 38.)
- D Notz. *Thermodynamic and Fluid-Dynamical Processes in Sea Ice*. PhD thesis, Trinity College, Cambridge, UK, 2005. (Cited on pages 5, 50, 51, 54, 57, 58, and 59.)
- D Notz and MG Worster. Desalination processes of sea ice revisited. *Journal of Geophysical Research*, 114(C05006), 2009. doi: {10.1029/2008JC004885}. (Cited on page 39.)
- D Notz, JS Wettlaufer, and MG Worster. A non-destructive method for measuring the salinity and solid fraction of growing sea ice in situ. *Journal of Glaciology*, 51(172):159–166, 2005. (Cited on pages 50, 51, 54, 55, and 59.)
- RW Obbard, HK Roscoe, EW Wolff, and HM Atkinson. Frost flower surface area and chemistry as a function of salinity and temperature. *Journal of Geophysical Research*, 114, 2009. doi: {101029/2009JD012481}. (Cited on page 11.)
- N Ono. Thermal properties of sea ice IV. *Cold Regions Research and Engineering Lab, Hanover NH, Draft Translation 467*, 1975. (Cited on page 38.)
- RG Onstott. *SAR and scatterometer signatures of sea ice, in*, volume 68. Geophys Monogr Ser, Washington, DC, 1992. (Cited on pages 4 and 10.)
- DK Perovich and B Elder. Estimates of ocean heat flux at SHEBA. *Geophysical Research Letters*, 29(9), 2002. doi: {101029/2001GL014171}. (Cited on page 3.)
- DK Perovich and JA Richter-Menge. Surface characteristics of lead ice. *Journal of Geophysical Research-Oceans*, 99(C8):16341–16350, 1994. (Cited on pages 10, 16, 20, and 28.)
- DK Perovich and JA Richter-Menge. Loss of Sea Ice in the Arctic. *Annual Review of Marine Science*, 1:417–441, 2009. (Cited on page 3.)
- DK Perovich, CS Roesler, and WS Pegau. Variability in arctic sea ice optical properties. *Journal of Geophysical Research*, 103(C1):1193–1208, 1998. (Cited on pages 3, 50, and 64.)
- DK Perovich, EL Andreas, CW Fairall, PS Guest, POG Persson, and 18 others. Year on ice gives climate insights. *EOS, Transactions of the American Geophysical Union*, 80(41):481–486, 1999. (Cited on page 4.)
- POG Persson, CW Fairall, EL Andreas, PS Guest, and DK Perovich. Measurements near the atmospheric surface flux group tower at SHEBA: near-surface conditions and surface energy budget. *Journal of Geophysical Research*, pages SHE21–1–35. (Cited on page 64.)
- AM Rankin, EW Wolff, and S Martin. Frost flowers: Implications for tropospheric chemistry and ice core interpretation. *Journal of Geophysical Research*, 107(D23):AAC4–1–15, 2002. (Cited on pages 10 and 11.)

- PH Rieger. Kluwer Academic Pub, 2nd edition, 1993. ISBN 0-412-04391-2. (Cited on page 52.)
- IG Rigor and JM Wallace. Variations in the age of Arctic sea-ice and summer sea-ice extent. *Geophysical Research Letters*, 31(9), 2004. doi: {10.1029/2004GL019492}. (Cited on pages 3 and 38.)
- HK Roscoe, B Brooks, AV Jackson, MH Smith, SJ Walker, RW Obbard, and EW Wolff. Frost flowers in the laboratory: Growth, characteristics, aerosol, and the underlying sea ice. *Journal of Geophysical Research*, 116, 2011. doi: {101029/2010JD015144}. (Cited on pages 11 and 25.)
- DA Rothrock, Y Yu, and GA Maykut. Thinning of the Arctic sea-ice cover. *Geophysical Research Letters*, 26(23):3469–3472, 1999. (Cited on page 64.)
- P Schwerdtfeger. The thermal properties of sea ice. *Journal of Glaciology*, 4: 789–807, 1963. (Cited on page 38.)
- JA Screen and I Simmonds. The central role of diminishing sea ice in recent Arctic temperature amplification. *Nature*, 464(7293), 2010. doi: {10.1038/nature09051}. (Cited on page 3.)
- AJ Semtner. Model for thermodynamic growth of sea ice in numerical investigations of climate. *Journal of Physical Oceanography*, 6(3):379–389, 1976. (Cited on page 31.)
- TGL Shirtcliffe and RC Kerr. On the use of electrical resistance and temperature as measures of the solid fraction in a mushy layer. *Journal of Crystal Growth*, 125(3-4):495–501, 1992. (Cited on pages 5, 51, and 59.)
- TGL Shirtcliffe, HE Huppert, and MG Worster. Measurements of the solid fraction in the crystallization of a binary melt. *Journal of Crystal Growth*, 113(3-4):566–574, 1991. (Cited on pages 5, 50, 51, 53, and 59.)
- A Stössel, K Yang, and S-J Kim. On the Role of Sea Ice and Convection in a Global Ocean Model. *Journal of Physical Oceanography*, 32:1194–1208, 2002. (Cited on page 38.)
- J Stroeve, MM Holland, W Meier, T Scambos, and M Serreze. Arctic sea ice decline: Faster than forecast. *Geophysical Research Letters*, 34(9), 2007. doi: {10.1029/2007GL029703}. (Cited on page 3.)
- RW Style. *The formation and evolution of frost flowers and related phenomena*. PhD thesis, Trinity College, Cambridge, UK, 2007. (Cited on pages 4, 16, 17, and 20.)
- RW Style and MG Worster. Frost flower formation on sea ice and lake ice. *Geophysical Research Letters*, 36(11):L11501 (4 pp), 2009. (Cited on pages 4, 10, and 16.)
- WB Tucker, JW Weatherly, DT Eppler, LD Farmer, and DL Bentley. Evidence for rapid thinning of sea ice in the western Arctic Ocean at the end of the 1980s. *Geophysical Research Letters*, 28(14):2851–2854, 2001. (Cited on page 64.)
- N Untersteiner. Natural desalination and equilibrium salinity profile of perennial sea ice. *Journal of Geophysical Research*, 73(4):1251–&, 1968. (Cited on page 39.)

- M Vancoppenolle, H Goosse, A de Montety, T Fichet, B Tremblay, and JL Tison. Modeling brine and nutrient dynamics in antarctic sea ice: The case of dissolved silica. *Journal of Geophysical Research*, 115(C2), 2010. doi: 10.1029/2009JC005369. (Cited on page 45.)
- J Wang, J Zhang, E Watanabe, M Ikeda, K Mizobata, JE Walsh, X Bai, and B Wu. Is the Dipole Anomaly a major driver to record lows in Arctic summer sea ice extent? *Geophysical Research Letters*, 36, 2009. doi: {10.1029/2008GL036706}. (Cited on page 64.)
- YT Wang, Bian LG, Ma YF, Tang J, Zhang DQ, and Zheng XD. Surface ozone monitoring and background characteristics at Zhongshan Station over Antarctica. *Chinese Science Bulletin*, 56(10):1011–1019, 2011. (Cited on page 10.)
- RC Weast. *Handbook of Chemistry and Physics*. The Chemical Rubber Co, Cleveland Ohio, 52nd edition, 1971. (Cited on page 53.)
- WF Weeks. *Growth conditions and the structure and properties of sea ice*. University of Helsinki Press, 1998. (Cited on page 45.)
- WF Weeks. *On sea ice*. University of Alaska Press, Fairbanks, Alaska, 2010. (Cited on pages 3, 4, 38, 39, 50, and 75.)
- WF Weeks and A Assur. The mechanical properties of sea ice. *Cold Regions Research and Engineering Lab, Hanover NH, Monogr II-C3*, 1967. (Cited on page 38.)
- JS Wettlaufer. Heat-flux at the ice-ocean interface. *Journal of Geophysical Research*, 96(C4), 1991. (Cited on page 64.)
- JS Wettlaufer. The phase evolution of young sea ice. *Geophysical Research Letters*, 24:1251–1254, 1997. (Cited on pages 39, 44, and 45.)
- JS Wettlaufer, MG Worster, and HE Huppert. Solidification of leads: Theory, experiment, and field observations. *Journal of Geophysical Research*, 105(C1): 1123–1134, 2000. (Cited on page 45.)
- Karl Weyprecht. *Die Metamorphosen des Polareises*. Verlag von Moritz Perles, Wien, 1879.
- JP Wilkinson, G DeCariolis, I Ehlert, D Notz, KU Evers, P Jochmann, S Gerland, M Nicolaus, N Hughes, S Kern, S de la Rosa, L Smedsrud, S Sakai, and P Shen, H Wadhams. Ice tank experiments highlight changes in sea-ice types. *EOS, Transactions of the American Geophysical Union*, 90(10):81–82, 2009. (Cited on page 51.)
- MG Worster. Instabilities of the liquid and mushy regions during solidification of alloys. *Journal of Fluid Mechanics*, 237:649–669, 1992. (Cited on pages 44 and 45.)
- MG Worster. *Perspectives in Fluid Dynamics: A Collective Introduction to Current Research*. Cambridge University Press, Cambridge, UK, 2000. (Cited on page 39.)
- D Yamagishi and P Langhorne. Experimental study of phase change in rapidly growing sea ice. In *IAHR International Symposium on Ice*. (Cited on pages 5 and 51.)

- JY Yang and JD Neelin. Sea-ice interaction with the thermohaline circulation. *Geophysical Research Letters*, 20(3):217–220, 1993. (Cited on page 83.)
- JY Yang and JD Neelin. Sea-ice interaction and the stability of the thermohaline circulation. *Atmosphere-Ocean*, 35(4):433–469, 1997. (Cited on page 83.)
- JL Zhang. Warming of the Arctic ice-ocean system is faster than the global average since the 1960s. *Geophysical Research Letters*, 32(19), 2005. doi: {10.1029/2005GL024216}. (Cited on page 3.)
- S Zhang, CA Lin, and RJ Greatbatch. A decadal oscillation due to the coupling between an ocean circulation model and a thermodynamic sea-ice model. *Journal of Marine Research*, 53(1):79–106, 1995. (Cited on pages 83 and 84.)
- J Zukriegel. *Cryologia maris*. Charles IV University, Praha, 1935.

Polar foxes have a black skin. Don't ask how we found out. And they really like eating cables connecting the most important of your instruments with the data logger. I am curious if polar rabbits have a black skin too. We need to answer this during our next field trip ...

And whenever you are taking an ice core—not, as you should do it, with the power of your arms—with a drilling machine ... just take care about a safe connection to the ice-core barrel. It might be that this 6000 dollar thing will get lost into the depths of the polar ocean.

... and as long as man will listen to the roar of the waves above the depth of the sea, as long as the human eye will follow the play of the northern light on the silent snowy landscapes, and as long as it will look out for the celestial bodies far away in infinite space, so long the romance of the Unknown will lead the human genius forward and upward!

— Fridtjof Nansen, 1911

